

NAG 5-528

GODDARD
GRANT

IN-13-CR

115292

AN ORBIT SIMULATION STUDY OF A GEOPOTENTIAL RESEARCH MISSION INCLUDING SATELLITE-TO-SATELLITE TRACKING AND DISTURBANCE COMPENSATION SYSTEMS 119 P.

by

Peter G. Antreasian

(NASA-CR-182353) AN ORBIT SIMULATION STUDY
OF A GEOPOTENTIAL RESEARCH MISSION INCLUDING
SATELLITE-TO-SATELLITE TRACKING AND
DISTURBANCE COMPENSATION SYSTEMS (Texas
Univ.) 119 p

N88-14997

Unclas
0115292

CSCL 22A G3/13

Center for Space Research

The University of Texas at Austin

January 1988

CSR-88-1

This report was prepared under

Grant No. NAG5-528

for the

National Aeronautics and Space Administration

Goddard Space Flight Center

Greenbelt, Maryland 20771

by the

Center for Space Research

The University of Texas at Austin

Austin, Texas 78712

under the direction of

Dr. Bob E. Schutz

Dr. Byron D. Tapley

Table of Contents

CHAPTER 1	Introduction.....	1
1.1	Description of the Low-Low Scenario for the Geopotential Research Mission.....	3
1.2	The DISCOS System	5
1.3	The Satellite-to-Satellite Tracking System.....	6
1.4	Requirements of GRM.....	6
1.5	Organization	7
CHAPTER 2	The Simulation of GRM	11
2.1	Equations of Motion	13
2.1.1	Pines Formulation of the Geopotential	14
2.1.2	The Encke Formulation	15
2.2	Initial Conditions.....	17
2.3	Encke Reference Orbits	18
2.4	The Gravity Model.....	19
2.5	The One-Way Doppler Range-Rate Algorithm.....	20
2.6	KSGFS Numerical Integrator	22
2.7	Computational Facilities	23
CHAPTER 3	Simulations of the True and Nominal Orbits	25
3.1	Pre-evaluation Computer Cost Analysis	25
3.2	True Orbit Simulation	27
3.3	Nominal Orbit Simulation.....	29

	3.4	RTN Differences between Nominal and True orbits.....	32
	3.5	Range-Rate Measurements.....	33
CHAPTER	4	Simulation of the Drag Compensation Mechanism	45
	4.1	The Disturbance Compensation System.....	46
	4.2	The Design of the Drag-free Thruster Control Algorithm.....	49
	4.3	Equations of Relative Motion.....	52
	4.4	The Force Model.....	54
	4.4.1	Geopotential Model	54
	4.4.2	Drag Model	54
	4.4.3	Thrust Model	57
	4.5	Numerical Integration Algorithm.....	58
	4.6	The Logic of the Thruster Control Algorithm	58
	4.7	The Ball-Centering Attitude Control Law.....	65
	4.8	Results	67
	4.8.1	Effectiveness of the Thruster Control Algorithm.....	67
	4.8.2	Effectiveness of the Ball-Centering Attitude Control Law.....	68
	4.8.3	Imparted Velocity Thruster Turn-off Adjustments	69
	4.8.4	Fuel Expenditure	70
CHAPTER	5	Conclusions.....	109
	5.1	Summary.....	110
	5.2	Future Study	111
		Bibliography.....	113

CHAPTER I

INTRODUCTION

"Because the measurement of the global gravity is a primary objective for both solid-earth dynamics and ocean dynamics and is an important secondary objective for continental geology, the determination of an improved gravitational field through space measurement should be an objective of highest priority for the 1980's,"

—The Space Science Board, *A Strategy for Earth Science from Space in the 1980's*, the National Academy of Sciences, Washington, D.C., [1982].

In the early 1980's, NASA proposed a Geopotential Research Mission (GRM) to globally determine high precision gravitational and magnetic fields of Earth with advanced science techniques using full Earth coverage, polar orbiting satellites. These detailed fields are required for the improvement of Earth's mathematical models that help scientists to understand the geodynamical activities which are continually evolving the Earth's internal and external structure and the dynamics of the oceans that influence ocean circulation and global climates. In addition, the measurement of the geopotential to high degree and order will improve orbit determination of other geodetic satellites.

Currently, three scenarios exist for recovering the higher degree and order coefficients of Earth's gravity potential. The first scenario, described as the "low-low" configuration, consists of two coplanar, low altitude, polar orbiting, satellites (Figure 1.1) that measure the Earth's gravity anomalies through range-rates derived from the Satellite-to-Satellite Tracking system, SST (discussed in Section 1.3)

[Keating *et al*, 1986]. The second scenario consists of a single low altitude, polar orbiting satellite equipped with a high precision gravity gradiometer sensor onboard. The third scenario, described as the "high-low" configuration, consists of a high altitude satellite along with a low altitude, polar orbiting, satellite. This high-low configuration was also designed to use a Satellite-to-Satellite Tracking system (SST) for measuring Earth gravity anomalies [Holmes *et al*, 1987].

Each low altitude satellite in any case is "drag-free", which means that orbital effects due to nonconservative forces such as drag and solar radiation pressure are offset by means of a Disturbance Compensation System (DISCOS) that appropriately fires thrusters to offset the effects due to these disturbances. The DISCOS is discussed in more detail in Section 1.4 and Chapter 4.

The orbital requirements of the low-low gravity mission also satisfy the orbital requirements for the magnetic mission. Therefore, the lead low-low satellite will measure the Earth's magnetic fields with the use of onboard scalar and vector magnetometers.

To properly plan for this mission, a high precision (true) orbit simulation of the low-low GRM satellite mission was performed at the University of Texas at Austin using the Cray X-MP/24 supercomputer. With this orbit simulation and a nominal orbit simulation that was fitted to the true orbits in a least squares sense, the geodetic science community will be able to test gravity evaluation techniques that are essential to recovering a geopotential of high degree and order. In addition, a simulation of the DISCOS system was also performed to assist in the planning for the mission. Therefore, the purpose of this report is: 1) to present a simulation study of a proposed GRM mission by numerically integrating a high precision orbit for each low-low satellite using a geopotential with coefficients up to degree and order 360 and calculating the SST's one-way Doppler range-rate measurements, 2)

to present a nominal orbit simulation of the aforementioned case with differences between the true and nominal ephemerides kept within specified limits, and 3) to develop a thruster control algorithm which simulates the DISCOS system so that fuel expenditure and thruster-on times can be studied. Since each of the aforementioned scenarios contain a low altitude segment, the techniques used to analyze the low-low scenario will be applicable to all three scenarios.

1.1 Description of the Low-Low Scenario for the Geopotential Research Mission

As proposed by *Keating et al*, [1986], the GRM mission that was once referred to as GRAVSAT/MAGSAT, is configured using two 160 km altitude, polar orbiting, drag-free satellites in coincident, near circular orbits with the longitude of the ascending node equal to 90° , and the mean argument of periapse equal to 90° . In spite of perturbations due to the oblateness, the nature of the orbits is such that the mean argument of periapse is constant, a "frozen orbit" [*White*, 1987]. The minimum mission lifetime goal was set at 6 months to achieve high resolution (1° by 1°) groundtrack coverage of Earth which will result in an equatorial spacing of approximately 111 km. The SST onboard will use an integrated one-way Doppler system to calculate the line of sight range-rates between the satellites which will have separation distances of 100 km to 600 km. A Disturbance Compensation System (DISCOS) will keep the satellites essentially "drag-free" by controlling radial, along-track and cross-track thrusters to negate the effects due to drag and solar radiation pressure, so that high sensitivity to the Earth's gravity field will be achieved [*Keating et al*, 1986].

It is desired that the groundtrack of each satellite repeats after a certain number of days that are not commensurate with the orbital period. The number of days required for the groundtrack repeat determines the resolution of global coverage.

While in a frozen orbit the mean orbital ellipse will not change its eccentricity or orientation in space. This means that each satellite will fly over the same location on Earth at nearly the same altitude, and their respective perigee location will remain fixed over the north pole.

The GRM launch date is currently proposed for sometime in the period 1993-95. After launching one of NASA's Space Shuttles into polar orbit from the Western Space and Missile Center, the Remote Manipulator Unit (RMU) will deploy the two satellites from the Space Shuttle's cargo bay. At a nominal altitude of 275 km, both satellites will be deployed in the same orbital plane but separated by 50 km. Then after several Hohman transfers and daily checkouts, the satellites are lowered to the 160 km altitude with a separation of 150 km to begin mission operations 168 hours after deployment.

The orbits of the spacecraft will be determined by tracking observations provided by the Defense Mapping Agency (DMA) with NASA's Tracking Data Relay Satellite System (TDRSS), the Global Positioning System, the TRANET ground based tracking network, or a subset of these techniques.

At the start of the mission with 1400 kg of hydrazine fuel aboard to power the DISCOS and attitude control thrusters, the leading satellite would have a mass of 2734 kg while the trailing satellite has a mass of 2517 kg. This mass difference is due to a boom that carries the magnetometers, and star cameras which maintain the spacecraft's orientation in space that are included on the lead spacecraft. Each satellite has a frontal area of 1.06 m² and an expected drag coefficient of 3.5. The

external and internal configurations of the lead GRM satellite are shown respectively in Figures 1.2 and 1.3.

1.2 The DISCOS System

The atmosphere at 160 km is dense enough to cause rapid orbit decay. If drag effects are not counteracted, each satellite's lifetime would be less than 3 days [Holmes *et al*, 1987]. Since the density of Earth's atmosphere is directly related to the current solar activities such as the amount of solar flux received by the Earth, it can not be easily predicted. Furthermore, since drag and solar radiation pressure would corrupt the science data, a DISCOS system will be used aboard the low altitude spacecraft to ensure that these disturbances are kept to a minimum. This can be achieved by firing thrusters to contain an inner satellite "proof mass" within a cavity at the satellite's centroid.

Eventually, the outer portion of the satellite drops in altitude because of drag and moves ahead of the proof mass, thus causing the proof mass to move aft with respect to the center of mass of the outer satellite. Upon the proof mass's approach to a deadband threshold, the corresponding thrusters fire on the outer satellite until the proof mass has a predetermined velocity with respect to the satellite's mass center. Relative to the outer satellite, the proof mass then moves forward until drag causes the relative velocity of the proof mass to become zero and then reverses direction. The proof mass then approaches the deadband threshold again and a control limit cycle is maintained. This steady-state condition involves relatively short firing pulses and relatively long non-thrusting coast arcs. The details of this DISCOS system are presented later in Chapter 4.

1.3 The-Satellite-to-Satellite Tracking System

Line-of-sight relative range-rates between the two satellite are provided by the Satellite-to-Satellite Tracking System. With this system, each satellite's transmitter continuously transmits millimeter radio signals at 42 GHz and 91GHz to each other. These frequencies were chosen to keep errors due to ionospheric effects below the limit necessary to satisfy the accuracy requirements [Keating *et al*, 1986].

As the pair of sateelites approach and pass a gravity anomaly, variations in the motion of the satellites are first induced on the lead satellite and then on the trailing satellite. As a result, the relative velocity between the satellites varies, from - 1.0 m/s to + 1.0 m/s. The variation in velocity, referred to as the relative range-rate, is an indirect measure of the gravity anomalies. The range variations are measured by the Doppler-shift of the frequency of the received signal when compared to a reference signal provided by a 5 MHz oscillator [Keating *et al*, 1986].

1.4 Requirements of GRM

The Satellite-to-Satellite Tracking system is required to measure the relative velocities between the antennae on each spacecraft to better than 1 $\mu\text{m} / \text{sec}$. This requirement is essential for the recovery of the gravity field, so that at an altitude of 160 km the data set would provide resolutions of at least 1-2 mgal (1 mgal = 10^{-5} m/s^2) in gravity anomalies, and 5-10 cm in geoid height with a spatial resolution of 100 km. These resolutions are recommended by national scientific communities for the study of geological features such as sedimentary basins, batholiths, mountain

ranges, subduction zones and shields [Keating *et al.*, 1986]. Also, the magnetic field will be resolved to 1 nT (nanotesla) at a 100 km spatial resolution [Keating *et al.*, 1986]. The orbit determination accuracy (3σ) requirements for the gravity mission are 100 meters in the radial direction and 300 meters in the along- and cross-track directions, whereas the magnetic mission requires an accuracy of 60 m in the radial direction, and 100 m in the along- and cross-track directions [Keating, *et al.*, 1986].

1.5 Organization

The research presented in this work covers details of the high precision and nominal orbit simulations which are discussed in Chapter 2. Chapter 2 also describes the mathematical formulae, software and hardware used for the generation of each simulation. The results of this study are shown in Chapter 3. The DISCOS instrument is discussed along with its history and implementation with GRM in Chapter 4. Also explained in Chapter 4 is the Drag-free Thruster Control Algorithm that contains all the control logic to operate DISCOS along with all the mathematical formulae, force models, software, and hardware that are used to simulate it. The results of this study are also presented in Chapter 4. The conclusions of this report are discussed in Chapter 5.

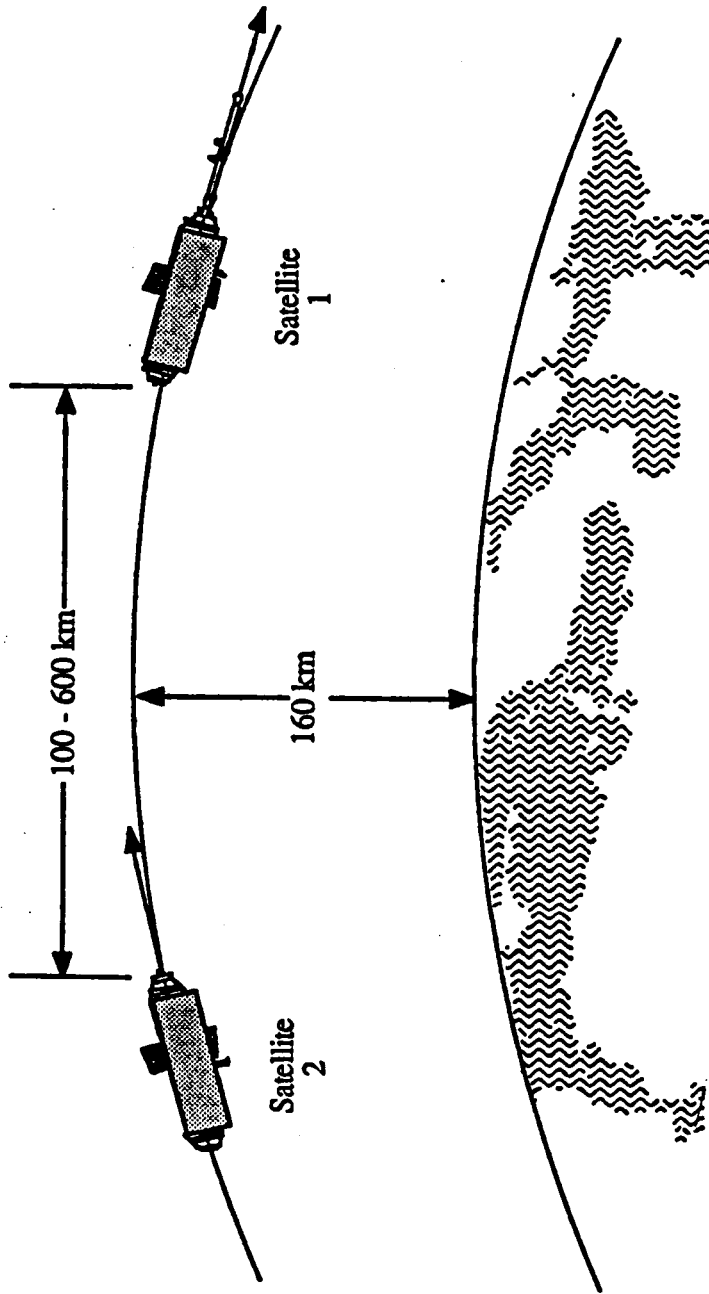


Figure 1.1 The "Low-Low" Flight Scenario of GRM

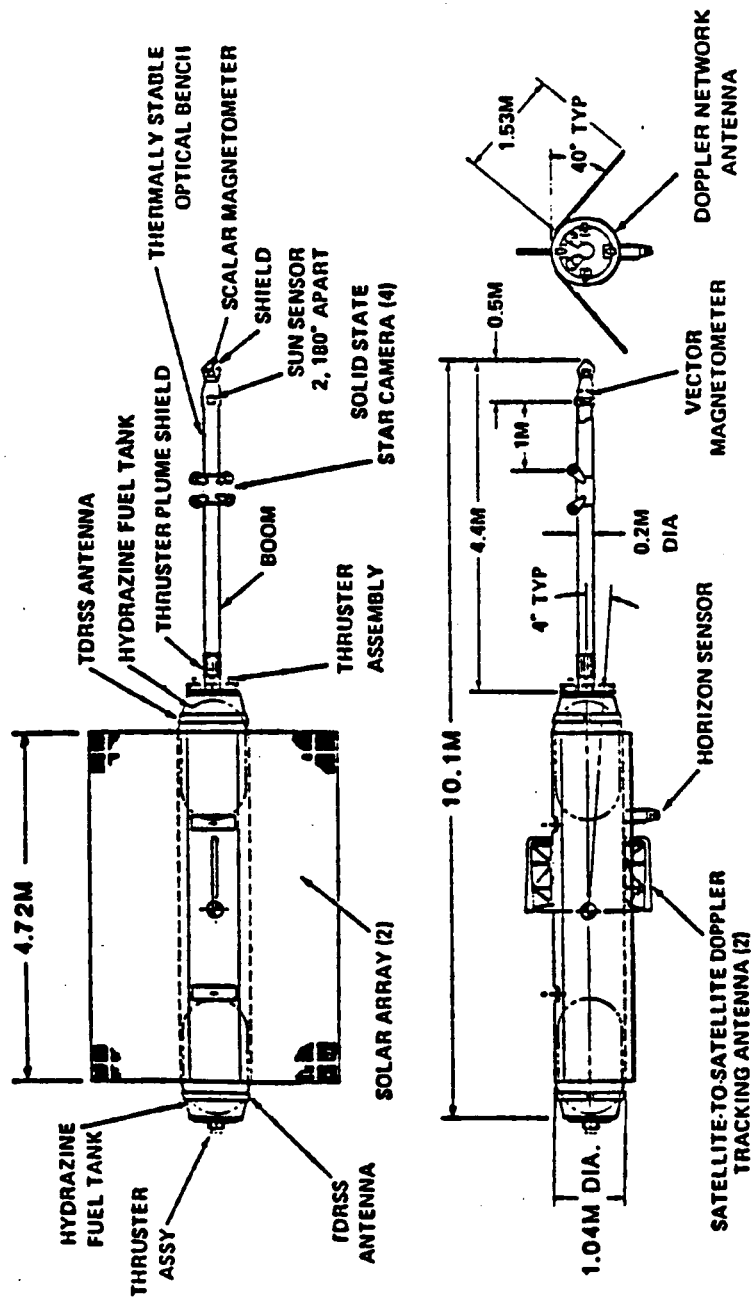


Figure 1.2 The External Configuration of the Lead GRM Satellite (Satellite 1)

[Keating et al, 1986].

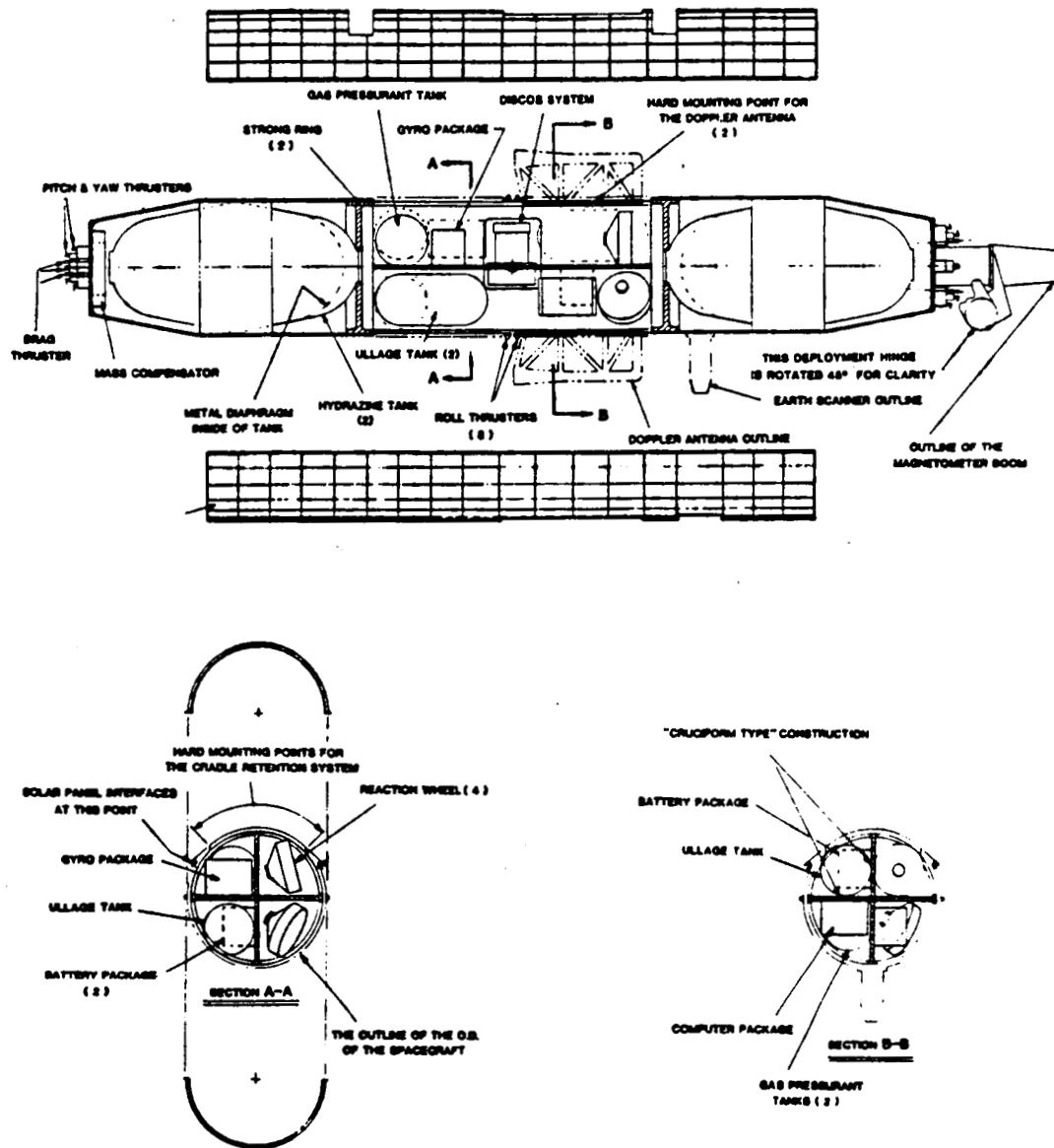


Figure 1.3 The Internal Configuration of the Lead GRM Satellite
[Keating et al, 1986].

CHAPTER II

SIMULATION OF GRM

Two orbit simulations were performed for GRM. The first simulation consisted of a high precision representation of the *actual* orbits of the proof masses inside the cavities of the two low altitude satellites described in Chapter 1. The second simulation consisted of nominal orbits of the two 'inner' satellites determined by least squares approximation of the actual orbits.

The high precision 'true' orbit was generated using an Ohio State University gravity field complete to degree and order 360 [Rapp, 1986], referred to as the "OSU86F" field. The ephemerides of the two low altitude satellites were generated at 4 second intervals for 32 solar days. Satellite-to-satellite line-of-sight range-rates measured by each spacecraft's integrated one-way Doppler antenna are also included in this simulation. The initial conditions of each satellite orbit were especially designed so that their groundtracks repeat after 32 sidereal days [White, 1987]. This 32 sidereal day repeating groundtrack results in exactly 525 orbital revolutions for each satellite. Therefore, the orbital period is not commensurate with the repeat period so that high resolution coverage of Earth's gravity field can be achieved (1° by 1°). To concentrate on the effects due to high degree and order terms in Earth's gravitational field, the gravitational effects due to the Sun or Moon were not included in the force model nor were effects due to kinematic or temporal forces. To keep computer costs low and maintain extreme accuracy, the KSG [Lundberg, 1984] fixed-mesh multi-step integrator was used along with the Encke

formulation of the differential equations. Furthermore, to avoid singularities at the Earth's poles, *Pines'* [1973] formulae that uses direction cosines rather than spherical coordinates were used to evaluate the geopotential.

The nominal orbit includes the ephemerides of the two proof masses estimated by performing a least squares fit to the true ephemerides plus the estimated range-rates between the two 'inner' satellites. The nominal orbit was generated using a modified Goddard Earth Model 10B (GEM10B) gravity field that includes coefficients to degree and order 36 with the zonals J_2 and J_3 and the first two pairs of resonant coefficients at orders 16, 17, 33, 49, and 82 adjusted [White, 1987]. The initial conditions of the nominal orbits were especially designed for this simulation to maintain low radial, transverse and normal (RTN) differences between the true and nominal orbits (residuals), but its 32 sidereal day mission was not required to repeat [White, 1987]. The University of Texas Orbit Processor, UTOPIA, along with the Encke formulation of the differential equations and *Pines* [1973] formulation of the geopotential were used to generate the nominal orbit simulation.

This chapter contains the mathematical formulae that model the motion of each GRM satellite in orbit about a non-spherical Earth. Section 2.1 presents the equations of motion that describe the orbit of each satellite and the force model that perturbs the satellites' motion. *Pines* [1973] formulation of the Geopotential is explained in Section 2.1.1. Increased numerical accuracy is obtained through the use of the Encke integration method which is presented in Section 2.1.2. The initial conditions for both the true and nominal simulations are discussed in Section 2.2. Section 2.3 lists the parameters that describe the Encke reference orbits. The gravity models are discussed in Section 2.4. The Integrated One-Way Doppler Range-Rate

computer algorithm that simulates the Satellite-To-Satellite Tracking system is presented in Section 2.5. The equations of motion are integrated efficiently, saving computer costs with the use of the KSGFS numerical integration algorithm described in Section 2.6. Finally, the specifications of the Cray X-MP/24 supercomputer used to numerically integrate the satellites' orbits is described in Section 2.7.

2.1 The Equations of Motion

The orbit of each satellite is modeled by Newton's Law of Gravitation which states that the force due to mass attraction between two point masses M and m separated by a distance r is given by the product of the masses, divided by the square of the distance and multiplied by a gravitational constant, G , or

$$F = \frac{GMm}{r^2} \quad (2.1)$$

By cancelling the satellite's mass (m) from both sides of Equation (2.1) and adding a perturbative force, the equations governing the motion of each satellite are

$$\ddot{\bar{r}} = -\frac{\mu\bar{r}}{r^3} + \bar{f} \quad (2.2)$$

where

\bar{r} = the position vector of the satellite as referenced to a nonrotating, geocentric coordinate system, such as defined by a mean epoch of 2000,

μ = the gravitational parameter of Earth,

\bar{f} = the perturbing force due to nonsphericity of Earth.

The proof mass will be susceptible to only conservative gravitational forces. Only the gravitational forces due to the Earth's static potential were examined. The forces due to third-body effects from the sun or moon, temporal effects from land and ocean tides, kinematic effects from precession, nutation, polar motion and UT1 variations were not included in this model because they would complicate the gravity evaluation techniques. Nonconservative forces such as drag and solar radiation pressure, likewise, will not effect the proof mass because of the DISCOS system. The gravitational force is derived from the gradient of the Earth's potential, that is,

$$\bar{\mathbf{f}} = -\nabla U \quad (2.3)$$

where the geopotential, U , is expressed in terms of spherical harmonics as:

$$U = \frac{\mu}{r} + \frac{\mu}{r} \sum_{n=1}^{\infty} \left(\frac{a_e}{r}\right)^n P_n(\sin \phi) C_{n,0} + \frac{\mu}{r} \sum_{n=1}^{\infty} \sum_{m=1}^n \left(\frac{a_e}{r}\right)^n P_{nm}(\sin \phi) [C_{n,m} \cos m\lambda + S_{n,m} \sin m\lambda] \quad (2.4)$$

where r , ϕ , λ are the radius, latitude, and longitude of the satellite's proof mass, modelled as a point mass with respect to the center of Earth, a_e and μ are the mean equatorial radius and the gravitational parameter of the Earth, respectively, P_{nm} are the associated Legendre functions, C_{nm} and S_{nm} are the constant geopotential coefficients, and n and m are the degree and order of the geopotential field.

2.1.1 Pines Formulation of the Geopotential

Since the GRM mission specifies a polar orbit for global coverage of Earth, a

singularity problem exists at the poles when the gradient of the spherical harmonic geopotential representation in Equation 3.4 is calculated. By using direction cosines rather than spherical coordinates, *Pines* [1973] reformulated Equation 2.4 so that the singularities no longer exist. The geopotential can now be used for polar orbits with the form being

$$U = \frac{\mu}{r} + \frac{\mu}{r} \sum_{n=1}^{\infty} \left(\frac{a_e}{r}\right)^n A_n(u) C_{n,0} + \frac{\mu}{r} \sum_{n=1}^{\infty} \sum_{m=1}^n \left(\frac{a_e}{r}\right)^n A_{nm}(u) [C_{n,m} r_m(s,t) + S_{n,m} i_m(s,t)] \quad (2.5)$$

where s , t , and u are the direction cosines,

$$s = \frac{x}{r}, \quad t = \frac{y}{r}, \quad u = \frac{z}{r}$$

$A_{n,m}$ are the "derived" Legendre functions, and $r_m(s,t)$ and $i_m(s,t)$ are the real and imaginary parts of $(s + j t)^m$. Recursion algorithms used for the calculation of the "derived" Legendre functions in *Pines'* formulation on high speed computers is discussed by *Lundberg and Schutz* [1987].

2.1.2 The Encke Formulation

A technique to preserve numerical accuracy during integration is provided by the Encke integration method. This technique uses an analytic reference orbit which closely matches the true orbit. The Encke vector then is described as the difference between the satellite's true trajectory and the reference orbit. By numerically integrating the Encke vector rather than the satellite's true state several significant digits can be preserved [*Lundberg, 1985*].

The Encke vector denoted by $\bar{\epsilon}$ is equal to the difference between the reference orbit, \bar{r}_s and the true orbit position, \bar{r} as shown in Figure (2.1). The Encke vector with its first and second time derivatives are then

$$\bar{\epsilon} = \bar{r} - \bar{r}_s \quad (2.6)$$

$$\dot{\bar{\epsilon}} = \dot{\bar{r}} - \dot{\bar{r}}_s \quad (2.7)$$

$$\ddot{\bar{\epsilon}} = \ddot{\bar{r}} - \ddot{\bar{r}}_s \quad (2.8)$$

The reference orbit for this work is modelled as a secularly precessing ellipse and can be written in differential form as

$$\ddot{\bar{r}}_s = -\frac{\mu\bar{r}_s}{r_s^3} + \bar{f}_s \quad (2.9)$$

where \bar{r}_s is the position vector to the reference orbit in a non-rotating, geocentric coordinate system as in Equation (2.2) and \bar{f}_s is the perturbing accelerations that result in a secularly precessing ellipse. The substitution of Equations (2.2) and (2.9) into Equation (2.8), results in the Encke formulation,

$$\ddot{\bar{\epsilon}} = -\frac{\mu\bar{r}}{r^3} + \frac{\mu\bar{r}_s}{r_s^3} + \bar{f} - \bar{f}_s \quad (2.10)$$

Extreme care was taken to define the reference orbit for these simulations, since possible problems may result in this formulation if the reference orbit nearly equals the true orbit or if it does not remain close to the true orbit. With the first problem, a significant loss of numerical accuracy may result from the subtraction of nearly equal terms. However, this problem can be overcome by arranging the computations for the first two terms of Equation 2.10 in an appropriate form. To achieve increased accuracy, the Encke vector, ϵ , must remain significantly smaller

than either the true or reference position vectors which means that the reference orbit must not deviate substantially from the true orbit. The choice for the reference orbit used in these simulations was provided by *Lundberg* [1986].

2.2 Initial Conditions

The initial conditions ($\tau = 0$.) for the true and nominal ephemerides were provided by *White* [1987]. The true orbit's initial conditions were especially designed so that the final state after exactly 32 sidereal days will be very nearly the same as the initial conditions. They were determined using the University of Texas Orbit Processor (UTOPIA) and are given below in Table 2.1. The initial conditions for the nominal orbits shown in Table 2.2 were also estimated using UTOPIA, by fitting the ephemerides of the true orbits in a least squares sense with a different model to simulate an actual situation.

Table 2.1 Initial Conditions for the 'True' Orbit

Satellite 1:

$$\begin{aligned} X_1 &= 262.16184162 \text{ m}, & Y_1 &= -150104.5682242 \text{ m}, & Z_1 &= 6515224.696995 \text{ m}, \\ V_{X_1} &= -4.81851974 \times 10^{-2} \text{ m/s}, & V_{Y_1} &= -7816.577574349 \text{ m/s}, & V_{Z_1} &= -179.5770526472 \text{ m/s}, \end{aligned}$$

Satellite 2:

$$\begin{aligned} X_2 &= 262.89992177 \text{ m}, & Y_2 &= 149884.9023112 \text{ m}, & Z_2 &= 6515227.869697 \text{ m}, \\ V_{X_2} &= -4.76637746 \times 10^{-2} \text{ m/s}, & V_{Y_2} &= -7816.587219218 \text{ m/s}, & V_{Z_2} &= 179.4189749253 \text{ m/s}, \end{aligned}$$

Table 2.2 Initial Conditions for the Nominal Orbits**Satellite 1:**

$$X_1 = 251.82011984 \text{ m}, \quad Y_1 = -150205.8333573 \text{ m}, \quad Z_1 = 6515206.75655362 \text{ m},$$

$$V_{X_1} = -8.617240919 \times 10^{-2} \text{ m/s}, \quad V_{Y_1} = -7816.5813004031 \text{ m/s}, \quad V_{Z_1} = -179.65789276711 \text{ m/s},$$

Satellite 2:

$$X_2 = 254.34316160 \text{ m}, \quad Y_2 = 149823.0882622 \text{ m}, \quad Z_2 = 6515206.44534594 \text{ m},$$

$$V_{X_2} = -8.650294014 \times 10^{-2} \text{ m/s}, \quad V_{Y_2} = -7816.6011900852 \text{ m/s}, \quad V_{Z_2} = 179.39406524579 \text{ m/s}$$

2.3 Encke Reference Orbits

The numerical integration of both the true and nominal orbit simulations used the same Encke reference orbits that are described in Section 2.1.2. The orbital parameters used to generate these reference orbits are listed in Table 2.3.

Table 2.3 Encke Reference Orbit Mean Orbital Elements

	<u>Satellite 1</u>	<u>Satellite 2</u>
Semimajor Axis, a (m)	6523600.811305	6523599.627289
Inclination, i (deg)	90	90
Longitude of Ascending Node, Ω (deg)	90	90
Argument of Periapse, ω (deg)	0.0	0.0
Eccentricity, e	0.0	0.0
Mean Anomaly, M (rad)	1.593311064614	1.547312542033
Node Rate, $\dot{\Omega}$ (rad/sec)	0.0	0.0
Argument of Perigee Rate, $\dot{\omega}$ (rad/sec)	0.0	0.0
Modified Mean Motion, \dot{M} (rad/sec)	$1.1963632130262 \times 10^{-3}$	$1.1963633652585 \times 10^{-3}$

2.4 The Gravity Model

The gravity model, OSU86F, used in the GRM high precision simulation was created at Ohio State University [Rapp & Cruz, 1986]. It contains a set of constant geopotential coefficients complete to degree and order 360. The gravitational parameters used in this model are given in Table 2.4.

Table 2.4 Gravity Model for the True Orbits

Initial Greenwich Hour Angle,	$\alpha = 100.3399460 \text{ deg,}$
Earth's Rotational Velocity,	$\dot{\omega}_e = 7.2921158553066 \times 10^{-5} \text{ rad/s}$ $= [15.04106864 \text{ deg/hr},$
Earth's Gravitational Parameter,	$\mu = 3.986004404 \times 10^{14} \text{ m}^3/\text{s}^2,$
Earth's Mean Radius,	$a_e = 6378137.0 \text{ m,}$
Maximum Degree of Geopotential:	360,
Maximum Order of Geopotential:	360

The Goddard Earth Model 10B (GEM10B) used for the nominal orbit was created at the *Goddard Space Center* and is discussed by *Lerch et al* [1981]. Coefficients up to degree and order 36 plus some additional coefficients (up to order 82) that produce resonance effects on the GRM orbit were included also. The gravitational parameters for this model are:

Table 2.5 Gravitational Model for the Nominal Orbits

Greenwich Hour Angle,	$\alpha = 100.3399460 \text{ deg,}$
Earth's Rotational Velocity,	$\dot{\omega}_e = 7.2921158553066 \times 10^{-5} \text{ rad/s}$ $= [15.04106864 \text{ deg/hr}],$
Earth's Gravitational Parameter,	$\mu = 3.9860064 \times 10^{14} \text{ m}^3/\text{s}^2,$
Earth's Mean Radius,	$a_e = 6378145.0 \text{ m,}$
Geopotential:	G10B complete to degree and order 36 with adjusted resonant coefficients of orders 16, 17, 33, 49 and 82

2.5 The One-Way Doppler Range-Rate Algorithm

Gravity anomalies will be indirectly measured by the Satellite-to-Satellite Tracking System (SST) that uses an integrated one-way Doppler system to calculate range-rates between the proof masses of the two satellites. Simultaneously, while the lead satellite's (A) narrow-beam antenna transmits two signals at 42 and 91 GHz directed towards the trailing satellite (B), the trailing satellite's antenna transmits two signals at the same frequencies towards the leading satellite. These two frequencies, that are broadcast continuously, were chosen to filter out ionospheric effects. When the line-of-sight distance between the satellites varies, the frequency of the signals are doppler shifted. These doppler-shifts are measured by comparing the signals to a 5 GHz reference signal. Satellite-to-satellite range-rates are then computed from the doppler-shifts. Finally, gravity anomalies can be evaluated using these range-rates with various techniques.

The one-way doppler algorithm simulates the doppler measurement by first calculating the time of flight (TOF= Δt) of each signal of the same frequency. If both satellites receive each other's signal at t_i then the trailing satellite (B) transmitted a signal to the lead satellite at time $t_i - \Delta t_{Bi}$ and the leading (A) transmitted a signal to the trailing satellite at time $t_i - \Delta t_{Ai}$. The path length or the distance between the satellites is calculated by subtracting the position vector of the transmitting satellite at time $t_i - \Delta t_i$ from the position vector of the receiving satellite at time t_i . This requires interpolating the states of each satellite at the time of transmission. For each satellite, the range or distance, ρ_i , that their signals have travelled must be iterated until the following equations hold true,

$$\rho_{Ai} = | \bar{r}_A(t) - \bar{r}_B(t - \Delta t_{Bi}) | = c (\Delta t_{Bi}) \quad (2.11)$$

$$\rho_{Bi} = | \bar{r}_B(t) - \bar{r}_A(t - \Delta t_{Ai}) | = c (\Delta t_{Ai}) \quad (2.12)$$

where Δt is the TOF of the corresponding signal and c is the speed of light in a vacuum. An average of each satellite's simultaneously measured distance is then taken so that the path length of the signal that arrives at time t_i is

$$\rho_i = \frac{\rho_{Ai} + \rho_{Bi}}{2} \quad (2.13)$$

Finally, the integrated range-rate measurement at t_i is determined by subtracting the previously measured range from the current range value and dividing by the interval between measurements, h , which for this simulation was taken to be four seconds, i.e.,

$$\dot{\rho}_i = \frac{\rho_i - \rho_{i-1}}{h} \quad (2.14)$$

The analytical equation for the instantaneous range-rate is

$$\dot{\rho}_{\text{INST}} = \frac{\bar{\rho}_{\text{INST}} \cdot \dot{\bar{\rho}}_{\text{INST}}}{\rho_{\text{INST}}} \quad (2.15)$$

where the instantaneous range vector is the difference between the position vector of the leading (\bar{r}_A) and trailing satellites (\bar{r}_B),

$$\bar{\rho}_{\text{INST}} = \bar{r}_A - \bar{r}_B \quad (2.16)$$

ρ_{INST} is the magnitude of the instantaneous range vector, and $\dot{\bar{\rho}}_{\text{INST}}$ is the time derivative of $\bar{\rho}_{\text{INST}}$.

Instantaneous range-rates from Equation (2.15) were calculated along with the integrated one-way doppler range-rates from Equation (2.14) and compared. These results are presented in Chapter 3.

2.6 The KSGFS Numerical Integrator

A time saving, but highly accurate numerical integration algorithm, KSGFS [Lundberg, 1985], was used for the creation of the ephemerides of all orbit simulations. The KSGFS package is a multi-step, fixed mesh, class II numerical integrator that uses a constant stepsize (h) with the general formulation (Adams' type) of the Predict-Evaluate-Correct-Evaluate (PECE) Algorithm. The accuracy of the KSGFS integrator is a function of the order of the integrator (NORD), the constant step size (h), and the starting convergence criterion (ALIM). The order of the integration, which represents the number of function evaluations that are stored within the back-difference table, was set at 10, the stepsize was set at 4 seconds, and the starting convergence criterion was set at 10^{-16} .

2.7 The Computational Facilities

All computations within this study were carried out on the University of Texas System Center for High Performance Computing (CHPC) Cray X-MP/24 supercomputer located at the Balcones Research Center in Austin. The CFT 1.15 fortran compiler under the Cray Operating System (COS) was used to process all software. Using a 64 bit word with a 48 bit mantissa, the Cray X-MP/24 provides approximately 14 decimal digits of numerical accuracy in single precision arithmetic operations.

Since the evaluation of the Earth's geopotential requires 90 percent of the CPU computational time, it is essential that its recursion algorithms are completely vectorizable. Studies of these algorithms were performed prior to the actual simulation study by *Schutz et al* [1987] at Cray's Mendota Heights computer facility on the CRAY X-MP/48 and on the Cray X-MP/24 at U.T.. From these tests, the 32 day high precision orbit simulation with a geopotential of degree and order 360 was estimated to require approximately 20 hours of Cray's CPU time for a numerical integration step size of 4 seconds. Actual simulation time costs are reviewed in Chapter 3.

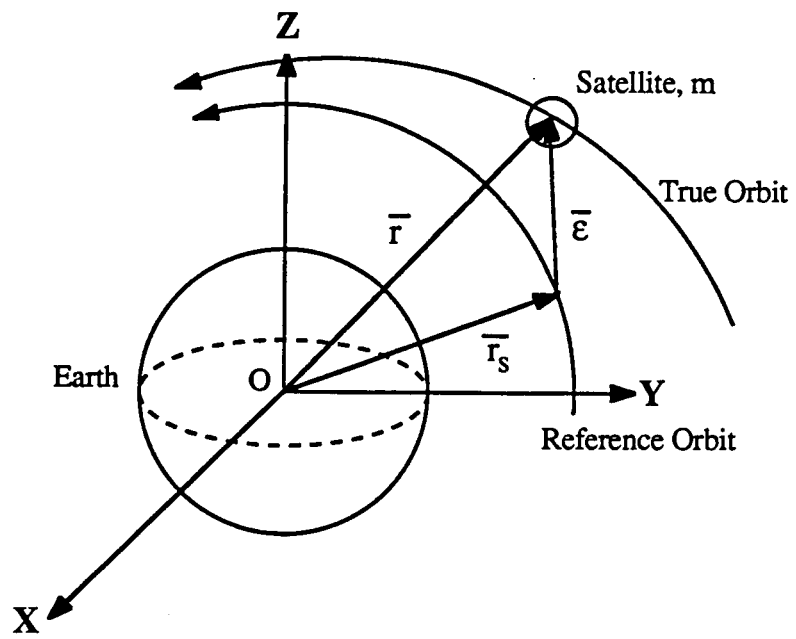


Figure 2.1 The Encke Vector

CHAPTER III

SIMULATIONS OF THE TRUE AND NOMINAL ORBITS

This chapter presents the results of creating the true and nominal orbit simulations performed at the University of Texas at Austin. Section 3.1 describes the predicted computer costs (CPU time) involved in creating a high precision orbit simulation that will represent the true or actual GRM orbits. The actual computer cost is discussed in Section 3.2 along with the results of the true orbit simulation. The comparison of the final conditions with the initial conditions is also presented in Section 3.2 to illustrate how closely they fulfill the groundtrack repeat requirement.

3.1 Pre-evaluation Computer Cost Analysis

Before submitting the costly High Precision Orbit Simulation, a computer cost analysis was performed on the software that was used generate it. It was found that evaluating the gravity accelerations by using the geopotential routine (GRAV) takes 90 percent of the execution costs (CPU time) on the Cray X-MP/24. The cost analysis involved timing a number of executions with the GRAV routine using different geopotential files in both single and double precision. Three geopotential files were investigated in this study: OSU322 [*Rapp*, 1981], OSU300 and OSU86F [*Rapp et al*, 1986] from the Ohio State University. The goal was to find highly accurate but efficient software to evaluate the geopotential. The results are presented in Table 3.1.

Table 3.1 Computational Costs on the Cray X-MP/24 Supercomputer

Geopotential File	Degree X Order	Precision	Cost/Evaluation
OSU 322	180 X 180 + 300 X 10	Single	8.34 ms
OSU 322	300 X 300	Single	12.4 ms
OSU 322	180 X 180 + 300 X 10	Double	0.460 s
OSU 300	300 X 300	Single	17.5 ms
OSU 86F	360 X 360	Single	23.6 ms
OSU 86F	360 X 360	Double	1.77 s

Since the Cray Fortran compiler does not vectorize double precision arithmetic, the timings per function evaluation are rather large. The OSU86F geopotential field was chosen for the high precision orbit simulation because it was the most recent file published that contains higher degree and order coefficients based on actual observations of surface gravity. With a 4 second integration stepsize and 2 function evaluations per integration step, the 32 day simulation was expected to take nearly 20 hours of CPU time on the Cray X-MP/24.

3.2 The True Orbit Simulation

With a four second integration step size, the 32-day repeating groundtrack mission required 19.2 hours of CPU time for the computation of 1.38 million function evaluations on the Cray X-MP/24 supercomputer. The final state (position and velocity) of the two "inner" satellites (proof masses) after 32 sidereal days is presented in Table 3.2. The ephemerides of both satellites were recorded on magnetic tapes at 4 second intervals for the 32 solar days. Also recorded on magnetic tapes were the Encke vector along with its first and second derivatives which represent the position, velocity, and acceleration with respect to the reference orbit; the true position and velocity vectors; the acceleration vector due to the nonspherical geopotential perturbations; and the Satellite-to-Satellite Tracking range-rate measurements. The 32 solar day ephemeris includes 691,200 data points.

Table 3.2 The Final Conditions of the True Orbit Simulation

At T = 2757250.896 seconds (32 sidereal days),

	Satellite 1	Satellite 2
X	263.71581564293 m	262.52773651901 m
Y	-151910.59425710 m	147270.45322817 m
Z	6514322.4662864 m	6514410.8338560 m
Vx	0.03922369100238 m/s	-0.03050865454835 m/s
Vy	-7817.5481419523 m/s	-7817.7162425634 m/s
Vz	-182.13650075972 m/s	175.89261824692 m/s

By comparing the initial longitude and latitude with the final longitude and latitude of each satellite, it was determined that the orbits repeat at the end of 32 sidereal days to within 1.78 km for the lead satellite and 2.52 km for the trailing satellite. This means the lead satellite misses its repeat location by 0.233 seconds, and the trailing satellite misses its repeat location by 0.331 seconds. As shown in Table 3.3 which compares the initial and final conditions of each satellite, the 32 sidereal day orbits resulted in very close repeats of their initial conditions, thus satisfying mission requirements.

Table 3.3 Comparison of the Initial and Final Conditions

	<u>Satellite 1</u>	<u>Satellite 2</u>
Initial Latitude:	88.68881 deg	88.69073 deg
Final Latitude:	88.67285 deg	88.71340 deg
Latitude Error:	0.015960 deg	0.022400 deg
Longitude Error:	0.000600 deg	0.001640 deg
Groundtrack Error:	1.780 km	2.5240 km
Time Error:	0.233 sec	0.33072 sec

3.3 The Nominal Orbit Simulation

The nominal simulation was determined by performing a least squares fit to the true ephemerides described above using the University of Texas Orbit Processor (UTOPIA). The fit required the adjustments of the zonals J_2 and J_3 and the first two pairs of the resonant coefficients at orders 16, 17, 33, 49, and 82 in the GEM10B gravity field. The initial conditions of the nominal orbit simulation were estimated

along with the above resonant coefficients by *White* [1987] and were presented in Chapter 2. The final conditions of the nominal orbit simulation at the end of 32 sidereal days are presented in Table 3.4.

It was desired to use a small geopotential field differing from the thruth model to simulate an actual mission. Such a field results in differences that exceed the mission requirements. Therefore, the nominal simulation was first estimated for the leading satellite using a 36 by 36 GEM10B gravity field. This baseline trajectory was then differenced from the true trajectory of this satellite in the radial, along-track, and cross-track directions. These differences were rather large and they did not meet the mission's specifications of 100 m in the radial and along-track directions and 300 m in the cross-track direction. It was determined that the spherical harmonic coefficients at orders 16, 17, 33, 49, and 82 were in resonance with the 160 km orbit since their periods are commensurate with an integer number of the satellite's daily revolutions. These resonant coefficients were seen to cause periodic variations in the along-track direction. For example, order 82's resonant period was found to be 32 days with an amplitude over 800 meters [*White*, 1987]. Therefore, the first two pairs of the harmonic coefficients, C_{nm} and S_{nm} , were estimated at these orders to reduce the residuals within the mission's specifications. However, these specifications were still not completely met so it was decided that the zonals J_2 and J_3 should also be estimated. Once the trajectory of the leading satellite was estimated with residuals to meet the mission specifications, the adjusted GEM10B gravity field was used to estimate satellite two's trajectory. The details of this estimation process for the nominal orbit are explained by *White* [1987].

Table 3.4 The Final Conditions of the Nominal Orbit Simulation

At T = 2757250.896 seconds (32 sidereal days),

	Satellite 1	Satellite 2
X	253.33113296 m	253.20268166 m
Y	-151930.52366132 m	147214.89761292 m
Z	6514302.05865142 m	6514389.94412363 m
Vx	0.02245143351 m/s	-0.05610810420 m/s
Vy	-7817.55836853513 m/s	-7817.73018629348 m/s
Vz	-182.16135321783 m/s	175.83304189105 m/s

3.4 RTN Differences Between True and Nominal Orbits

The true and nominal orbit simulations are compared by examining the radial (R), transverse (along-track, T), and normal (cross-track, N) components of the position vector difference along the entire trajectory of the 32 day orbit. These differences indicate the level of effort necessary to meet the orbit determination requirements of the mission. The prime concern of this study is the gravity mission which requires 3σ accuracy of 100 meters in the radial and 300 meters for along- and cross-track components. The differences between the true and the nominal orbits must remain below these requirements. The radial component of the differences versus time for the lead and trailing satellite (satellite 1 and satellite 2) are shown in Figures 3.1-a and 3.1-b, respectively. The transverse difference versus time are shown in Figures 3.2-a and 3.2-b for satellite one and satellite two, respectively. The normal differences are shown in Figures 3.3-a and 3.3-b. These graphs were generated by sampling data at a rate of five points per orbit.

As seen from these figures, the radial differences of both satellites remain between ± 55.0 meters; the transverse residuals of both satellites remain between $+200.0$ and -250.0 meters; and the normal differences of both satellites remain between ± 55.0 meters. Therefore, the nominal orbit simulation meets the requirements for the gravity mission, whereas the magnetic mission requirements (3σ) of 100 meters in the along-track direction are not satisfied. However this nominal orbit simulation will be used to improve gravity models so that eventually the magnetic mission's requirements can be met, or additional resonance terms can be estimated to further reduce the transverse differences.

3.5 Range-Rate Measurements

If the range-rate between the satellites could be instantaneously measured, then a plot of range-rate versus time for the 32 day true orbit simulation would have the characteristics shown in Figure 3.4. Range-rates during the beginning of the mission would range between ± 0.8 m/s, then increase gradually (± 0.9 m/s) near the end of 32 days.

Actual range-rate measurements made by the SST's integrated one-way Doppler system along the true orbit would resemble those shown in Figures 3.5-a and 3.5-b for the reception of the signal by satellite 1 and satellite 2, respectively. These plots also exhibit the trend described in the instantaneous plot. These simulated measurements were made by the one-way Doppler range-rate algorithm discussed in Chapter 2. Figures 3.6-a and 3.6-b show the time of flight (minus 1.0 millisecond) of the signal received respectively by satellite 1 and satellite 2 against time. Since the variations of the time of flight are on the order of $1.0 \mu\text{s}$, one millisecond is subtracted from the actual time of flight in order to show these small differences in the time of flight. With the speed of light (c) approximately 3×10^8 m/s, the corresponding distances between the satellites could also be represented by these figures. The average range-rates of these two measurements are presented in Figure 3.7, and the differences of the two measurements are presented in Figure 3.8. The two satellites' antennae are not measuring the same range-rates since each satellite is accelerating and decelerating at different times and signals are not instantly received. Figure 3.8 shows the differences between the two satellite measurements to range between ± 100 microns per second.

All measurements calculated by the one-way Doppler algorithm were compared against the ideal instantaneous measurements. Figures 3.9-a and 3.9-b

show the differences between the measurements calculated from the signal received using the one-way Doppler algorithm and the instantaneous measurement for satellite 1 and satellite 2, respectively. Figure 3.10 shows the difference between the instantaneous and the average of the two satellite range-rate measurements. These differences remained between +2.5 and -3.5 millimeters per second.

The nominal orbit simulation range-rate measurements were then compared to those from the true orbit. It is anticipated that the difference between the nominal and true measurements would be used to recover the true geopotential field. Figures 3.11-a and 3.11-b show the differences between the nominal and the true range-rate measurements against time as measured respectively by the signal received by satellite 1 and satellite 2. These differences remain below ± 35 millimeters per second.

Each of the above figures were generated by sampling the data at a rate of five points per orbit. The sinusoidal patterns seen on these graphs and the above RTN graphs are usually the results of this sampling rate and are generally not the true indication of the actual data.

It was found that the iterating procedure of the one-way Doppler algorithm to determine the time-of-flight of the transmitted signal of satellite two was unable to converge occasionally (15 points out of a total of 691,200 measurements). The computer code and algorithm was extensively evaluated to clear this problem, but the cause was not determined. Possibly, it could be due to round-off error when interpolating for the states of each satellite. The measurements calculated during these non-convergences did not meet the $1 \mu\text{m/s}$ accuracy required, and were ignored.

Figure 3.1-a Residuals between true & nominal orbits
for satellite one.

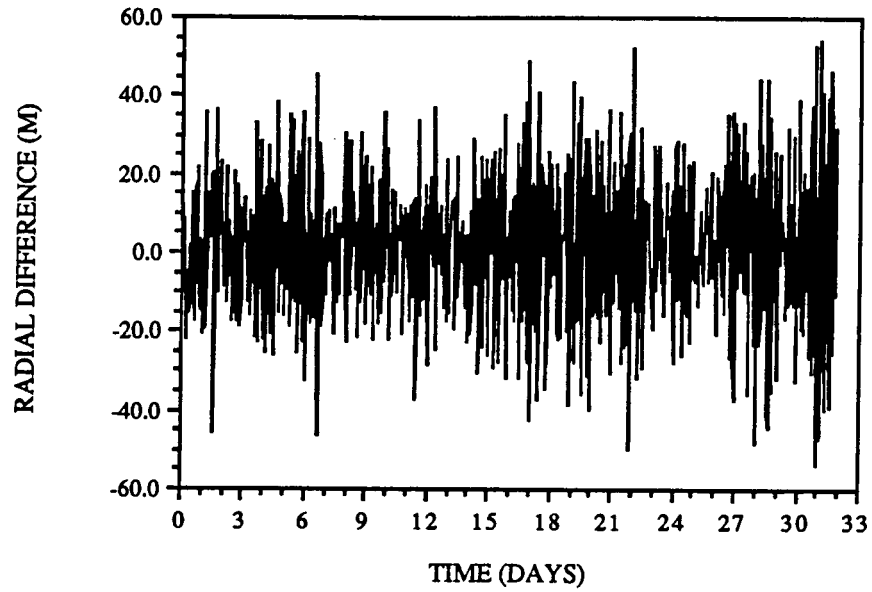


Figure 3.1-b Residuals between true & nominal orbits
for satellite two.

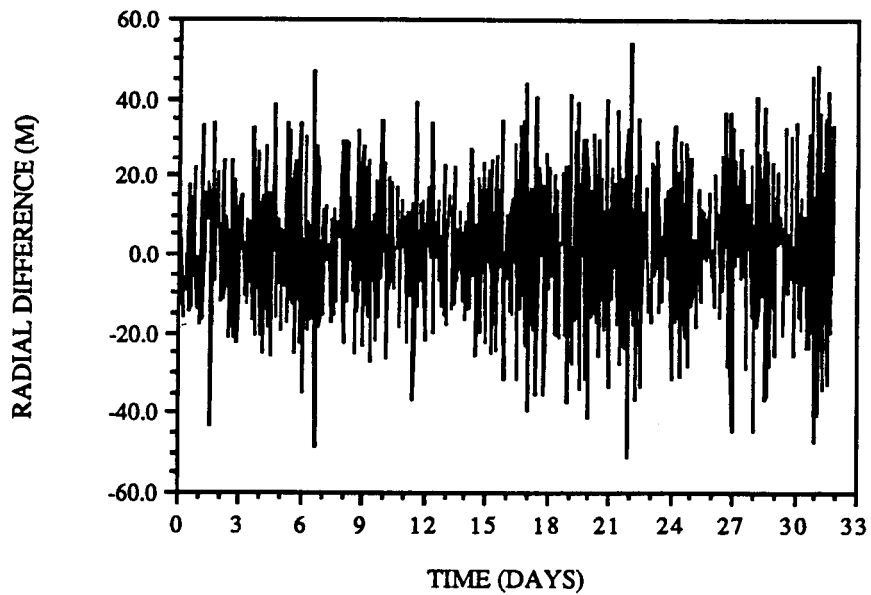


Figure 3.2-a Residuals between true & nominal orbits
for satellite one .

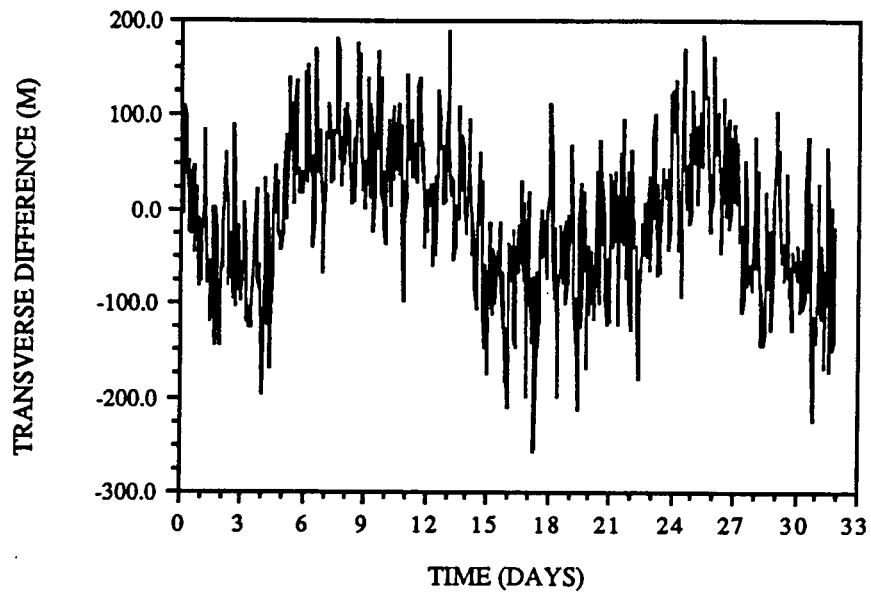


Figure 3.2-b Residuals between true & nominal orbits
for satellite two .

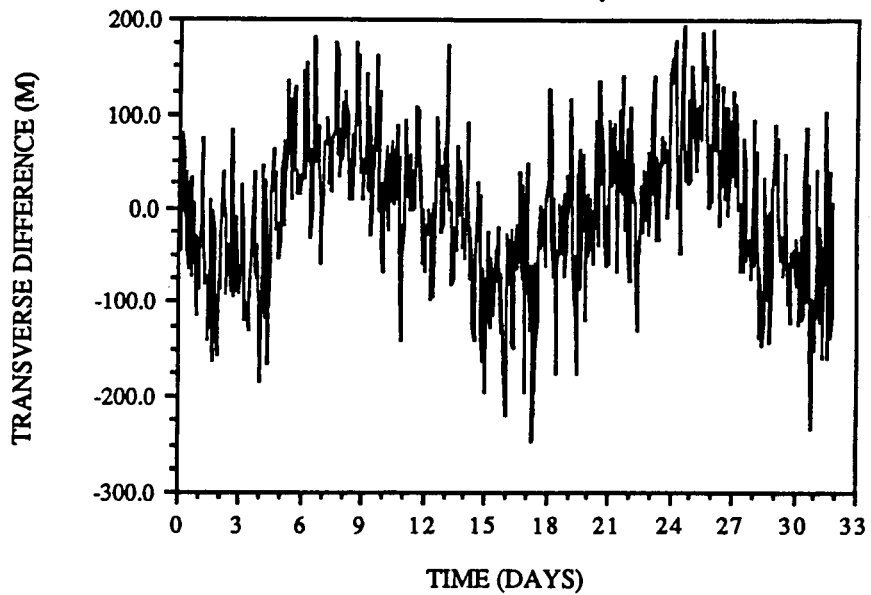


Figure 3.3-a Residuals between true & nominal orbits
for satellite one.

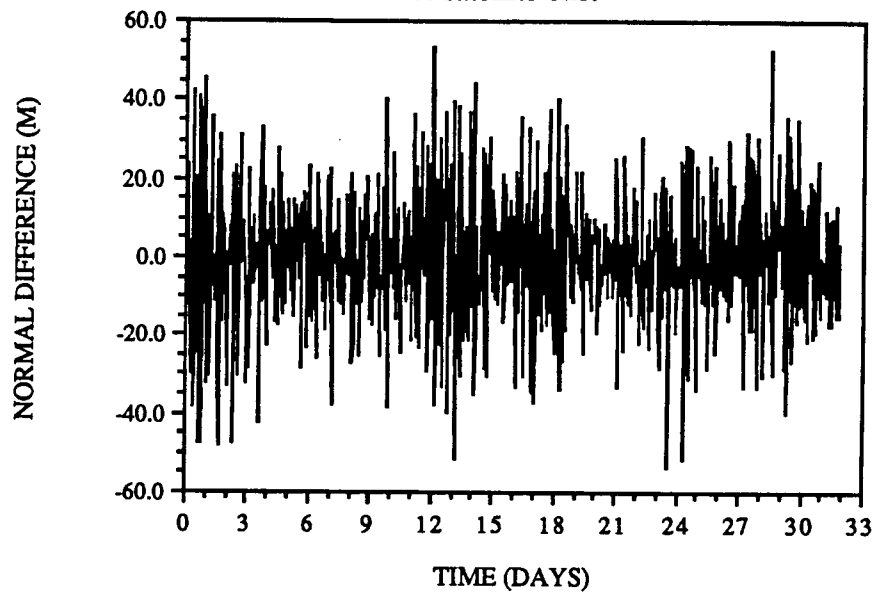


Figure 3.3-b Residuals between true & nominal orbits
for satellite two.

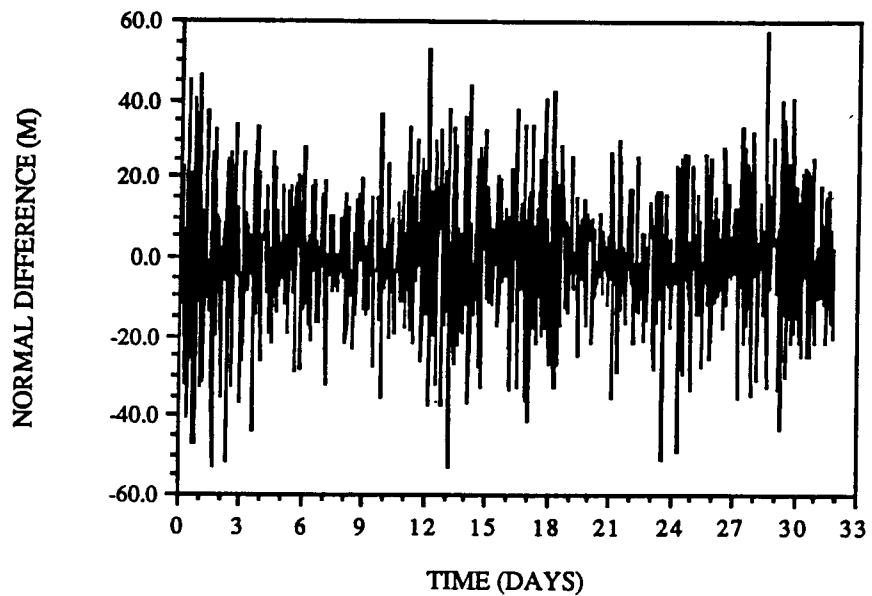


Figure 3.4 Instantaneous range-rate

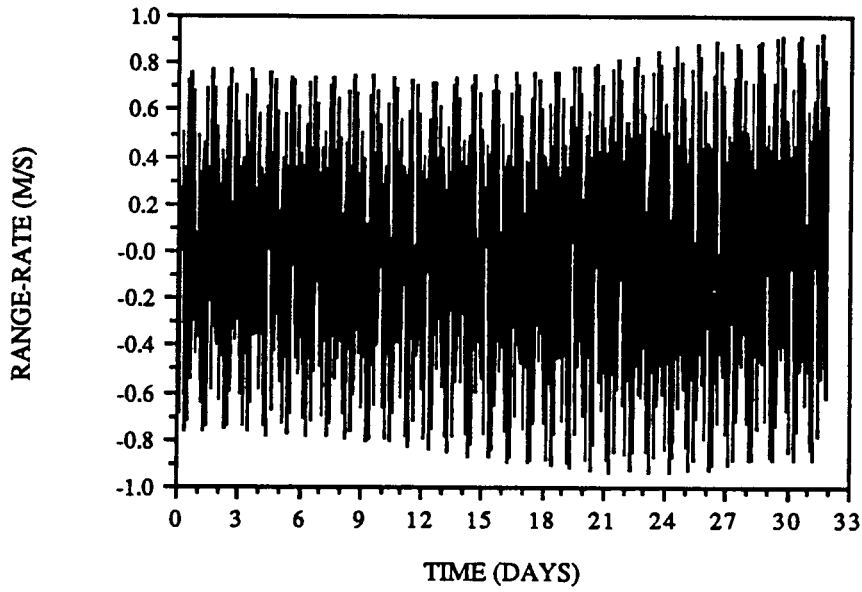


Figure 3.5-a Integrated One-Way Doppler measurements for signal received by satellite one.

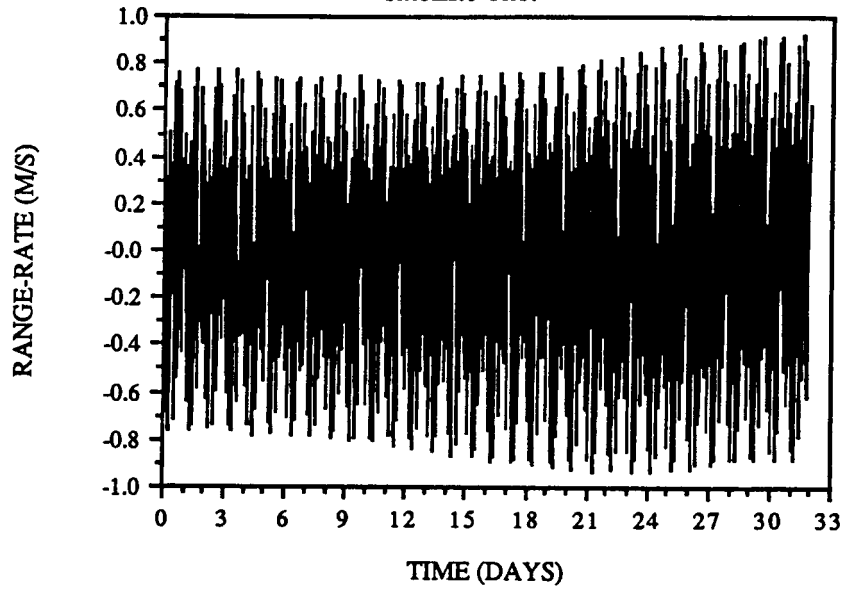


Figure 3.5-b Integrated One-Way Doppler measurements for signal received by satellite two.

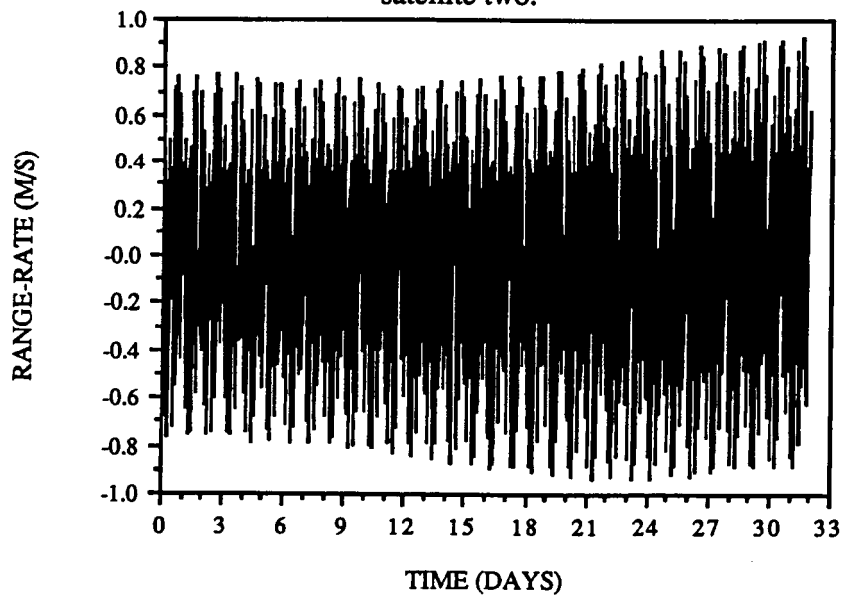


Figure 3.6-a Time of flight of signal received by satellite one.

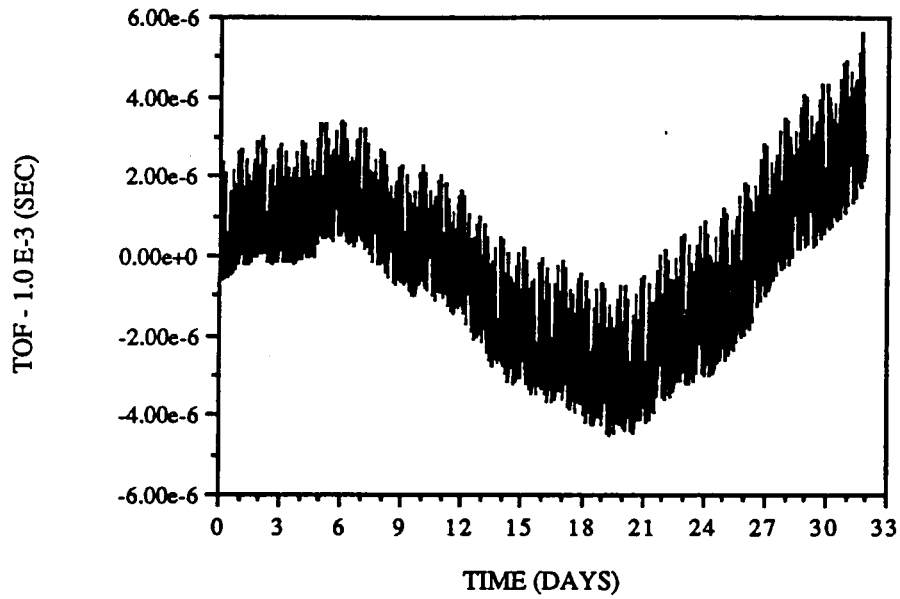


Figure 3.6-b Time of Flight of signal received by satellite two.

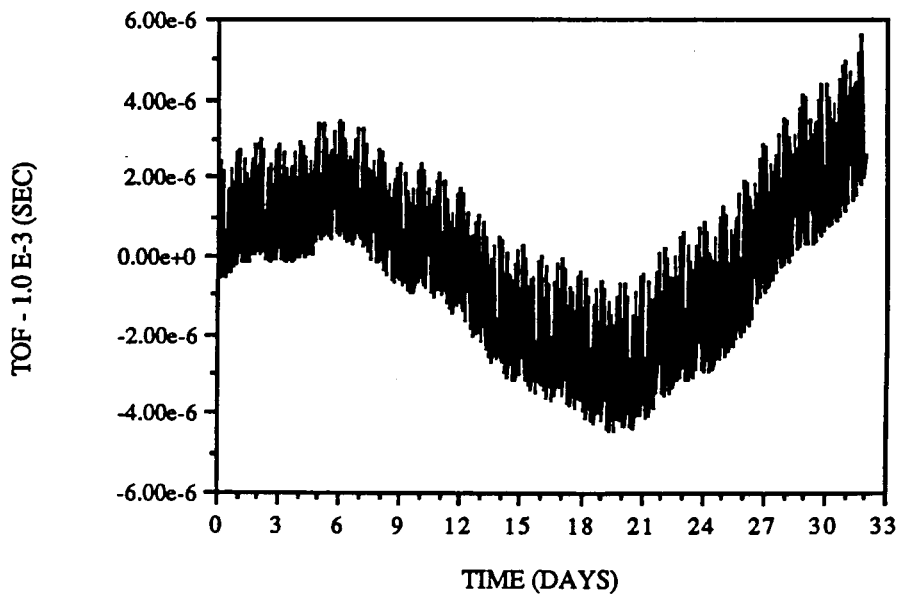


Figure 3.7 Average of both satellite's Integrated One-Way Doppler measurements

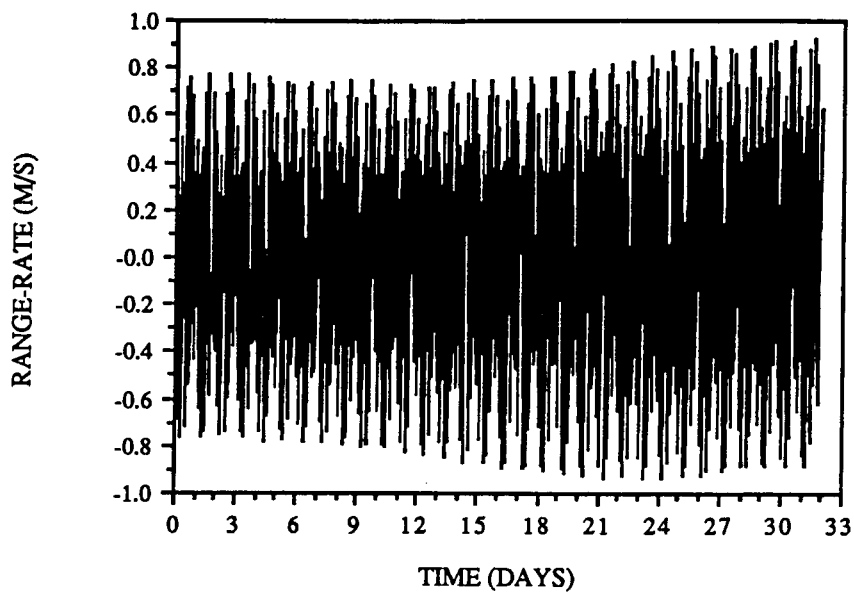


Figure 3.8 The difference between the integrated one-way doppler range-rate measured by satellite 1 and satellite 2.

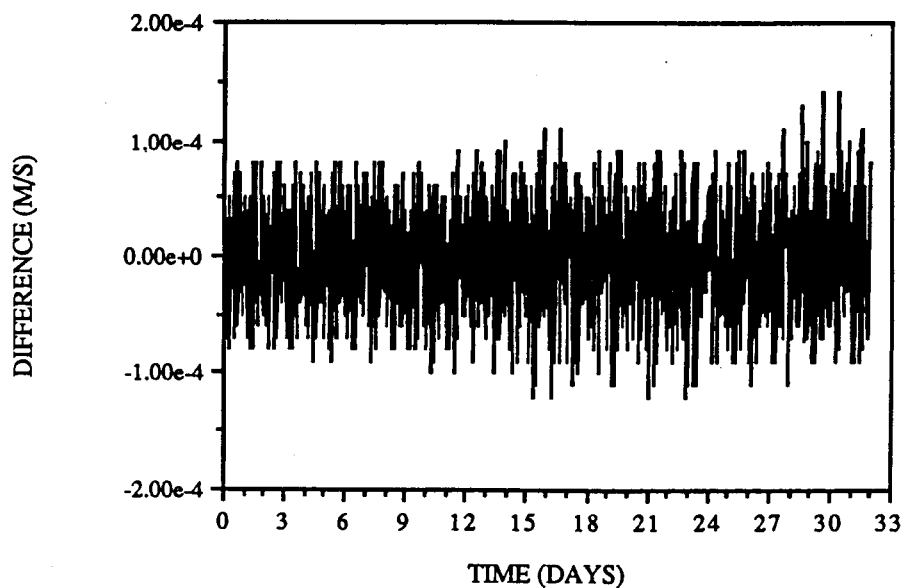


Figure 3.9-a The difference between satellite one and instantaneous range-rates.

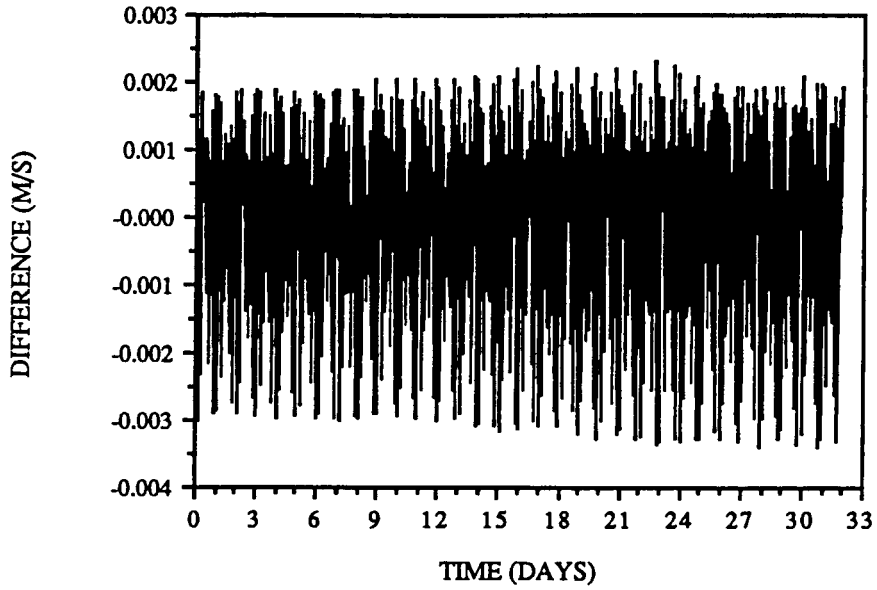


Figure 3.9-b The difference between satellite two and instantaneous range-rates.

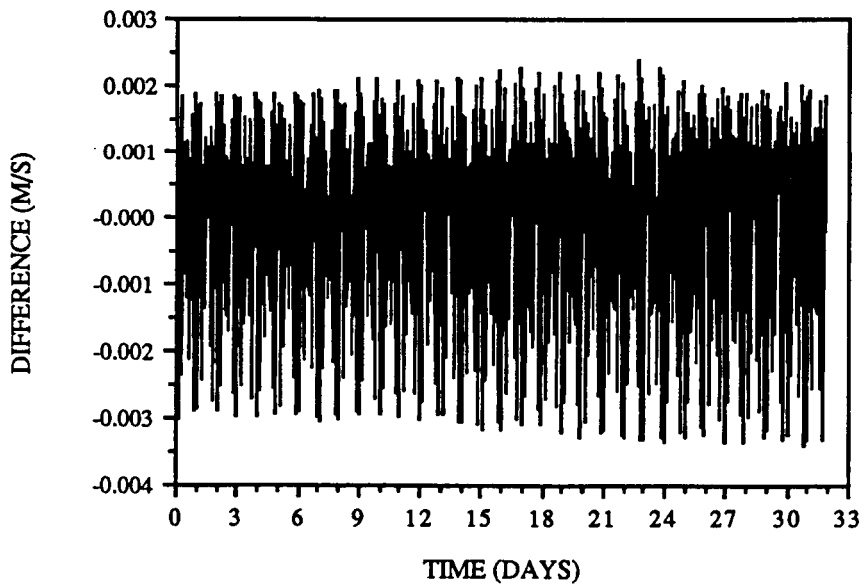


Figure 3.10 The difference between instantaneous and average range-rates.

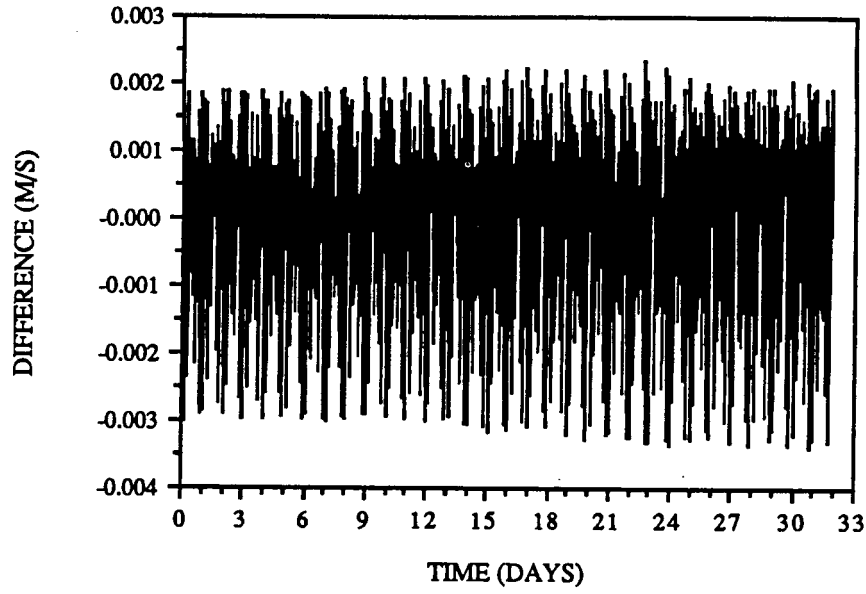


Figure 3.11-a Differences between true & nominal Integrated One-Way Doppler measurements for satellite one.

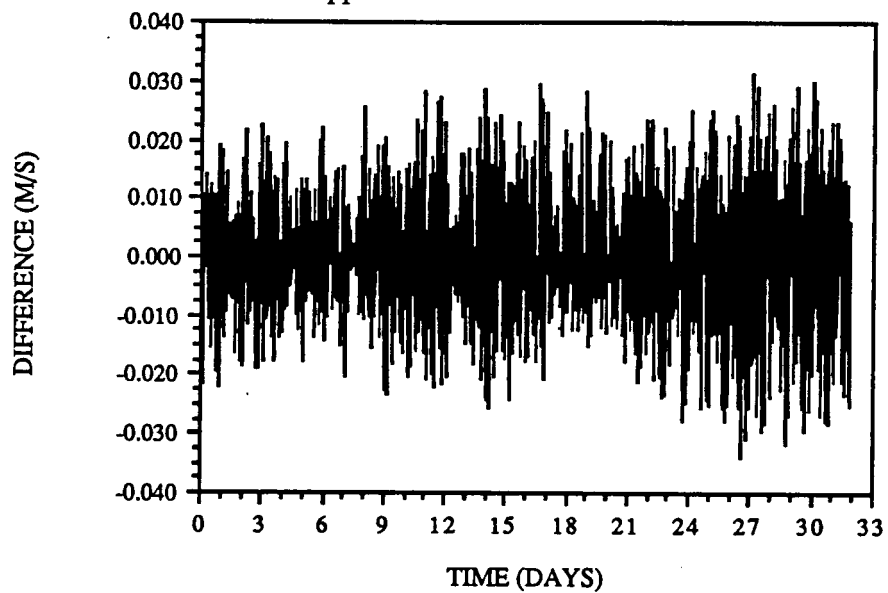
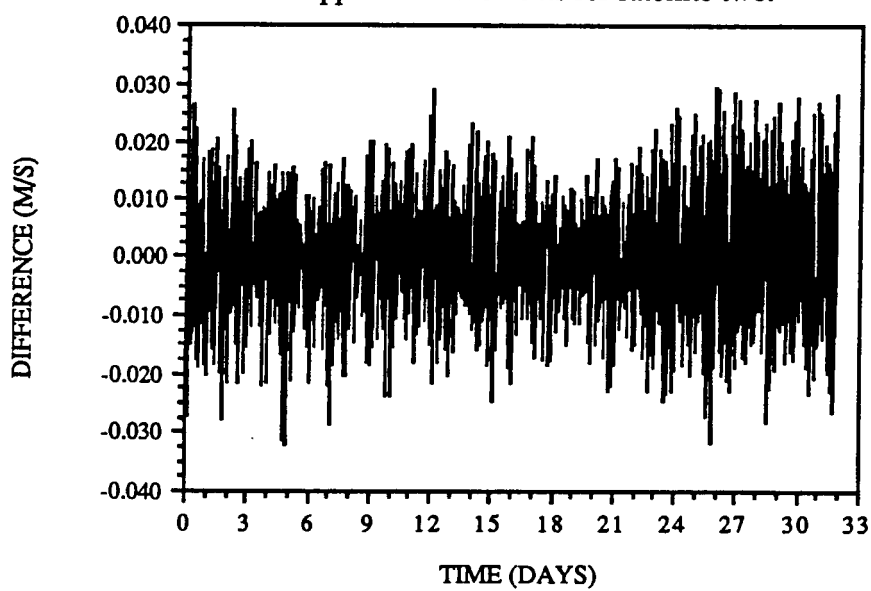


Figure 3.11-b Differences between true & nominal Integrated One-Way Doppler measurements for satellite two.



CHAPTER IV

SIMULATION OF THE DRAG COMPENSATION SYSTEM

This Chapter describes the mathematical formulae and control logic for the design of a Disturbance Compensation System (DISCOS) thruster control algorithm. The DISCOS is designed to offset effects due to drag and radiation pressure on the satellite, but only drag will be considered here.

A description of the DISCOS mechanism along with its history is discussed in Section 4.1. Section 4.2 describes the control logic of the computational algorithm used for this simulation. The equations of motion for this analysis are derived in Section 4.3 and Section 4.4 describes the force model used in this study. The numerical integration of the equations of motion of the proof mass and outer satellite is discussed in Section 4.5. The control laws, system logic and parameters for on-off thrusting switches is detailed in Section 4.6. Section 4.7 describes the ball-centering attitude control law that is coupled with the DISCOS translational control system so that small lift and sideslip forces can help reduce fuel expenditure. Finally, the results of this investigation are presented and the amount of fuel required to fire the thrusters for drag compensation during the six month mission is calculated in Section 4.8. Also, fuel expenditures are compared with previously published reports of *Keating et al* [1986] and *Ray & Jenkins* [1981] in Section 4.8.

4.1 The Disturbance Compensation System

As early as 1962, the feasibility of a mechanism that freed a satellite from atmospheric effects was first investigated by *B. Lange*, [1962]. Later, a "drag-free" mechanism, the DISTurbance COMPensation System (DISCOS), was developed in a joint effort by *The Johns Hopkins University Applied Physics Laboratory* and *the Stanford University Guidance and Control Laboratory* [1974] for the 1972 U.S. Navy's TRIAD satellite in an effort to improve navigation by satellite.

In the DISCOS design, a small satellite (the proof mass) is completely enclosed inside a cavity at the centroid of a larger outer satellite. This inner proof mass is then shielded from all nonconservative forces such as drag and radiation pressure. As the outer satellite is perturbed by these forces, its orbit deviates from the proof mass's orbit. When its deviation from the proof mass reaches a predetermined limit (the deadband region), appropriate thrusters fire from the outer satellite's propulsion system to keep its orbit coincident with the inner satellite's orbit and effectively negates the effects of nonconservative forces. This design was observed to maintain the proof mass of the TRIAD satellite within specified boundaries at an altitude of 700 km for 18 months using only three pounds of cold propellant [*JHU APL et al*, 1974].

While in orbit, the spherical proof mass orbits without contact with the outer satellite's spherical cavity, and its position relative to the outer satellite is monitored by a set of capacitance bridges (2 plates oppositely aligned on each of the 3 coordinate axes). External forces displace the outer satellite's electrical center of the capacitive cavity from the mass center of the proof mass, so that its capacity

changes as a function of its position relative to the proof mass's center of mass.

The TRIAD proved that a satellite equipped with the DISCOS mechanism can be essentially drag-free. Because a comprehensive gravity study such as GRM would require a low altitude orbit for extreme sensitivity to the geopotential, unpredictable, orbit decaying drag effects need to be constantly removed by an onboard control system. A review of the TRIAD DISCOS design indicated that its technology is adaptable to the GRM mission. Studies have shown that 0.1 $\mu\text{m/s}$ minimum sensitivity to the velocity of the proof mass with respect to the satellite's centroid can be achieved by the modification of the TRIAD DISCOS sensor [Keating *et al*, 1986].

The proposed GRM DISCOS mechanism is comprised of a 160 mm diameter spherical beryllium oxide housing (cavity) that includes a capacitive three-axis orthogonal coordinate position sensor and associated electronics while enclosing a 4 kg, 140 mm spherical aluminum proof mass and is located at the mass center of each satellite. Each entire DISCOS instrument, shown in Figure 4.1, is estimated to weigh 15 kg [Keating *et al*, 1986].

The outputs of the DISCOS sensor are used by the Guidance and Control System which controls the thrusting on all three body-fixed orthogonal axes. Each spacecraft uses eight along-track thrusters (4 forward and 4 aft) that are rated at 4 newtons apiece; eight 1 N thrusters (4 port and 4 starboard) for yaw momentum unloading and cross-track drag compensation; eight 1 N thrusters (4 top and 4 bottom) for pitch momentum unloading and vertical translation control; and eight 1 N thrusters (4 oppositely aligned) for roll momentum unloading. All thrusters are modelled as "idealized", instantaneous on-off force generators; and are fired in

pairs. Approximately 1400 kg of liquid hydrazine provided by fuel tanks placed equidistant from the proof mass to minimize mass attraction will be used to fuel each spacecraft's propulsion system. This gives a total impulse of 2.8 million newton-seconds of thrust to counteract drag and control each satellite's attitude [Ray, & Jenkins, 1981].

Since the Satellite-to-Satellite Tracking antennae are attached to the outer satellites, their precise displacement must be determined so that the relative velocity between the phase centers of the antennae can be determined to correct the SST data. As shown in Figure 4.2, the true range-rate (\dot{s}_T) is then

$$\dot{s}_T = \dot{s} + \dot{\delta}_{x1} + \dot{\delta}_{x2} \quad (4.1)$$

where \dot{s} is the measured range-rate provided by the SST and $\dot{\delta}_{x1}$ and $\dot{\delta}_{x2}$, respectively represent relative velocities of the leading and trailing spacecraft's SST antenna with respect to the proof mass [Keating *et al*, 1986].

According to Keating *et al* [1986], "the performance requirements of the DISCOS for the GRM mission are:

- 1.) Proof mass-to-spacecraft relative velocity knowledge within 0.1 $\mu\text{m/s}$ (1σ) with a 4 second averaging time.
- 2.) Three-axis disturbance compensation within 10^{-9} g, rms, over the frequency range of 0.001 to 0.5 rad/s."

In order to meet the 10^{-9} g compensation requirement, the proof mass (ball) must fly freely within the satellite's cavity without hitting its walls, or in other words, the outer satellite must follow the proof mass without touching it. Satellite/ball interactions due to mass attraction, electric and magnetic fields, residual gas pressure (inside the cavity) and radiation pressure are some of the

possible sources of error. The 1972 flight of the U.S. Navy TRIAD satellite proved that these disturbances can be kept below 10^{-11} g. It has been determined that motions caused by thruster firings will directly corrupt science data (Equation 4.1) unless it is determined to a $0.1 \mu\text{m/s}$ accuracy. Ball center of mass offset, ball shape, pick-off noise, thermal deflections and structural flexure are some of the errors associated with the proof mass velocity measurements provided by the capacitive sensor. Also, since the capacitors (one pair on each axis) exhibit nonlinearities outside a small linear range ($\sim\pm 1.0$ mm), the deadband limit is fixed at these boundaries. Therefore, the maximum distance the outershell can deviate from the proof mass is 1 mm (furthest ball excursion in all directions) before the corresponding thrusters turn on [*Keating et al*, 1986].

4.2 The Design of the Drag-Free Thruster Control Algorithm

The primary objective of the thrusting control algorithm is to compensate for the drag effects on the outer satellite while minimizing fuel consumption. It involves controlling the outer satellite's thrusters so that it precisely follows the drag-free orbit of the proof mass within required limits.

Both the along-track and cross-track thruster control models involve turning the appropriate thrusters on and off at the precise moments to keep the outer satellite's center of mass from deviating no more than 1 mm from that of the proof mass. The 160 mm diameter cavity allows the 140 mm diameter proof mass to drift within a 10 mm margin before it touches the wall. In general, the capacitance is a nonlinear function of proof mass displacement in the cavity. However, since the

compactive sensors behave linearly within a ± 1 mm region, the deadband zone (the thruster-on switch) is set at these limits. These on-off switches cause a contactor control limit cycle to occur in either the along-track (Figure 4.3) or cross-track (Figure 4.4) phase-plane diagrams. The thruster-on portions of the along-track limit cycle is represented by a parabolic arcs at the deadband regions in the phase-plane diagram as shown in Figure 4.3. The thruster-off portion is represented by a "coast arc" parabola in the phase-plane. The thruster-on/off switches occur at the intersection of these two parabolas. There is no steady-state limit cycle for the cross-track control law since there is no consistently predictable force in this direction. This law imparts a small inward velocity proportional to the proof mass distance from the deadband zone.

As drag affects the outer portion of the satellite, the proof mass moves forward with respect to the center of mass of the outer satellite with increasing speed. Eventually the proofmass approaches the forward deadband region inside the cavity which is represented by the parabolic thrust arc in Figure 4.3. The aft thrusters turn on for approximately 60 milliseconds causing the outer satellite to move ahead of the proof mass. Then drag slows the velocity of the proof mass with respect to the satellite's centroid to zero and the ball reverses direction and speeds back to the forward deadband region as shown by the parabolic coast arc in Figure 4.4.

The frequency and amplitude of the along-track limit cycle was chosen to enhance the accuracy of the post-flight ball velocity reconstruction. Due to uncertainties, satellite-to-satellite range-rate measurements taken during thruster-on times are not to be used in the gravity recovery. Therefore, a repeatable limit cycle is needed for filtering out the data recorded during these times. However, the

variation of drag along the satellite's orbit cause difficulties in achieving a precisely repeatable limit cycle. Also it is desirable to maintain a small amplitude limit cycle to remain within the linear range of the sensor, but with a small amplitude cycle, the thrusters fire more frequently causing an increase in fuel consumption and also affecting thruster reliability. Therefore, "the desired steady-state condition is a sequence of relatively short firing pulses and relatively long coast arcs," [Ray and Jenkins, 1982].

Unwanted disturbance forces such as electrical charge and self-gravity on the proof mass are an important source of error and the control law should minimize their effect on science data. Therefore, the average value of the proof mass excursions must be kept as close to zero as possible. According to Ray and Jenkins, [1982], "the average position on the parabolic arcs will be zero for $x_{\max} = 2 x_{\min}$, which has been chosen for the nominal along-track limit cycle on GRM," where x_{\max} is the maximum along-track excursion of the proof mass with respect to the outer mass (apex of thrust arc parabola) and x_{\min} is the minimum along-track excursion (apex of the coast arc parabola). So with these considerations, "the GRM limit cycle has been tentatively set at $x_{\max} = +1.0$ mm and $x_{\min} = -0.5$ mm."

Since the spacecraft's attitude affects the translational dynamics of the proof mass relative to the outer spacecraft through both aerodynamic forces and kinematic pseudo forces (centrifugal and Coriolis) and the attitude thrusters will produce a torque and a force when fired, the attitude and translational control laws must be coupled [Ray and Jenkins, 1982]. The ball-centering attitude control system explained in Section 4.7 is an example of this coupling.

4.3 The Equations of Relative Motion

Figure 4.5 shows the relative position of the inner satellite (proof mass) with respect to the outer satellite's center of mass. Both inner and outer satellites are modelled as point masses, however it is assumed that the mass attraction between the two is negligible. In a mean of 2000, equatorial, geocentric, inertial coordinate frame the position of the proof mass with respect to the outer satellite (outer mass) is

$$\bar{\mathbf{E}} = \bar{\mathbf{r}}_{pm} - \bar{\mathbf{r}}_{om} \quad (4.2)$$

where $\bar{\mathbf{r}}_{pm}$ is the position vector of the proof mass and $\bar{\mathbf{r}}_{om}$ is the position vector of the outer mass as referenced to the inertial coordinate system.

Taking the time derivative twice gives the proof mass's acceleration with respect to the outer mass as

$$\ddot{\bar{\mathbf{E}}} = \ddot{\bar{\mathbf{r}}}_{pm} - \ddot{\bar{\mathbf{r}}}_{om} \quad (4.3)$$

where the dynamical motion induced on the proof mass state is purely gravitational and is represented by the two-body acceleration plus accelerations due to a nonspherical Earth geopotential of degree and order 5,

$$\ddot{\bar{\mathbf{r}}}_{pm} = -\mu \frac{\bar{\mathbf{r}}_{pm}}{r_{pm}^3} + \bar{\mathbf{f}}_{g_{pm}} \quad (4.4)$$

The dynamical motion of the outer mass includes the two-body and nonspherical accelerations, but is perturbed by drag forces that are eventually counteracted by the thrusters. Therefore, the equations of motion of the outer mass is

$$\ddot{\bar{r}}_{om} = -\mu \frac{\bar{r}_{om}}{r_{om}^3} + \bar{f}_{g_{om}} + \bar{f}_{drag} + \bar{f}_{thrust} + \bar{f}_{BC} \quad (4.5)$$

In the above equations, μ is the Earth's gravitational parameter, $\bar{f}_{g_{pm}}$ and $\bar{f}_{g_{om}}$ respectively represent the gradient of the geopotential induced on the proof mass and the outer mass due to Earth's nonsphericity. Drag and thrust are respectively represented as \bar{f}_{drag} and \bar{f}_{thrust} . The term \bar{f}_{BC} is a small lift force in the radial direction or a sideslip force in the cross-track direction produced by pitching or yawing the outer mass at small angles with respect to the velocity vector, so that they will help center the proof mass in these directions. This ball-centering attitude control law is explained further in Section 4.7.

Finally, by substituting Equation 4.3 and Equation 4.4 into Equation 4.2, the equations of motion that govern the proof mass's state with respect to the outer mass are produced,

$$\ddot{\bar{e}} = -\mu \left[\frac{\bar{r}_{pm}}{r_{pm}^3} - \frac{\bar{r}_{om}}{r_{om}^3} \right] + \left[\bar{f}_{g_{pm}} - \bar{f}_{g_{om}} \right] - \bar{f}_{drag} - \bar{f}_{thrust} - \bar{f}_{BC} \quad (4.6)$$

The state vectors of the proof mass with respect to the inertial frame and with respect to the centroid of the satellite are propagated by numerically integrating Equations 4.4 and 4.6 as opposed to Equations 4.4 and 4.5. The Encke integration can be used to provide greater accuracy in the solution for the relative motion than the differencing of the numerical solution of the absolute positions.

4.4 The Force Model

To keep this model as simple as possible, forces due to three-body, temporal, and kinematic effects were not included in this analysis. Disturbance forces such as electrical charge on the proof mass and ball-satellite gravitational attraction are also not included in this analysis.

4.4.1 Geopotential Forces

The force induced on either the proof mass or the outer mass from the Earth's nonsphericity is respectively derived by the gradient of the geopotential,

$$\bar{f}_{g_{pm}} = \nabla U_{pm} \quad (4.7)$$

$$\bar{f}_{g_{om}} = \nabla U_{om} \quad (4.8)$$

where the geopotential, U , is expressed in the Pines formulation using direction cosines, which is discussed in Chapter 2 and represented by Equation (2.4). The OSU86F gravity model (discussed in Chapter 2) through degree and order 5 was used for the geopotential coefficients in the above calculations.

4.4.2 Drag

The drag force per unit mass induced on the outer satellite is

$$\bar{f}_{\text{drag}} = -\frac{C_D}{2m} S \rho V \bar{V} \quad (4.9)$$

where C_D is the outer satellite's coefficient of drag ($C_D = 3.5$), S is frontal area of the spacecraft ($S = 1.06 \text{ m}^2$), ρ is the density of the atmosphere, m is the mass of the satellite and \bar{V} is the velocity of the spacecraft with respect to the atmosphere,

$$\bar{V} = \dot{\bar{r}}_{pm} - \bar{\omega} \times \bar{r}_{pm} \quad (4.9)$$

The density of the Earth's atmosphere is much less predictable at altitudes above 125 km than at lower altitudes. The behavior of the atmosphere above 125 km is due to many complex processes, such as geomagnetic heating, sunspot activity (solar flux), seasonal latitudinal variation of helium and the lower troposphere, and gravitational attraction of Earth's geoid. These processes determine the densities of the atmospheric constituents nitrogen (N_2), argon (Ar), helium (He), oxygen (O_2 and O), and hydrogen (H) which are involved in producing the exospheric temperature.

The atmospheric density model used in this study was the Jacchia 1971 Atmosphere Model with modifications by Roberts [Jacchia, 1971]. This model calculates the densities of the atmosphere based on the aforementioned processes that raise or lower the exospheric temperature. Also included in this model are the analytical functions of the diurnal variation of the atmospheric bulge, the solar radiation flux at the 10.7 cm wavelength, the geomagnetic flux and the seasonal variations of the atmosphere. Since solar sunspot activity is known to occur with a 11 year cycle, the 10.7 cm solar flux and the geomagnetic flux during the actual GRM mission (planned for January - June, 1990's) are predicted by using the data

obtained from 1975 to 1986. The sunspot cycle's influence on the 10.7 cm solar flux and the geomagnetic planetary index for this period are presented in Figures 4.6 and 4.7, respectively.

The maximum sunspot activity occurred from 1980 to 1982, while the minimum sunspot activity occurred from 1985 to 1986. Atmospheric densities were calculated during these times to estimate the maximum and minimum densities the spacecraft would encounter during its mission in the 1990's. The predicted latitudinal atmospheric density variation for altitudes of 150 to 170 km during the vernal equinox of 1991 (high solar activity) and the summer solstice of 1996 (low solar activity) are shown in Figures 4.8 and 4.9, respectively. Here it is found that the density of the atmosphere at 160 km altitude varies between 6 to 17×10^{-10} kg/m^3 for high solar activity and between 3.5 to 11.5×10^{-10} kg/m^3 during the minimum activity.

Radial, along-track and cross-track drag components along the trajectory of the proof mass's 160 km high, drag-free orbit were computed using the density ranges stated previously for high and low solar activity; and they would resemble those shown in Figures 4.10 through 4.15. Since, at satellite altitudes, the drag induced on the spacecraft is proportional to the inverse of its mass, the drag will slowly increase during the lifetime of the mission as the fuel is expended. The drag values during the beginning (when the fuel tanks are full), the middle (half-full), and the end of the mission (empty) are also shown on the aforementioned figures.

Along-track drag per unit satellite mass range from -30 to -180 microns/sec^2 during high solar activity and from -20 to -140 microns/sec^2 during low solar activity. The unique patterns in these plots arise from the location on Earth that the

orbit passes. The polar orbit begins at the equator with a northerly direction; the peaks in the radial and along-track figures indicate the north and south pole regions where the magnitudes of drag are a minimum; the depressions indicate the equatorial regions where the magnitude of drag is greatest. The cross-track drag in Figures 4.14 & 4.15 arise from the rotation of the Earth and its atmosphere; the spacecraft's ascending track induces drag on its port side while the descending track induces drag on its starboard side; and cross-track drag is zero at the poles.

4.4.3 Thrust

The thrust per unit mass generated by the thrusters is modelled as an on-off step function. When fore or aft thrusters need to fire then,

$$\bar{f}_{\text{thrust}} = \begin{cases} +16 N \bar{t} & \text{aft thrusters on} \\ 0 N \bar{t} & \text{off} \\ -16 N \bar{t} & \text{fore thrusters on} \end{cases} \quad (4.10)$$

If cross-track thrusters need to fire then

$$\bar{f}_{\text{thrust}} = \begin{cases} + 4 N \bar{n} & \text{starboard thrusters on} \\ 0 N \bar{n} & \text{off} \\ - 4 N \bar{n} & \text{port thrusters on} \end{cases} \quad (4.11)$$

or if radial thrusters need to fire then,

$$\bar{f}_{\text{thrust}} = \begin{cases} + 4 N \bar{r} & \text{top thrusters on} \\ 0 N \bar{r} & \text{off} \\ - 4 N \bar{r} & \text{bottom thrusters on} \end{cases} \quad (4.12)$$

where \bar{r} , \bar{t} , \bar{n} denotes the radial, tangential (along-track) and normal (cross-track) directions, respectively, in a body-fixed RTN coordinate system.

4.5 Numerical Integration of the Equations of Motion

The Runge-Kutta Fehlberg 4(5) numerical integrator [Bettis, 1977] was used to integrate Equation 4.6 to determine the ephemeris of the proof mass's state vector with respect to the outer satellite and Equation 4.4 to determine the ephemeris of the proof mass. This fifth order, singlestep integrator allows for the integration of discontinuous functions such as the on-off switching of the thrusters. Embedded within this integrator is a fourth order method for automatic stepsize selection, but it is not used in this study.

The step size (h) was set at 0.5 seconds during coasting and 20 milliseconds during thrusting phases of the proof mass trajectory with respect to the outer mass. The step size is further reduced in both phases to reach switch boundaries precisely.

4.6 The Logic of the Thruster Control Algorithm

The thruster control algorithm was programmed in FORTRAN-77 using UT System CHPC's Vax 8600 front-end computer and compiled and executed on the

Cray X-MP/24 Supercomputer. Conditional IF statements simulate the control system by monitoring the proof mass's position relative to the outer satellite in an RTN coordinate system and determining when, for how long, and what thrusters need to fire.

The thruster control algorithm is implemented with the initial conditions and the various parameters listed in Tables 4.1 through 4.4. Starting at the beginning of the coast phase of the limit cycle with the numerical integration step size of 0.5 sec, the equations of motion of the proof mass with respect to the inertial frame and with respect to the centroid of the spacecraft (Equations 4.4 and 4.6) are integrated. At the end of every third step, the along-track position of the proofmass with respect to the centroid of the spacecraft and time is recorded. Upon recording the third data point, a parabola is fitted through the along-track position versus time curve and the along-track velocities of the ball with respect to the spacecraft's centroid is then calculated at these three positions. A parabola is fitted through the velocity versus position curve. Then the time of the aft thruster turn-on switch (deadband region) can be predicted at the intersection of this coast arc curve and an analytical representation of the velocity versus position curve (Equation 4.17) for the thrust phase of the limit cycle. If the difference of this time and the current time is less than the integration step size, the step size is reduced to this difference.

Once the aft thruster turn-on switch has been activated, the drag force per unit mass is estimated using the total time of coast and the thruster-on and -off switch velocities (Equation 4.20). The aft thrusters are turned on and the integration step size is changed to 20 milliseconds. While integrating the ball's state with respect to the spacecraft's centroid, the time of the thruster turn-off switch is predicted using the turn-on and turn-off velocities (explained below) and the estimated drag and

thrust per unit mass (Equation 4.21). Then, if the difference between the current time and the predicted time of thruster turn-off is less than the integration step size, the step size is reduced to this difference. Upon reaching the turn-off time, the aft thrusters are turned off and the limit cycle is repeated.

Since the drag and thrust per unit mass changes according to solar activity, location above Earth and fuel expenditure, the imparted velocity at the thruster turn-off switch must be changed throughout the mission in order to keep the ball excursions within the designed -0.5 mm limit. When this value is held constant throughout the mission, either too small or too large limit cycles result which cause either the aft thrusters to fire very frequently or the fore thrusters to fire, thereby greatly increasing fuel consumption. Therefore, this imparted velocity turn-off switch was determined for each phase (beginning, middle and end) of the mission such that the maximum ball along-track excursion remains within the designed -0.5 mm limit, but was held constant in each case. These values are listed in Table 4.4 for high and low solar activity, respectively, and they range from -0.44 to -0.24 mm/sec.

Unless unexpected disturbances cause the proof mass to reach the radial or cross-track ± 1.0 mm deadband regions, there is no need to fire radial or cross-track thrusters. Therefore, the computational thruster control algorithm outlined below involves only along-track drag compensation. All radial and cross-track excursions are controlled by the ball-centering attitude control laws explained in Section 4.7.

Along-track Drag-free Thruster Control Algorithm

1. Specify:
 - a) Initial Conditions of proof mass state with respect to the outer mass and the proof mass state in the inertial mean of 2000 coordinate frame
 - b) Thrust model parameters,
 - c) Gravity model parameters,
 - d) Drag model parameters, and
 - e) Control law parameters

The corresponding parameters used in this study are listed in Table 4.1 through 4.4 and Equation 4.10.

2. Set step-size to 0.5 seconds.
3. Integrate equations of motion Equations 4.4 and 4.6.
4. Record time and proof mass position with respect to outer mass every third step.
5. Once three data points of time and along-track position have been recorded along the coast arc phase, the along-track control law is implemented by fitting a parabola of the form

$$x = t^2 a_1 + t a_2 + a_3 \quad (4.14)$$

through the curve using a least squares approximation where a_1 , a_2 , a_3 are the coefficients that describe the curve, x is the along-track position and t is the time since the coasting phase began.

6. Determine velocities at these three data points,

$$\dot{x}_i = 2 t_i a_1 + a_2 \quad i = 1, 2, 3 \quad (4.15)$$

7. A parabola is fitted through the three position and velocity data points to

find the coefficients b_1, b_2 , and b_3 of the equation

$$\dot{x} = \dot{x}^2 b_1 + \dot{x} b_2 + b_3 \quad (4.16)$$

This equation is used to describe the phase plane characteristics of the coast arc in the along-track direction.

8. The analytical representation of the phase plane motion in the along-track direction during the thrust arc is,

$$\frac{1}{2} \dot{x}^2 = -(f_{\text{Drag}} + f_{\text{Thrust}})(x - x_{\text{max}}) \quad (4.17)$$

where x_{max} is the maximum excursion of the proof mass with respect to the outer satellite (taken to be +1.0 mm), f_{Thrust} is the thrust per unit satellite mass fired in the transverse direction, and f_{Drag} is the estimated transverse drag force per unit mass (initially set at a nominal value to initiate first control law predictions).

9. The velocity at the transition point from the coast arc to the thrust arc is defined by the intersection of Equations 4.16 and 4.17 and is predicted using the quadratic equation (positive root),

$$\dot{x}_{\text{ON}} = \frac{-B \pm \sqrt{B^2 - 4AC}}{2A} \quad (4.18)$$

where,

$$A = b_1 - \left[-\frac{1}{2(f_{\text{Thrust}} + f_{\text{Drag}})} \right] \quad (4.19)$$

$$B = b_2$$

$$C = b_3 - x_{\text{max}}$$

The position and time of deadband intersection (thruster turn-on switch, x_{ON} , t_{ON}) is calculated using Equations 4.16 and 4.15 respectively.

10. If the difference between the predicted turn-on switch time t_{ON} and the current time is less than the integration step size, the step size is reduced to this difference. The time of entire coast phase, t_{Coast} , is recorded.

11. Estimate drag accelerations during the coast phase

$$f_{Drag} = \frac{\dot{x}_{OFF} - \dot{x}_{ON}}{t_{Coast}} \quad (4.20)$$

where \dot{x}_{OFF} is the velocity at the thruster turn-off switch (thrust imparted velocity of the proof mass relative to the spacecraft) calculated using Equation 4.17 where x_{max} is the maximum excursion of the ball when the magnitude of drag is a minimum.

12. Turn-on transverse thrusters, change integration step size to 20 milliseconds.

13. Thruster turn-off time, t_{OFF} is then predicted using

$$t_{OFF} = \frac{\dot{x}_{ON} - \dot{x}_{OFF}}{-(f_{Thrust} - f_{Drag})} \quad (4.21)$$

14. If the difference between the current time along the thrust arc and t_{OFF} is less than the integration step size, reduce the step size to this difference to reach the turn-off switch precisely.

15. Once $t = t_{OFF}$, the thrusters are turned off and steps 2 - 15 are repeated.

Table 4.1 Initial Conditions

The initial conditions of the proof mass's state in inertial geocentric equatorial mean of 1950 system are:

$$\begin{array}{ll} X = 6538137.0 \text{ m}, & V_X = 0.001 \text{ m/s}, \\ Y = 0.001 \text{ m}, & V_Y = 0.001 \text{ m/s}, \\ Z = 0.001 \text{ m}, & V_Z = 7808.03729 \text{ m/s} \end{array}$$

And the initial conditions of the proof mass's state with respect to the outer satellite are:

$$\begin{array}{ll} \varepsilon_R = 0.00 \text{ mm}, & \dot{\varepsilon}_R = 0.00 \text{ mm/s}, \\ \varepsilon_T = 0.95 \text{ mm}, & \dot{\varepsilon}_T = X_{OFF} \text{ mm/s} \\ & \text{(see Table 4.4)} \\ \varepsilon_N = 0.00 \text{ mm}, & \dot{\varepsilon}_N = 0.00 \text{ mm/s}. \end{array}$$

Table 4.2 Parameters for the Gravity Model

$$\begin{array}{ll} \text{Earth's mean radius,} & A_e = 6378137.0 \text{ m}, \\ \text{Earth's gravitational parameter,} & \mu = 3.9860044 \times 10^{14} \text{ m}^3/\text{s}^2, \\ \text{Earth's rotational velocity,} & \dot{\omega} = 7.29211611 \times 10^{-5} \text{ rad/s}, \\ \text{Gravity Coefficients, } C_{nm} \text{ \& } S_{nm} \text{ from } 5 \times 5 \text{ OSU86F gravity field} & \end{array}$$

Table 4.3 Parameters for the Drag Model

Mass of satellite:	m	=	1334 kg,
Mass of Fuel:		=	<u>1400 kg</u>
Total Mass at launch from space shuttle,		=	2734 kg
at mission start (95% Full),		=	2664 kg,
middle of mission (50% Full),		=	2034 kg
near end of mission (5% Full),		=	1404 kg,
Satellite's projected cross-sectional area,	S	=	1.06 m ² ,
Satellite's coefficient of drag,	C_D	=	3.5,

Table 4.4 Parameters for the Control Laws

The maximum forward designed excursion, $X_{max} = +1.0$ mm,

The minimum aft designed excursion, $X_{min} = -0.5$ mm,

The thruster off switch, \dot{X}_{OFF} ,

	<u>95% Full</u>	<u>50% Full</u>	<u>5% Full</u>
High Solar Activity:	-0.308 mm/s	-0.352 mm/s	-0.437 mm/s
Low Solar Activity:	-0.240 mm/s	-0.274 mm/s	-0.330 mm/s

4.7 Ball-Centering Attitude Control Law

A ball-centering attitude control law is coupled with the DISCOS translational control system so that radial and cross-track excursions of the proof mass with respect to the outer mass can be stopped without firing the radial and cross-track thrusters. Figure 4.16 shows how a small pitch bias, α , about the cross-track axis,

produces a small aerodynamic lift force,

$$f_{\text{Lift}_R} \equiv f_{\text{Drag}_T} \alpha \quad (4.21)$$

Likewise, a small aerodynamic sideslip force can be produced to center the proof mass in the cross-track direction by introducing a small yaw bias, β , about the radial axis (Figure 4.17),

$$f_{\text{Sideslip}_N} \equiv f_{\text{Drag}_T} \beta \quad (4.22)$$

These angles are computed by the ball-centering attitude feedback control laws of the form

$$\alpha = -K_{1N} x_R - K_{2N} \dot{x}_R \quad (4.23)$$

$$\beta = K_{1R} x_N + K_{2R} \dot{x}_N \quad (4.24)$$

where K_{1R} and K_{2R} and K_{1N} and K_{2N} are the feedback gains about the radial and normal axis respectively (listed in Table 4.5). The gains, K_{1N} and K_{2N} , were determined by *Ray and Jenkins* [1982], and the K_{1R} and K_{2R} gains were determined in this study through an iterative process.

Table 4.5 Ball-Centering Attitude Control Gains

Pitch gains (about the normal axis),	$K_{1N} =$	3.0,
	$K_{2N} =$	200.0,
Yaw gains (about the radial axis),	$K_{1R} =$	100.0,
	$K_{2R} =$	3000.0.

4.8 Results

The GRM DISCOS simulation using the drag-free thruster control algorithm was performed during high and low solar activity and during the beginning (95% full), middle (50% full), and end (5% full) of mission to estimate fuel expenditures during the mission. Each simulation of one orbital revolution required approximately 86 seconds of CPU time on the Cray X-MP/24 supercomputer. The number of thruster firings and fuel expended per orbit and 6 month mission along with other pertinent data are presented in Table 4.6 and 4.7 respectively for the high and low solar activity simulations.

4.8.1 The Effectiveness of the Drag-Free Thruster Control Algorithm.

Along-track proof mass excursions with respect to the centroid of the outer mass against time for one orbit during high and low solar activity are shown in Figures 4.18-a, -b, and -c and Figures 4.19-a, -b, and -c when the spacecraft has respectively, 95% fuel, 50% fuel and 5% fuel of initial fuel onboard. Radial and cross-track proof mass excursions are shown in Figures 4.20-a, -b, and -c for high solar activity and Figures 4.21-a, -b, and -c for low solar activity. These excursions were plotted during two orbits to verify that they were not secularly increasing. Along-track phase plane diagrams in Figures 4.22-a, -b, and -c and Figures 4.23-a, -b, and -c show the limit cycles that are produced from the control laws respectively during the high and low solar activities.

The aforementioned figures demonstrate the ability of the thruster control

algorithm to offset effects due to drag and keep the GRM spacecraft essentially drag-free. The along-track phase plane diagrams show the clock-wise pattern of the limit control cycles where the nearly straight (actually parabolic) portion of the cycle at the +1.0 mm region is the thrusting arc from top to bottom and the band of parabolas with their apexes of +0.5 mm to -0.5 mm are the coast arcs from bottom to top. They show that when the proof mass reaches the aft deadband limit of + 1.0 mm inside the spacecraft's cavity with a positive approaching velocity, the along-track thrusters on the spacecraft fire from 55 to 105 milliseconds until a predetermined negative imparted velocity is achieved. Then the proof mass is seen coasting until a maximum excursion of -0.5mm relative to the spacecraft's cavity is reached at zero velocity. Drag then overcomes the thrusting effort and causes the proof mass to "fall" with positive velocity back to the deadband region.

4.8.2 The Effectiveness of the Ball-Centering Attitude Control Law

Figures 4.20 and 4.21(-a, -b, and -c) and 4.24 to 4.28 demonstrate the effectiveness of the ball-centering attitude control law to produce small lift and sideslip forces to center the proof mass in the radial and cross-track directions. Figures 4.20(-a, -b, and -c) and 4.21(-a, -b, and -c) show that the radial proof mass excursions deviate no more than +0.40 mm or no less than -0.32 mm from the centroid of the spacecraft. These figures also show that the cross-track ball excursions deviate between ± 0.60 mm.. Radial and cross-track relative velocities as a function of time are plotted along two orbits in Figure 4.24 during high solar activity and 50% fuel and are indicative of all high and low solar activity cases. The radial velocities range from -1.5 to +1.5 $\mu\text{m/s}$ while the cross-track velocities range

from -0.75 to $+0.75$ $\mu\text{m/s}$. Also indicative of all cases, the ball-centering attitude control pitch and yaw angles for the above case are shown in Figures 4.25 and 4.26 during two orbits. It is shown that very small pitch angles of 0.057 to 0.069 degrees are produced to counteract radial excursions while relatively large yaw angles of ± 3.4 degrees are needed to counteract the cross-track excursions. Finally, radial and cross-track phase plane diagrams for this case are shown in Figures 4.27 and 4.28. The irregularities at the beginning of each plot, especially in the cross-track curves, resulted from the initial guess of the magnitude of drag to initiate the algorithm. Once initiated the curves become periodic with the orbit; local minimum and maximum excursions are indicative of the drag induced on the spacecraft in these directions or its location above the Earth when compared to the drag profiles in Figures 4.10 through 4.15.

Without the ball-centering attitude control law, the radial and cross-track excursions would hit the ± 1.0 mm deadband regions causing both radial and cross-track thrusters to fire briefly every 100 to 200 seconds.

4.8.3 Imparted Velocity Thruster Turn-off Adjustments

The along-track phase plane diagrams in Figures 4.22 and 4.23 (-a, -b, -c) show the results of the velocity turn-off switch adjustments. Each diagram shows the maximum excursion to be approximately -0.5 mm, resulting in maximum coast arc times of 14 to 25 seconds (as indicated in Tables 4.6 and 4.7) depending on solar activity and the amount of fuel onboard. However, holding the imparted velocity turn-off switch constant through the drag variation of one orbit results in

minimum excursions of +0.50 mm for high solar activity and +0.60 mm for low activity. These minimum excursions result in relatively short coast times between 5.0 and 7.5 seconds (as indicated in Tables 4.6 and 4.7) which may not be acceptable for minimizing fuel consumption or for post ball reconstruction. Therefore, the control algorithm should be able to adaptively adjust the turn-off switch due to these effects. However, the selection of an adaptive control law is beyond the scope of this research.

4.8.4 Fuel Expenditure

Both drag and thrust per unit mass increase when fuel is expended because of the decrease in spacecraft mass. For this reason, three scenarios during the mission are studied: 1) the beginning of the mission (after orbit injection) when the spacecraft has approximately 95% fuel left onboard, 2) the middle of the mission with 50% fuel onboard, and 3) near the end of the mission when there is approximately 5% fuel left onboard. Since drag increases during high solar activity, fuel expenditure is expected to be much greater during this period than during low solar activity. To best estimate fuel expenditures, both high and low cases must be investigated.

The fuel expenditure for the GRM mission is estimated by first determining the mass fuel rate of the thrusters and the total thruster-on time during one complete orbital revolution about Earth. Then assuming that fuel consumption will be nearly constant through the entire six month mission, the fuel expended per orbit is multiplied by the number of orbital revolutions at the end of six months.

The mass fuel rate of the thrusters when fired is

$$\dot{m}_{\text{Fuel}} = \frac{F_{\text{Thrust}}}{g_e I_{\text{SP}}} \quad (4.25)$$

where F_{Thrust} is the total thrust produced by the aft thrusters, g_e is the Earth's gravity at the surface and I_{SP} is the specific impulse of the fuel. With an I_{SP} of 200 seconds and F_{Thrust} of 16 Newtons ($g_e = 9.81 \text{ m/s}^2$), the fuel mass rate is 0.0081633 kg/s.

The fuel expenditure for the entire six month mission can be estimated by using the above algorithm to find the total thruster-on time, t_{ONTotal} , for one orbital revolution about Earth. The fuel expended per orbit, is then

$$\frac{m_{\text{Fuel}}}{\text{Orbit}} = \dot{m}_{\text{Fuel}} t_{\text{ONTotal}} \quad (4.26)$$

and the mission fuel expenditure can be estimated by noting that the six month mission requires approximately 2953 revolutions about Earth.

As listed in Tables 4.6 and 4.7, thruster on-times varied between 75.5 to 105 milliseconds during high solar activity, and between 58.9 to 81.8 milliseconds during low activity. The number of firings per orbit rose from 423 during the beginning of the mission to 583 firings near the end for the high solar activity case and from 395 to 543 firings during the low activity. However, the total on-time per orbit from beginning to end of the mission was nearly constant at approximately 43.8 sec during high solar activity and 31.7 sec for low activity. The idea that the fuel expended per orbit is independent of the amount of fuel left in the tanks was proven by observing the values of fuel expended per orbit listed in Tables 4.6 and 4.7. Here, the fuel expended per orbit was also nearly constant at 0.357 kg/orbit during high solar activity and 0.256 kg/orbit for low activity. Finally, with

approximately 2953 orbital revolutions, fuel expenditure estimates of 763 and 1056 kilograms of hydrazine (as listed in Tables 4.6 and 4.7) were determined, respectively during the low and high solar activities.

These fuel expenditures were compared with other published GRM fuel expenditure estimates. According to *Ray and Jenkins* [1982], their DISCOS simulation resulted in a cycle time of 10-20 seconds and about two million firings for the six month mission. Using a totally diffuse reflection drag model for worst case estimates, their simulations estimated the fuel expenditure for a seven month mission to be approximately 1150 kg giving 2.6 million N-sec of total impulse to counteract drag. This corresponds to nearly 986 kg of hydrazine for a six month mission if the fuel consumption rate was constant during entire mission. Their optimistic fuel estimate used only purely specular reflection and required 660 kg for seven months which would correspond to 566 kg for six months. According to *Keating et al*, [1986], the Goddard Space Flight Center's Flight Dynamics Division determined the 180 day (six month) mission would require approximately 1051 kg of hydrazine using worst case assumptions such as high solar activity.

Table 4.8 lists the worst and best case fuel expenditures of each study. It shows that the results of this report were reasonably close when compared to the other studies; the results were 0.5% greater than *Keating et al*, [1986] and 7.0% greater than *Ray and Jenkins* [1982] for the worst case, and 35% greater than *Ray and Jenkins* [1982] for the best case.

Table 4.6 Results of the GRM DISCOS Simulation during High Solar Activity

	<u>95% Full (2664 kg)</u>	<u>50% Full (2034 kg)</u>	<u>5% Full (1404 kg)</u>
Imparted velocity	-0.30795 mm/s	-0.35244 mm/s	-0.43695 mm/s
No. of firings/orbit	423	484	583
No. of firings/6 month mission	1.25 million	1.43 million	1.72 million
Fuel expended/orbit	0.35749 kg	0.35741 kg	0.35767 kg
Six month fuel expenditure	1055.7 kg	1055.5 kg	1056.3 kg
Maximum thrust time	105.01 msec	91.76 msec	76.24 msec
Minimum thrust time	104.06 msec	90.93 msec	75.53 msec
Maximum coast time	19.392 sec	16.942 sec	14.075 sec
Minimum coast time	7.591 sec	6.248 sec	5.347 sec
Total thrust time/orbit	43.793 sec	43.783 sec	43.815 sec
Maximum estimated drag magnitude	86.140 $\mu\text{m/s}^2$	112.82 $\mu\text{m/s}^2$	163.44 $\mu\text{m/s}^2$
Minimum estimated drag magnitude	31.781 $\mu\text{m/s}^2$	41.624 $\mu\text{m/s}^2$	60.302 $\mu\text{m/s}^2$

Table 4.7 Results of the GRM DISCOS Simulation during Low Solar Activity

	<u>95% Full (2664 kg)</u>	<u>50% Full (2034 kg)</u>	<u>5% Full (1404 kg)</u>
Imparted velocity	-0.23957 mm/s	-0.27417 mm/s	-0.32999 mm/s
No. of firings/orbit	395	451	543
No. of firings/6 month mission	1.17 million	1.33 million	1.60 million
Fuel expended/orbit	0.25839 kg	0.25850 kg	0.25857 kg
Six month fuel expenditure	763.07 kg	763.39 kg	763.60 kg
Maximum thrust time	81.84 msec	71.51 msec	59.42 msec
Minimum thrust time	81.19 msec	69.94 msec	58.94 msec
Maximum coast time	24.959 sec	21.813 sec	18.134 sec
Minimum coast time	7.058 sec	6.167 sec	5.123 sec
Total thrust time/orbit	31.653 sec	31.667 sec	31.675 sec
Maximum estimated drag magnitude	67.889 $\mu\text{m/s}^2$	88.916 $\mu\text{m/s}^2$	128.81 $\mu\text{m/s}^2$
Minimum estimated drag magnitude	19.192 $\mu\text{m/s}^2$	25.136 $\mu\text{m/s}^2$	36.416 $\mu\text{m/s}^2$

Table 4.8 Comparisons of Fuel Expenditures for 6 Month Mission

	<u>This Report</u>	<u>Keating et al. [1986]</u>	<u>Ray & Jenkins. [1981]</u>
Worst Case	1056 kg	1051 kg	986 kg
Best Case	763 kg	N.A.	566 kg

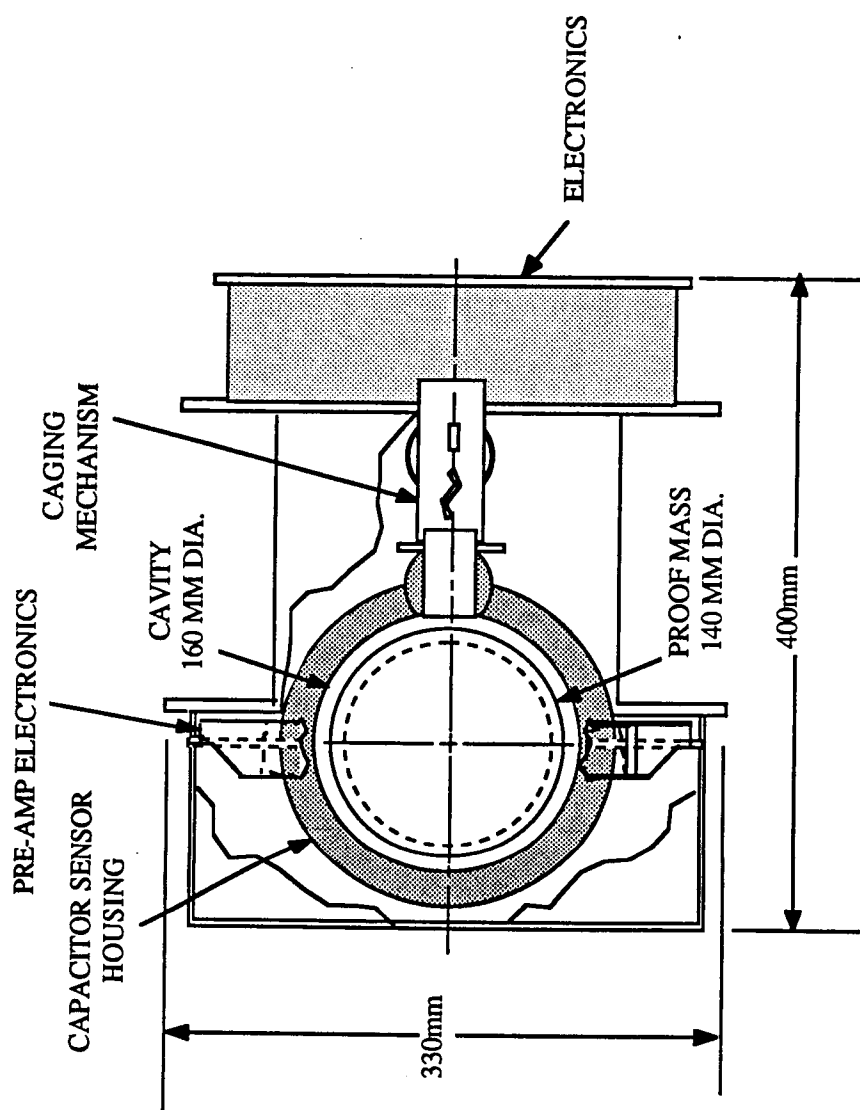


Figure 4.1 The GRM Disturbance Compensation System (DISCOS) Mechanism.

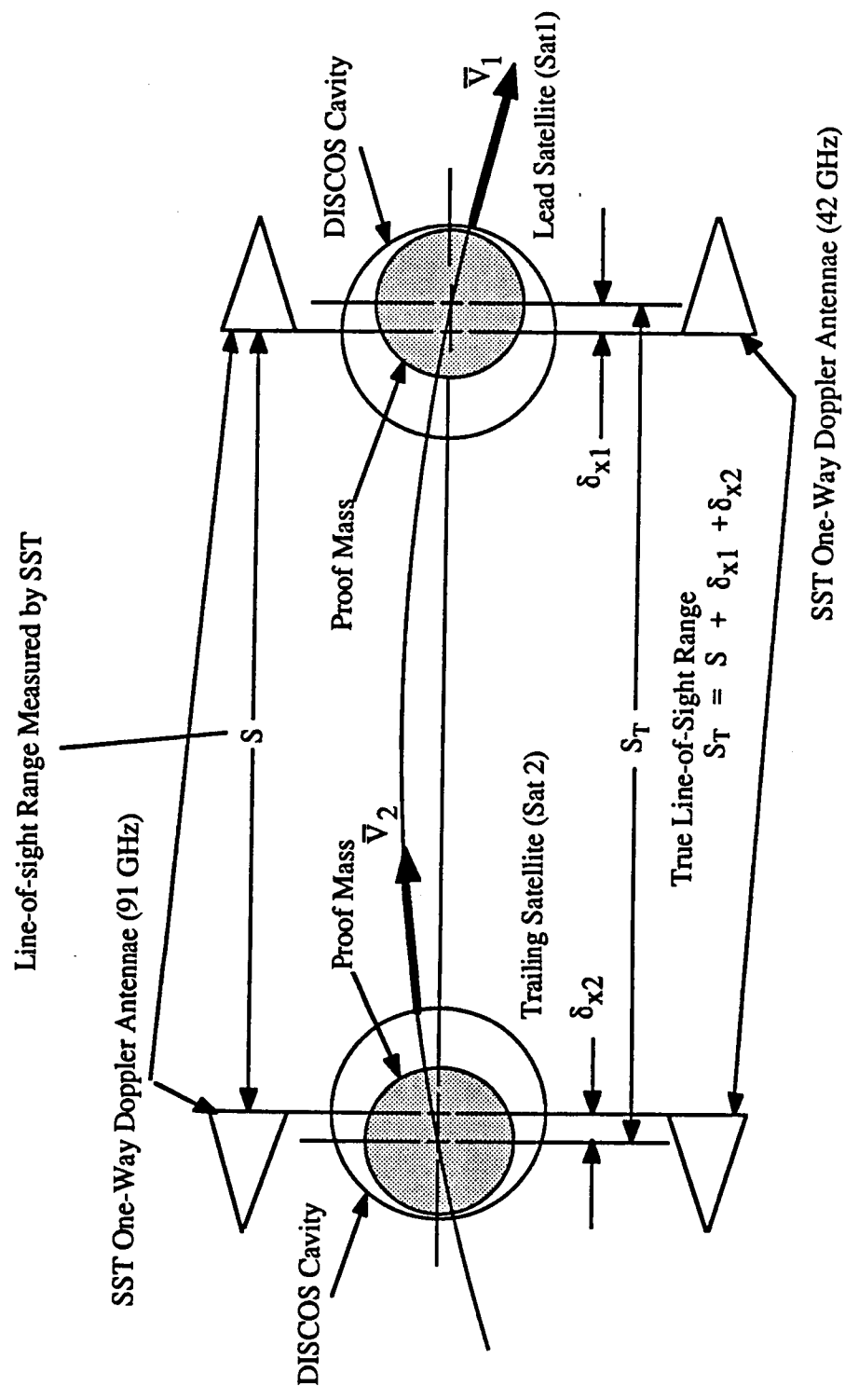


Figure 4.2 The GRM Ball-to-Ball Range Relationship.

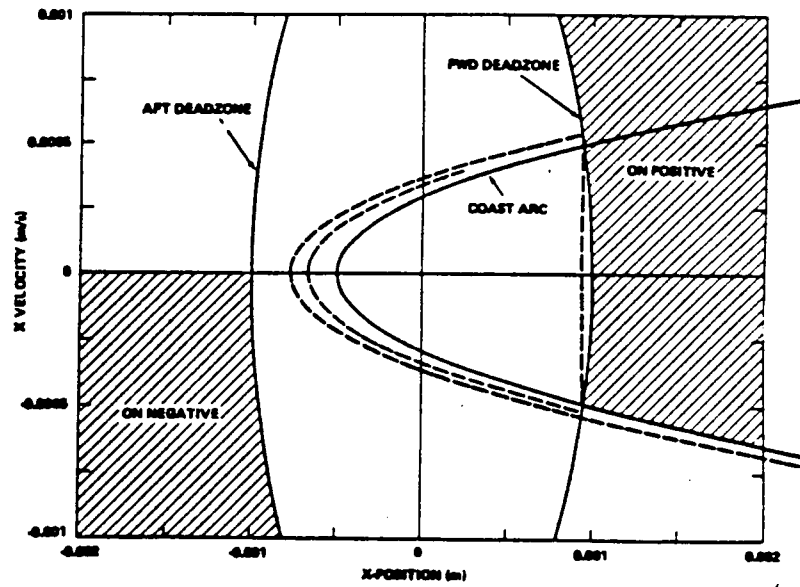


Figure 4.3 Along-track phase plane limit cycle, *Ray & Jenkins*, [1981].

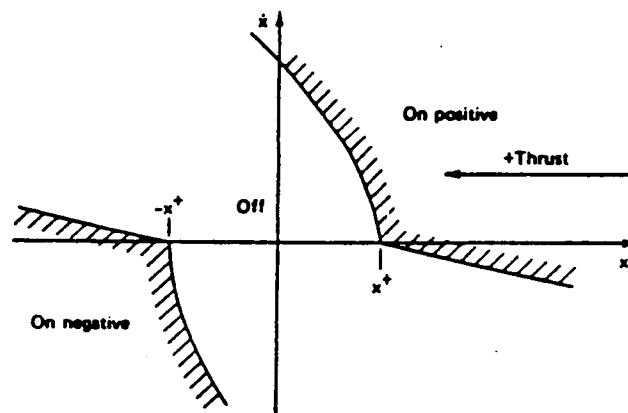


Figure 4.4 Cross-track phase plane limit cycle, *Ray & Jenkins*, [1981].

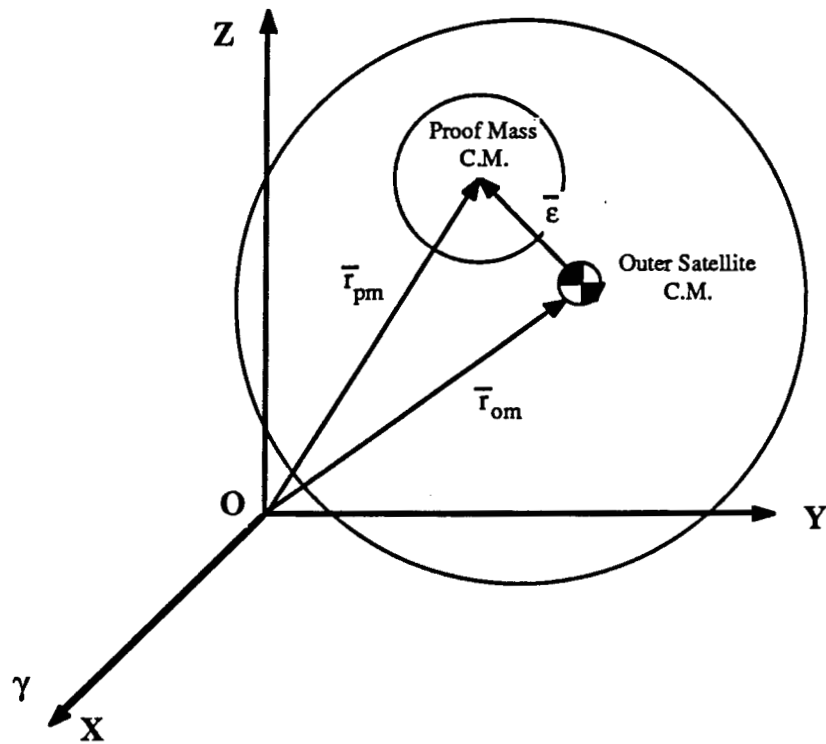


Figure 4.5 The Vector representing the Proof Mass with respect to the Outer Satellite

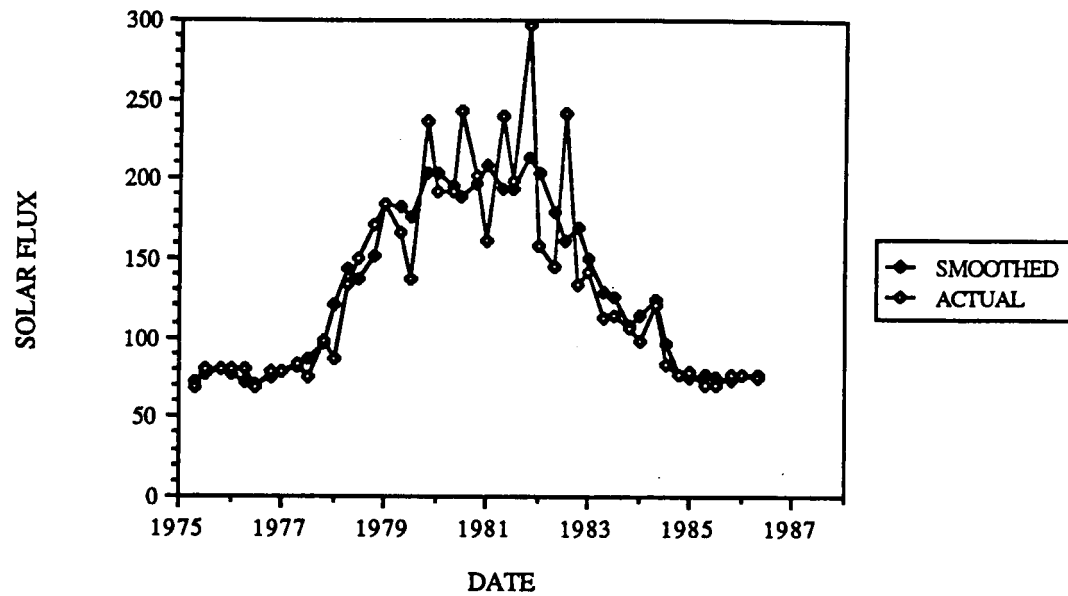
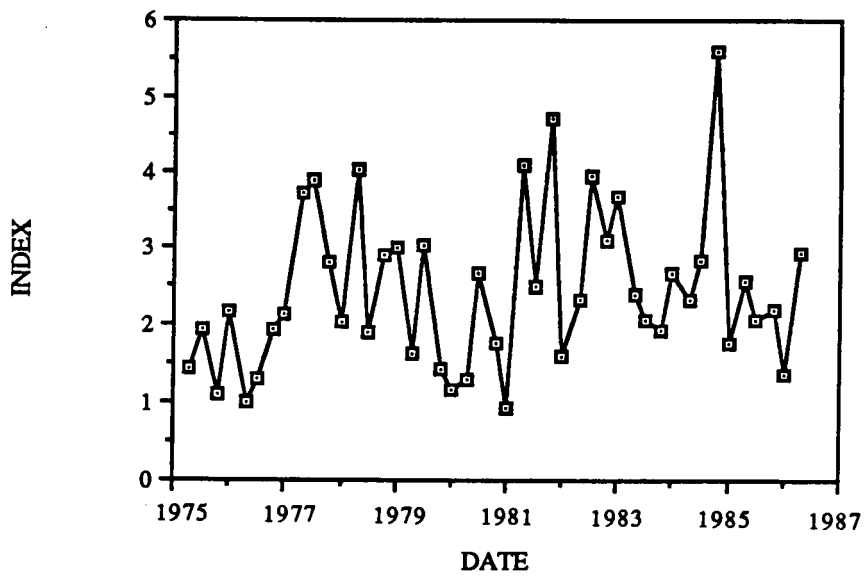
Figure 4.6 Solar flux data in 10^{-22} watts/m²/cycles/sec bandwidth.

Figure 4.7 The Geomagnetic Planetary Index



~~PRECEDING PAGE BLANK NOT FILMED~~

Figure 4.8 Predicted latitudinal atmospheric density variation for the vernal equinox of 1991 at GRM altitudes.

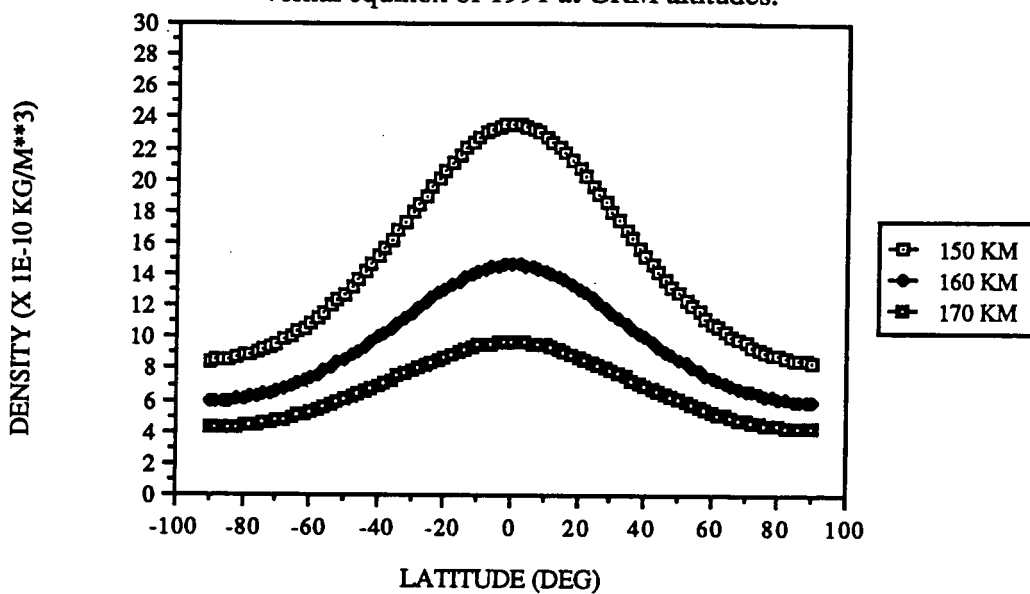


Figure 4.9 Predicted latitudinal atmospheric density variation for the summer solstice of 1996 at GRM altitudes.

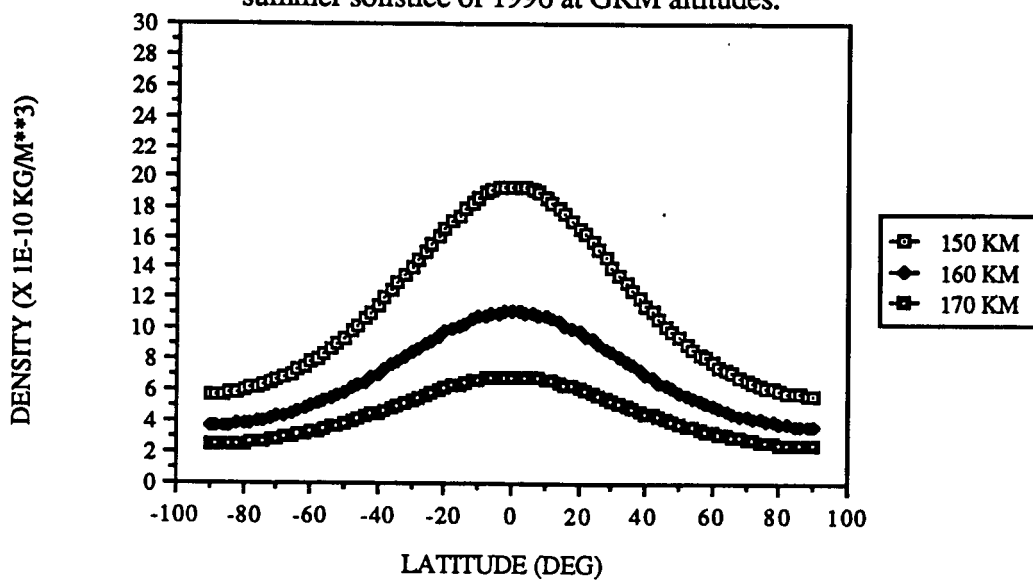


Figure 4.10 Predicted drag profiles along 2 GRM (160km) orbits on the vernal equinox of 1991 (high solar activity).

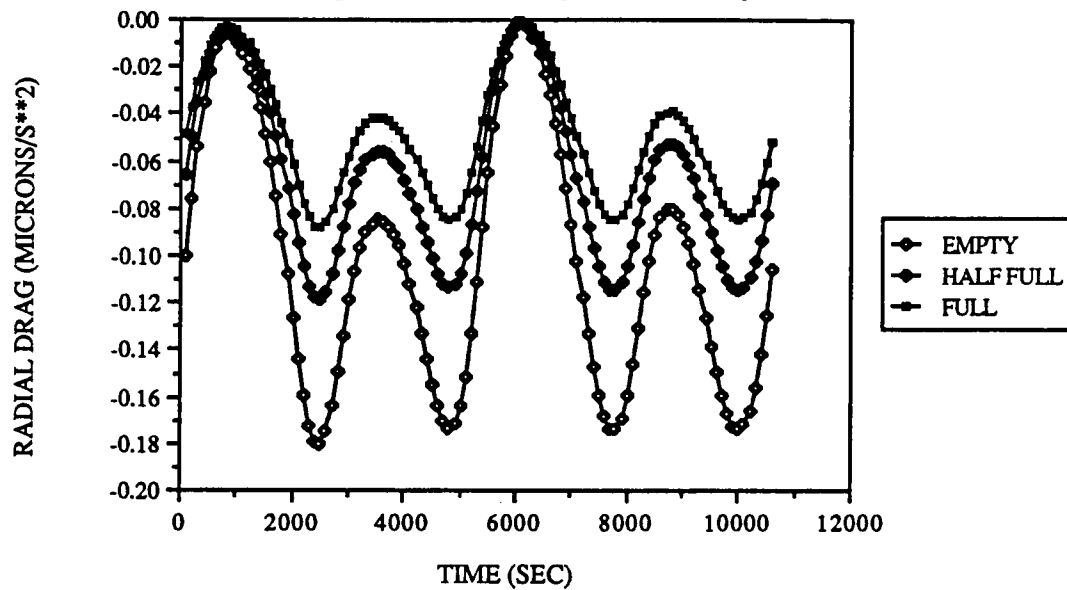


Figure 4.11 Predicted drag profiles along 2 GRM (160km) orbits on the summer solstice of 1996 (low solar activity).

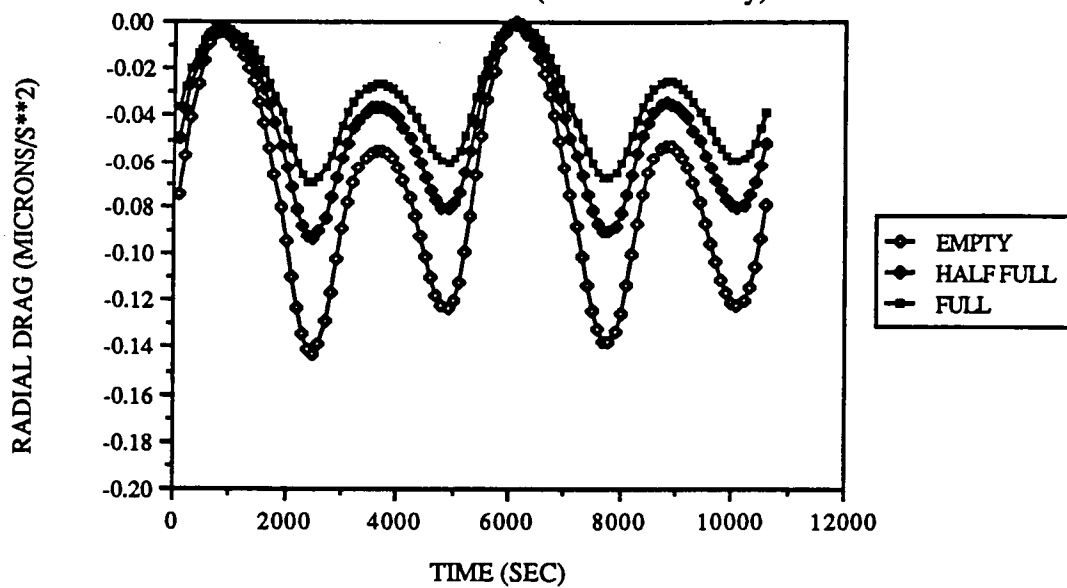


Figure 4.12 Predicted drag profiles along 2 GRM (160km) orbits on the vernal equinox of 1991 (high solar activity).

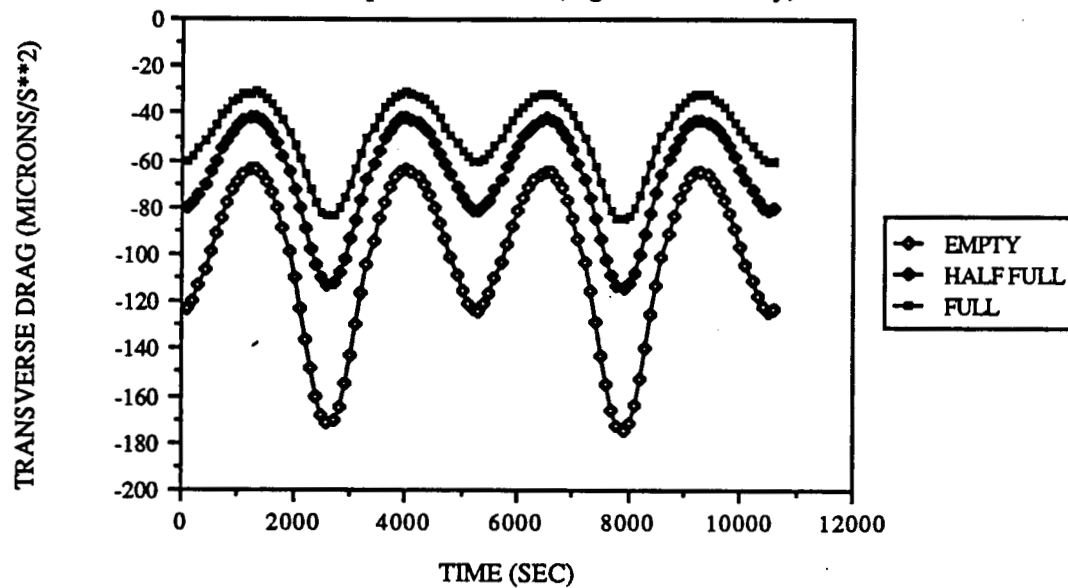


Figure 4.13 Predicted drag profiles along 2 GRM (160km) orbits on the summer solstice of 1996 (low solar activity).

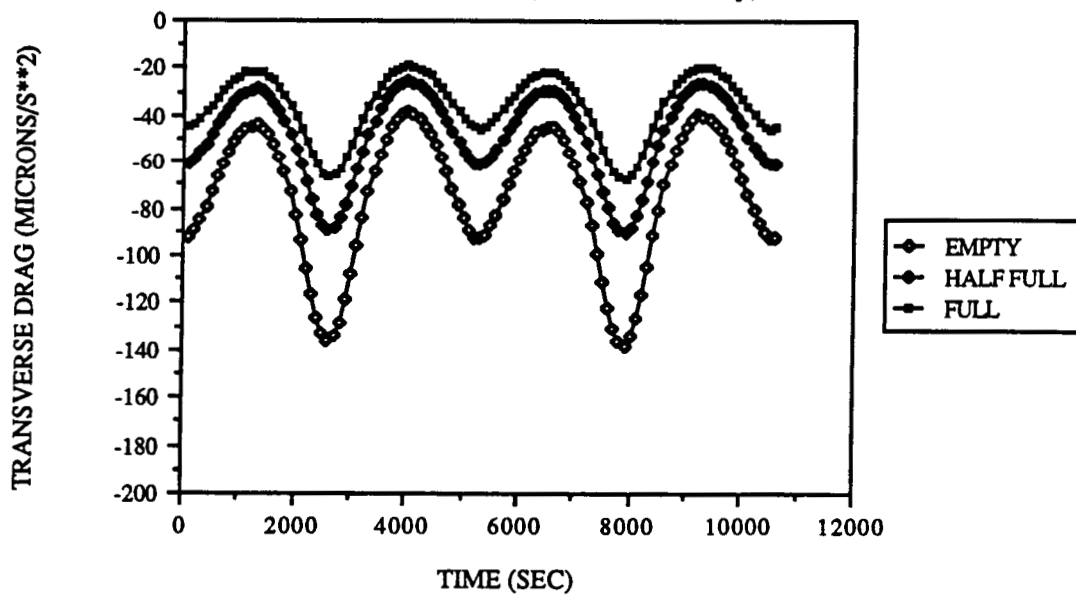


Figure 4.14 Predicted drag profiles along 2 GRM (160km) orbits on the vernal equinox of 1991 (high solar activity).

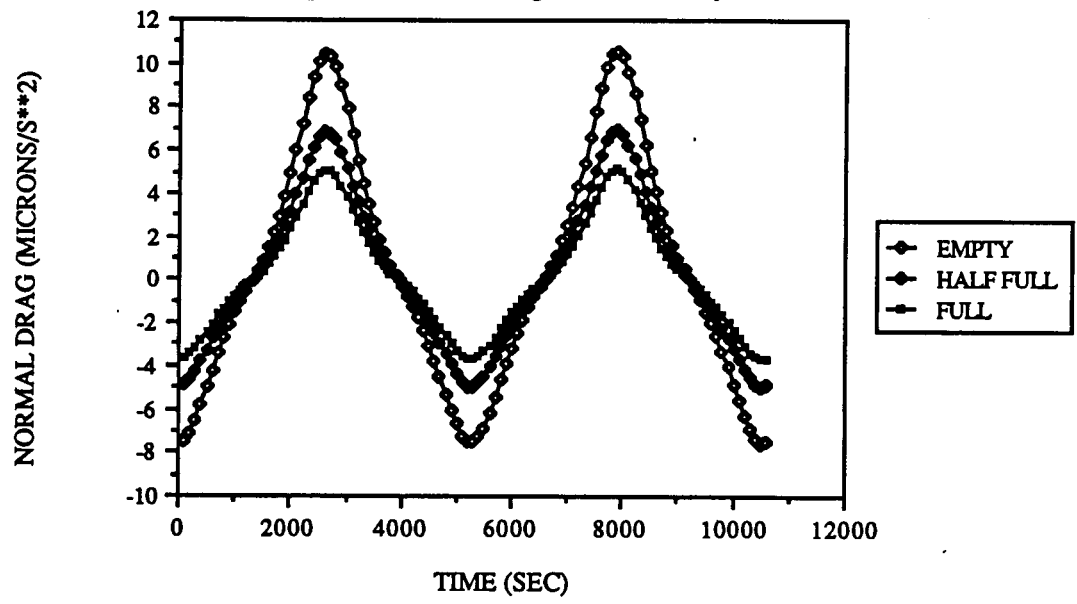
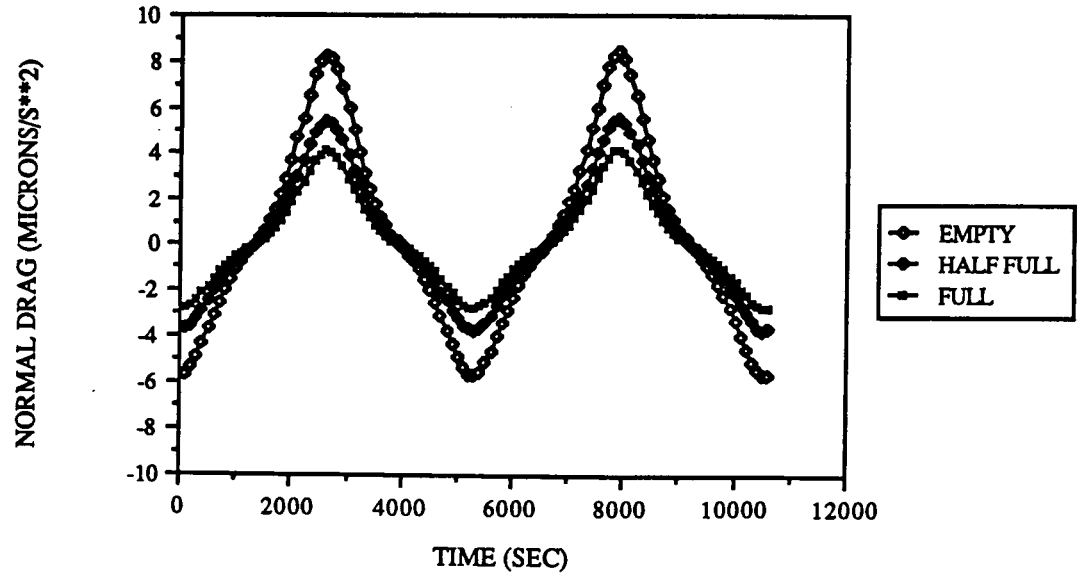


Figure 4.15 Predicted drag profiles along 2 GRM (160km) orbits on the summer solstice of 1996 (low solar activity).



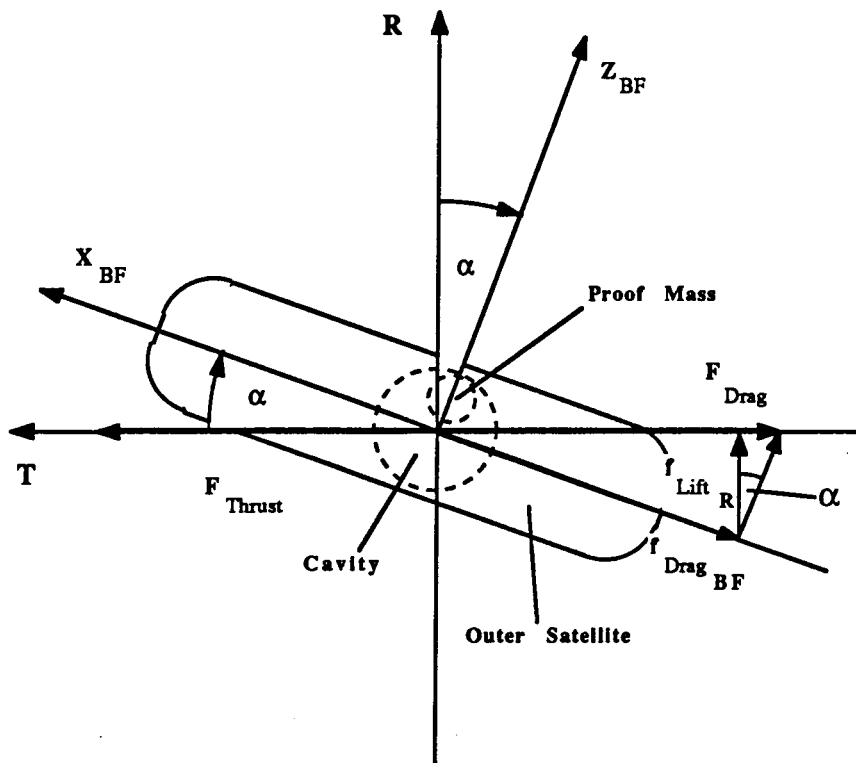


Figure 4.16 Aerodynamic lift force generated by the Ball Centering Control Law.

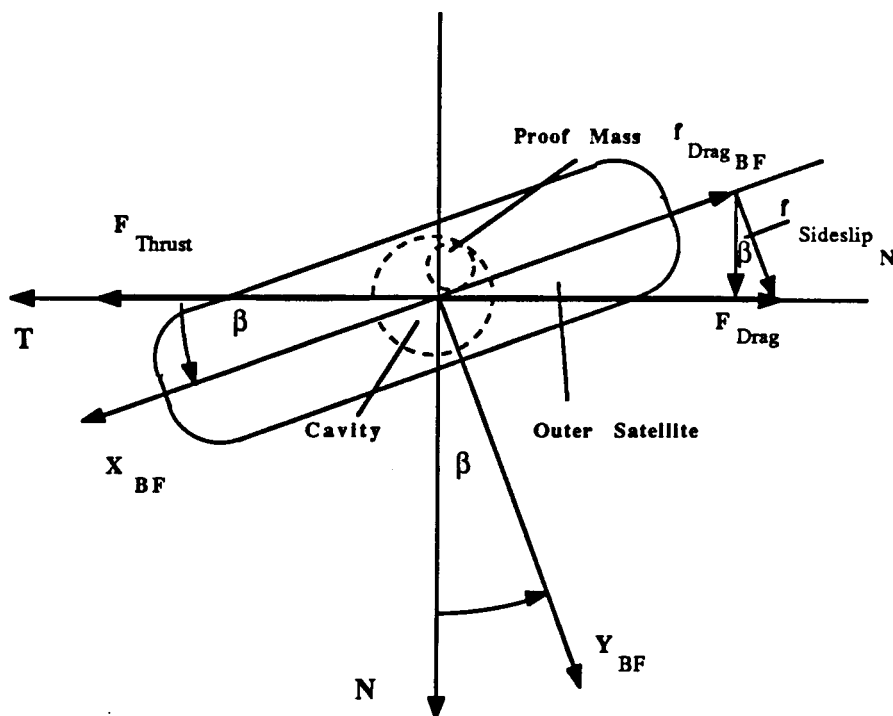


Figure 4.17 Aerodynamic sideslip force generated by the Ball Centering Control Law.

ORIGINAL PAGE IS
OF POOR QUALITY

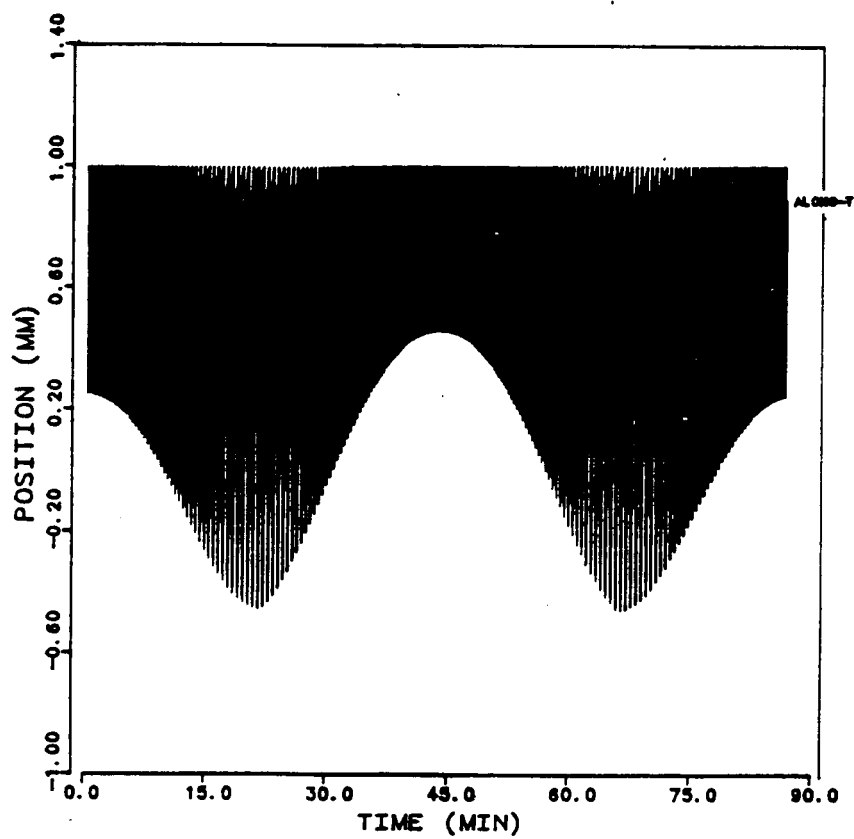


Figure 4.18-a Along-track position of proof mass with respect to spacecraft's centroid against time for one orbit during high solar activity with 95% fuel onboard.

THIS PAGE IS
OF POOR QUALITY

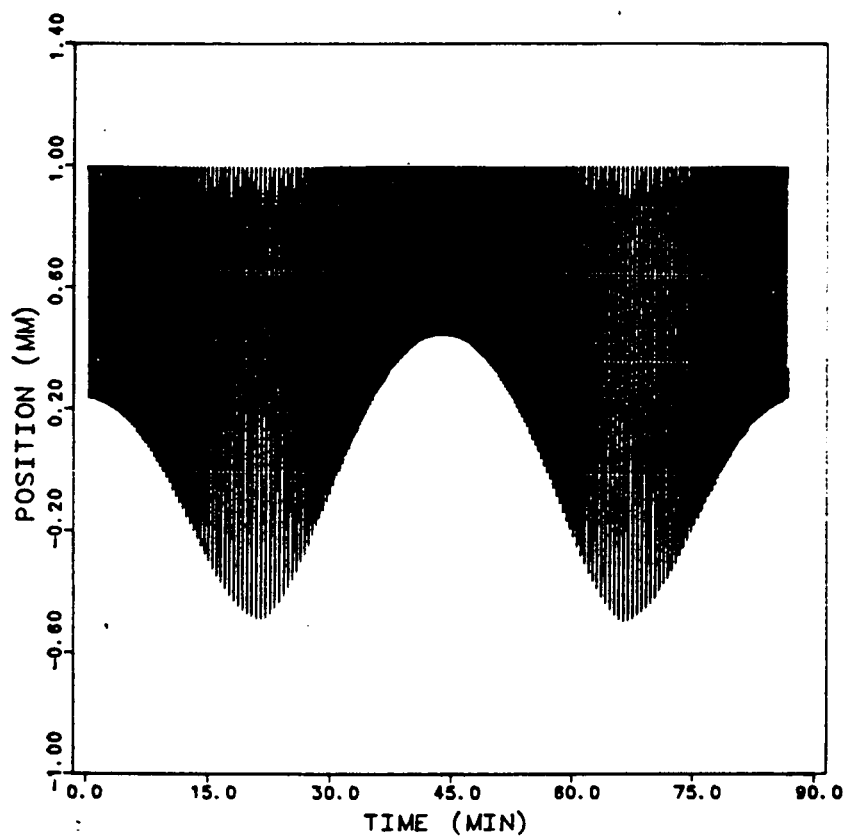


Figure 4.18-b Along-track position of proof mass with respect to spacecraft's centroid against time for one orbit during high solar activity with 50% fuel onboard.

ORIGINAL PAGE IS
OF POOR QUALITY

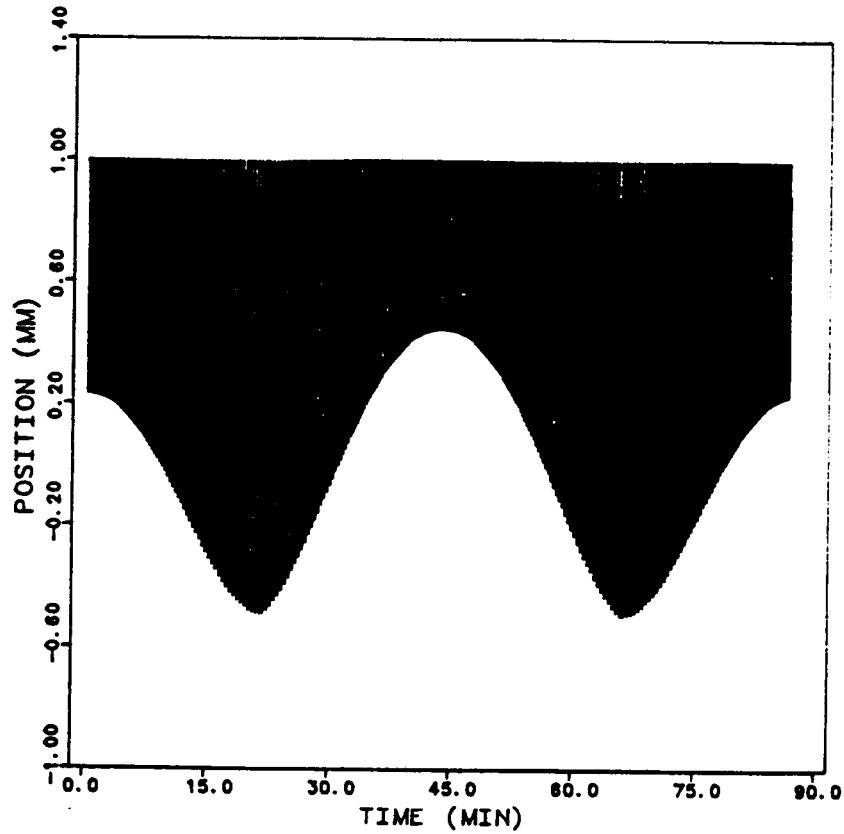


Figure 4.18-c Along-track position of proof mass with respect to spacecraft's centroid against time for one orbit during high solar activity with 5% fuel onboard.

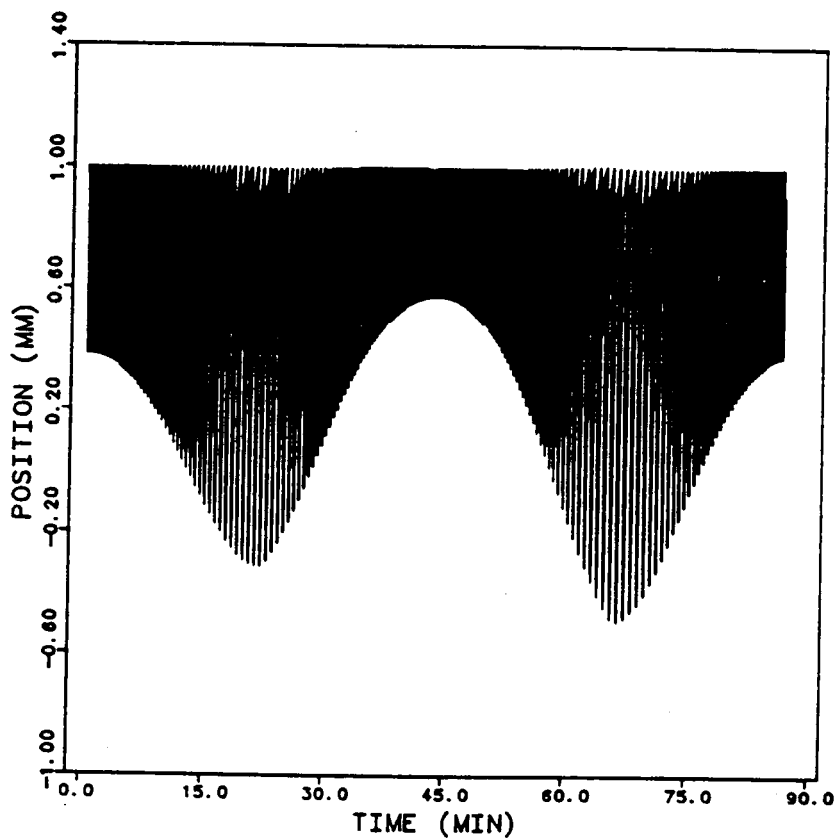
CERTAIN RANGE OF
OF POOR QUALITY

Figure 4.19-a Along-track position of proof mass with respect to spacecraft's centroid against time for one orbit during low solar activity with 95% fuel onboard.

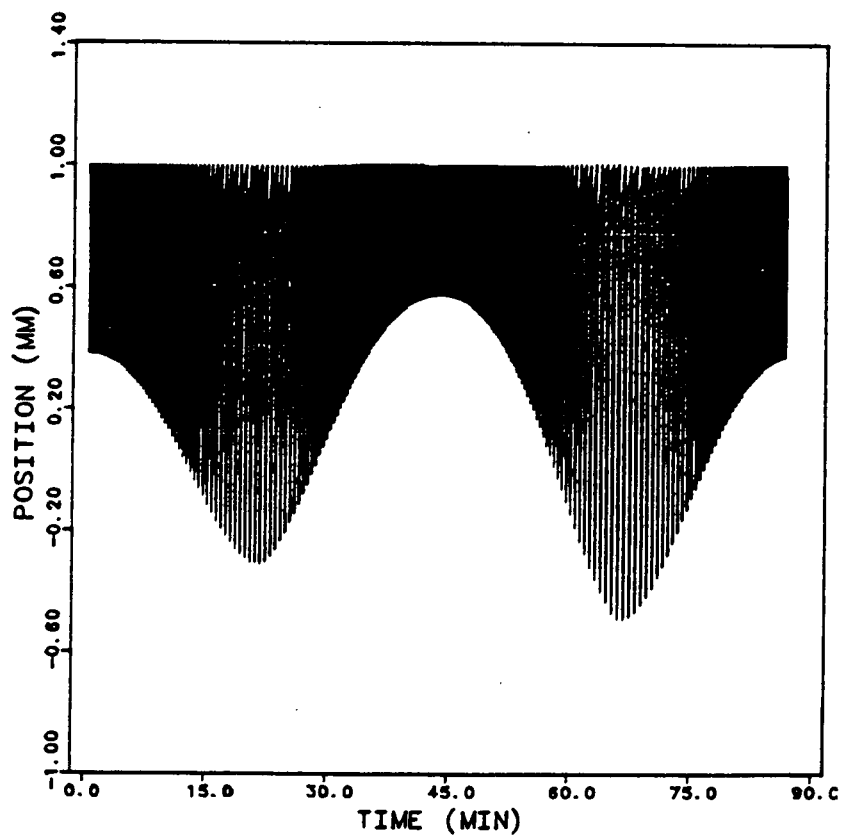
ORIGINAL POSITION OF
ON BOARD QUALITY

Figure 4.19-b Along-track position of proof mass with respect to spacecraft's centroid against time for one orbit during low solar activity with 50% fuel onboard.

ORIGINAL PAGE IS
OF POOR QUALITY

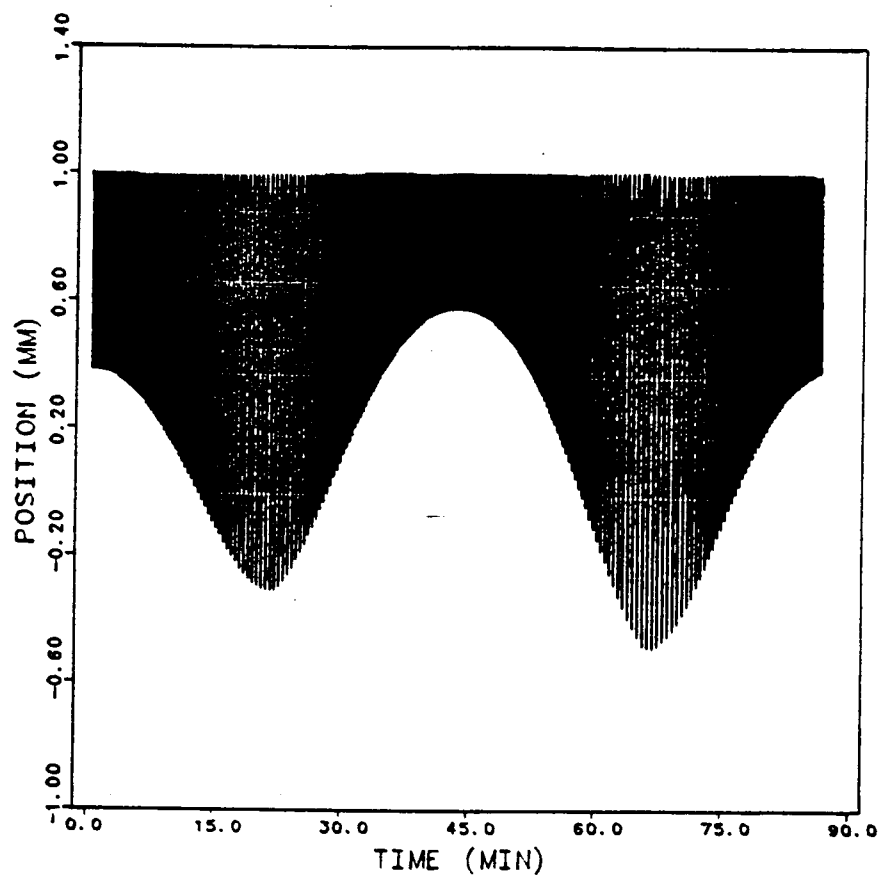


Figure 4.19-c Along-track position of proof mass with respect to spacecraft's centroid against time for one orbit during low solar activity with 5% fuel onboard.

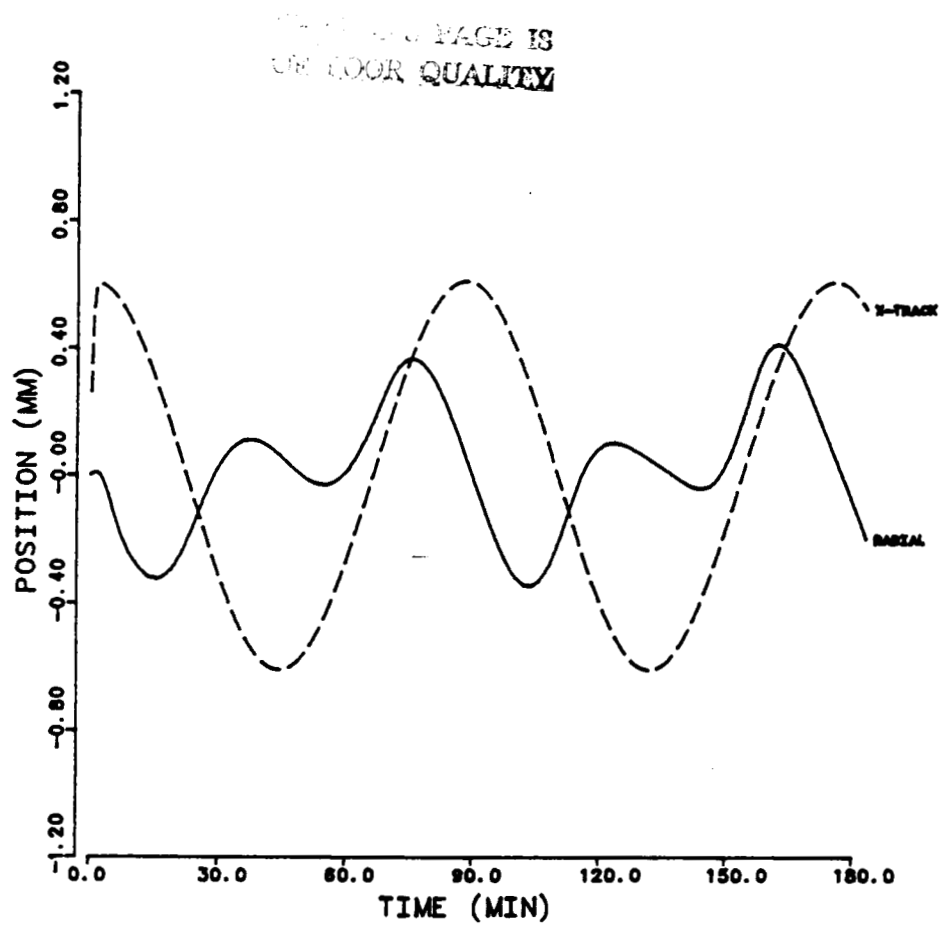


Figure 4.20-a Radial and cross-track position of proof mass with respect to spacecraft's centroid against time for two orbits during high solar activity with 95% fuel onboard.

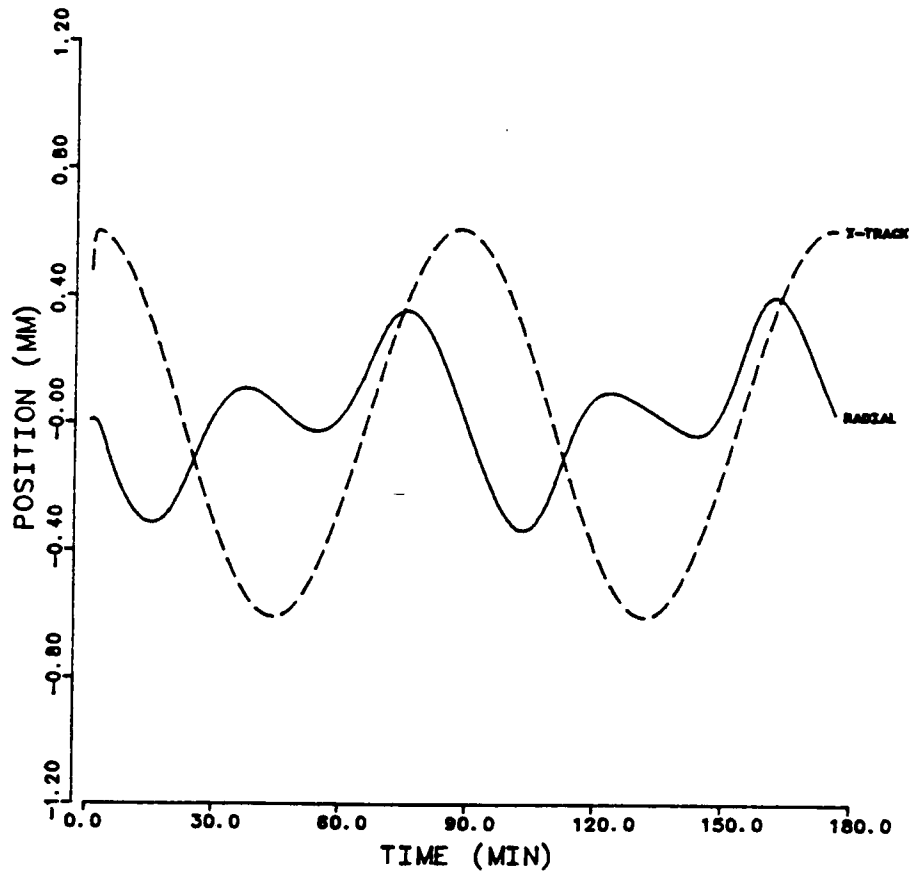


Figure 4.20-b Radial and cross-track position of proof mass with respect to spacecraft's centroid against time for two orbits during high solar activity with 50% fuel onboard.



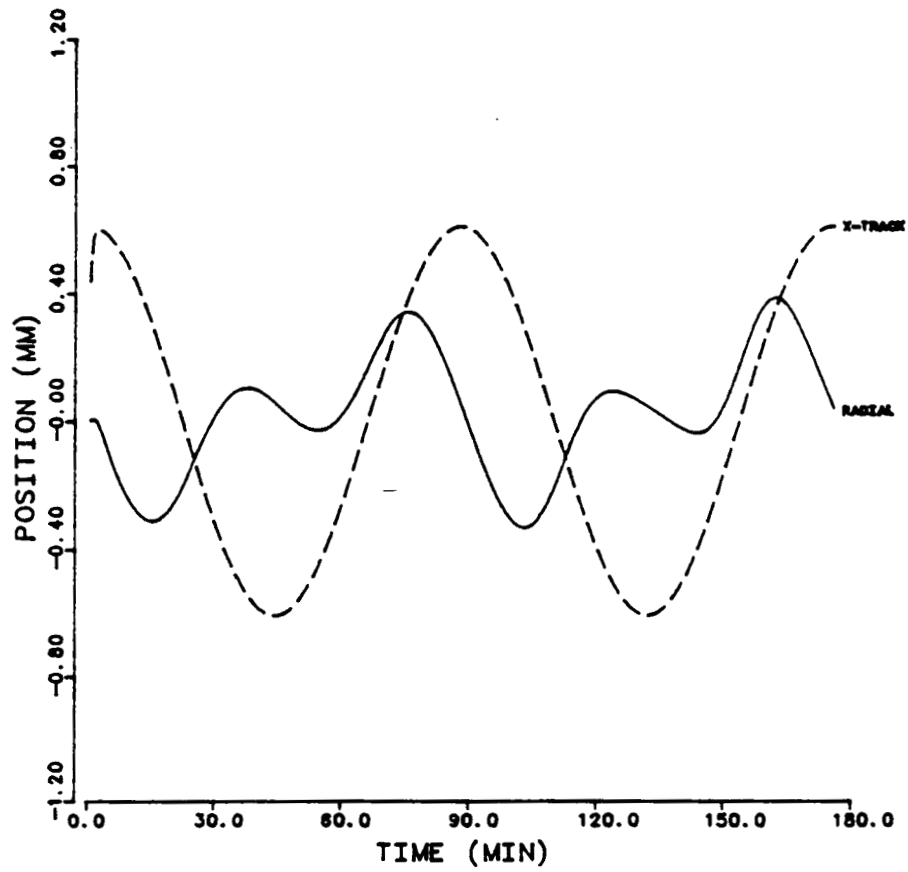


Figure 4.20-c Radial and cross-track position of proof mass with respect to spacecraft's centroid against time for two orbits during high solar activity with 5% fuel onboard.

C-2

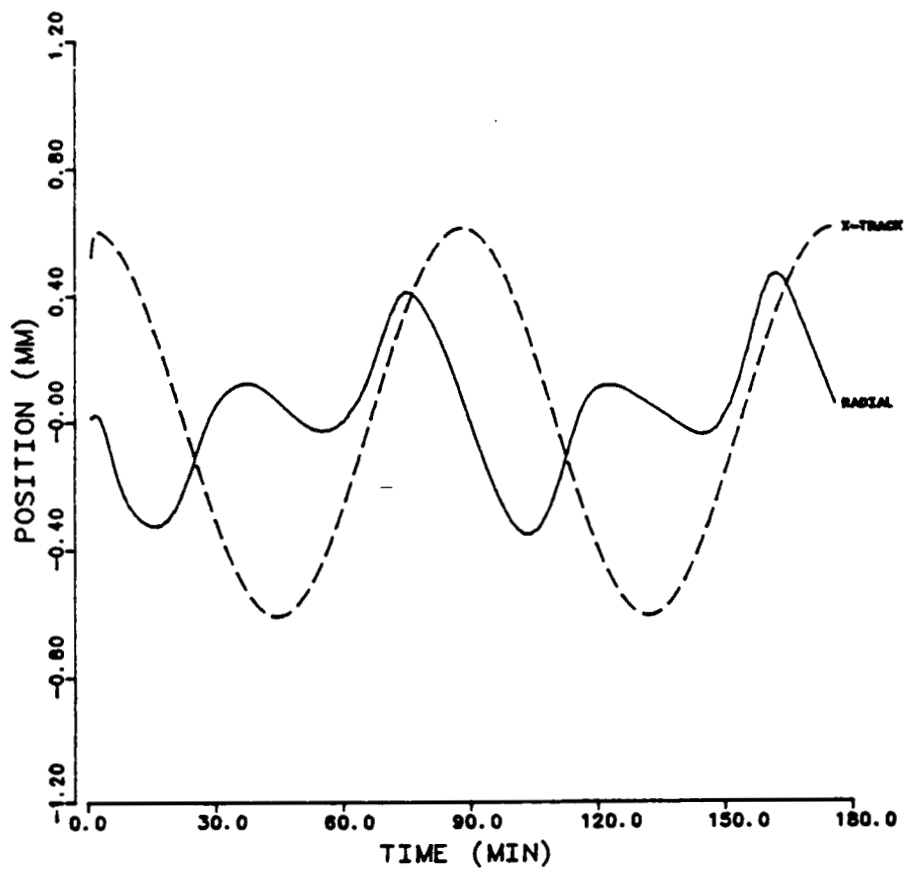


Figure 4.21-a Radial and cross-track position of proof mass with respect to spacecraft's centroid against time for two orbits during low solar activity with 95% fuel onboard.

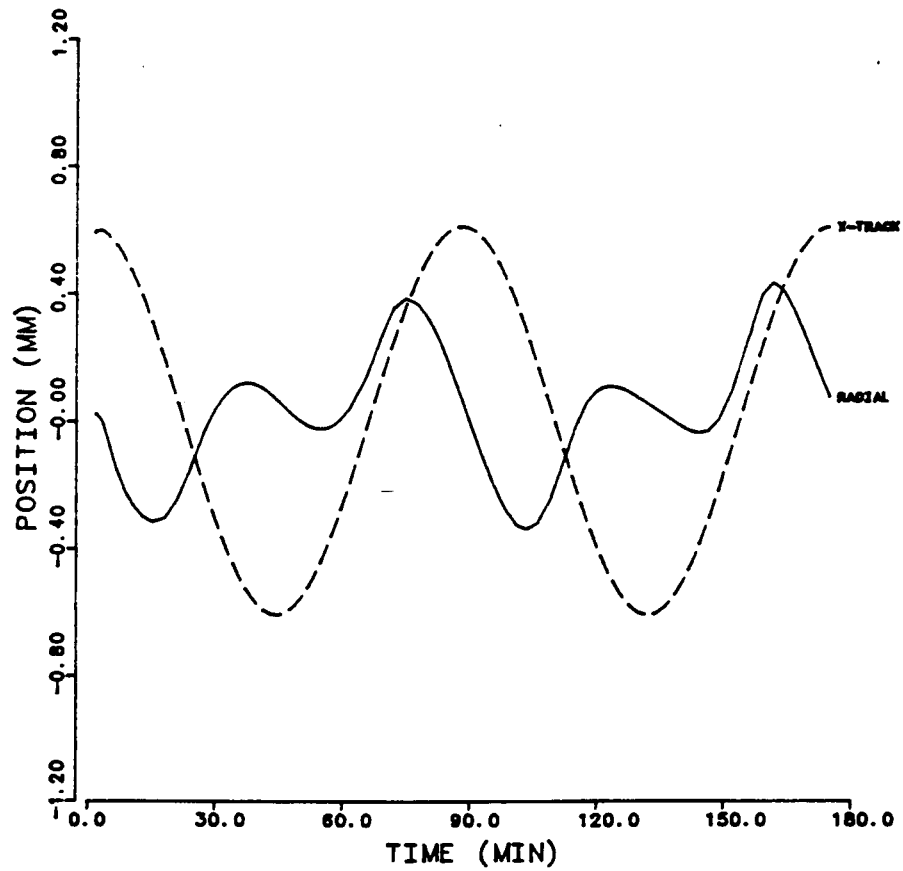


Figure 4.21-b Radial and cross-track position of proof mass with respect to spacecraft's centroid against time for two orbits during low solar activity with 50% fuel onboard.

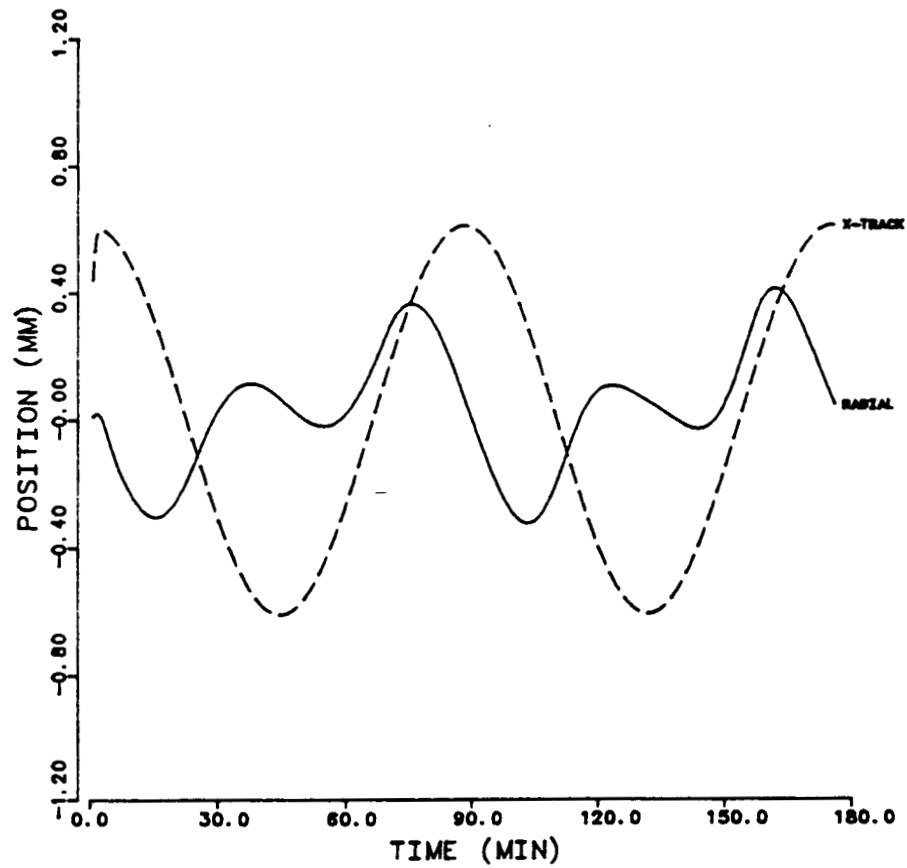


Figure 4.21-c Radial and cross-track position of proof mass with respect to spacecraft's centroid against time for two orbits during low solar activity with 5% fuel onboard.

ORIGINAL PAGE IS
OF POOR QUALITY

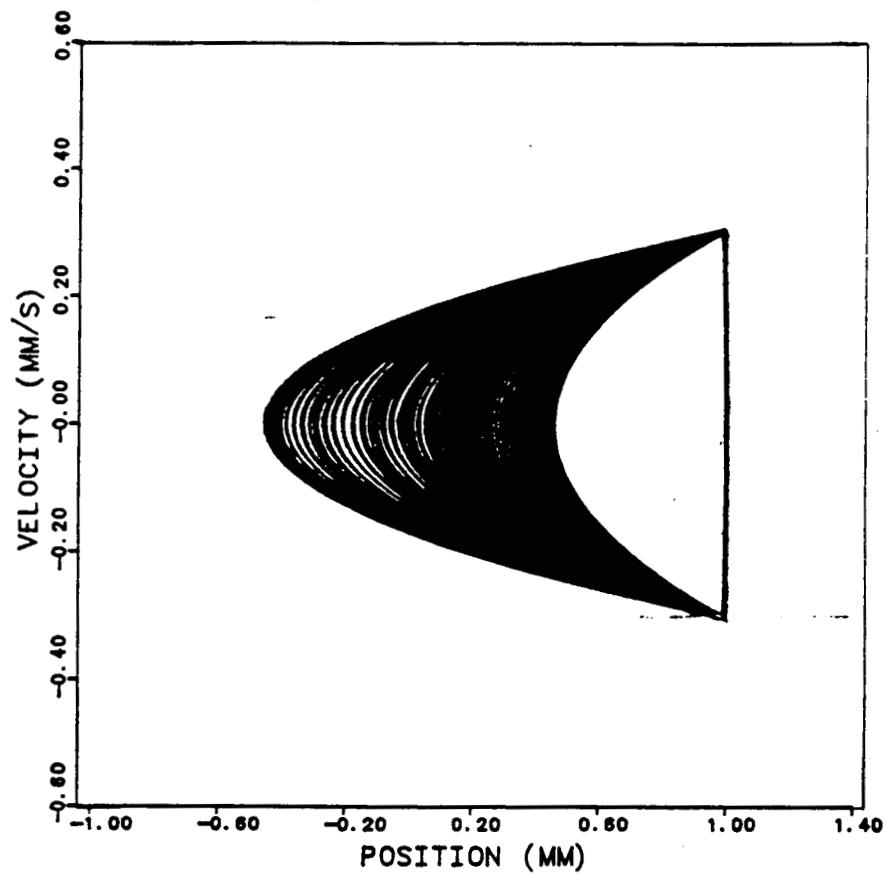


Figure 4.22-a Along-track phase plane limit cycle for one orbit during high solar activity with 95% fuel onboard.

ORIGINAL PAGE IS
OF POOR QUALITY

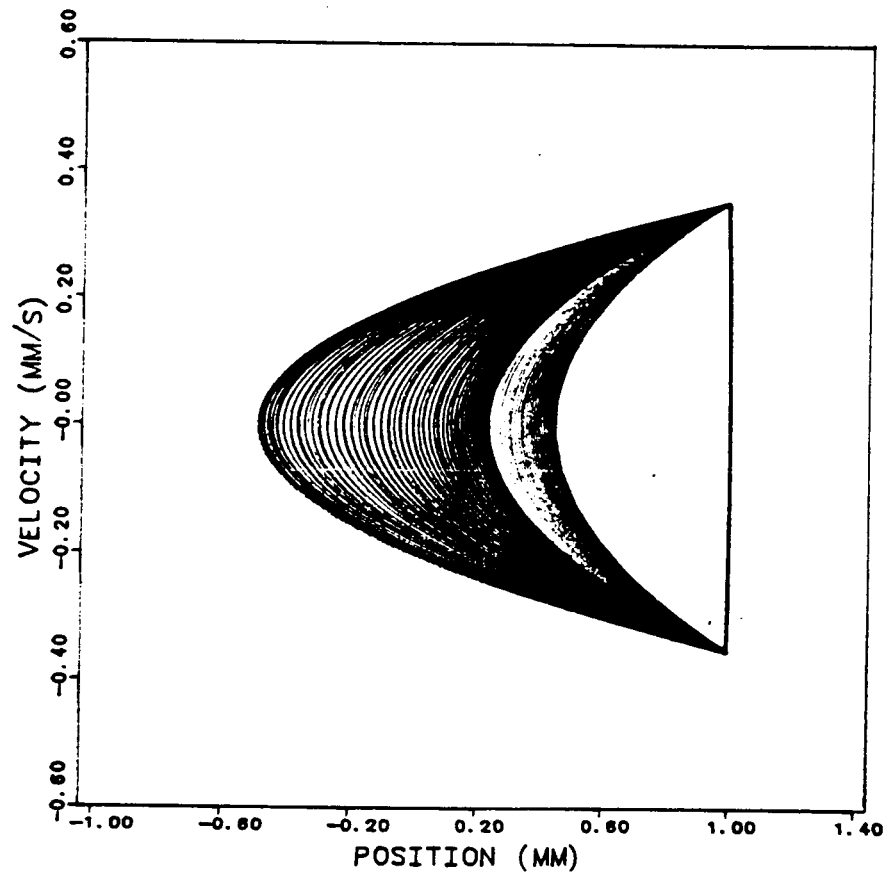


Figure 4.22-b Along-track phase plane limit cycle for one orbit during high solar activity with 50% fuel onboard.

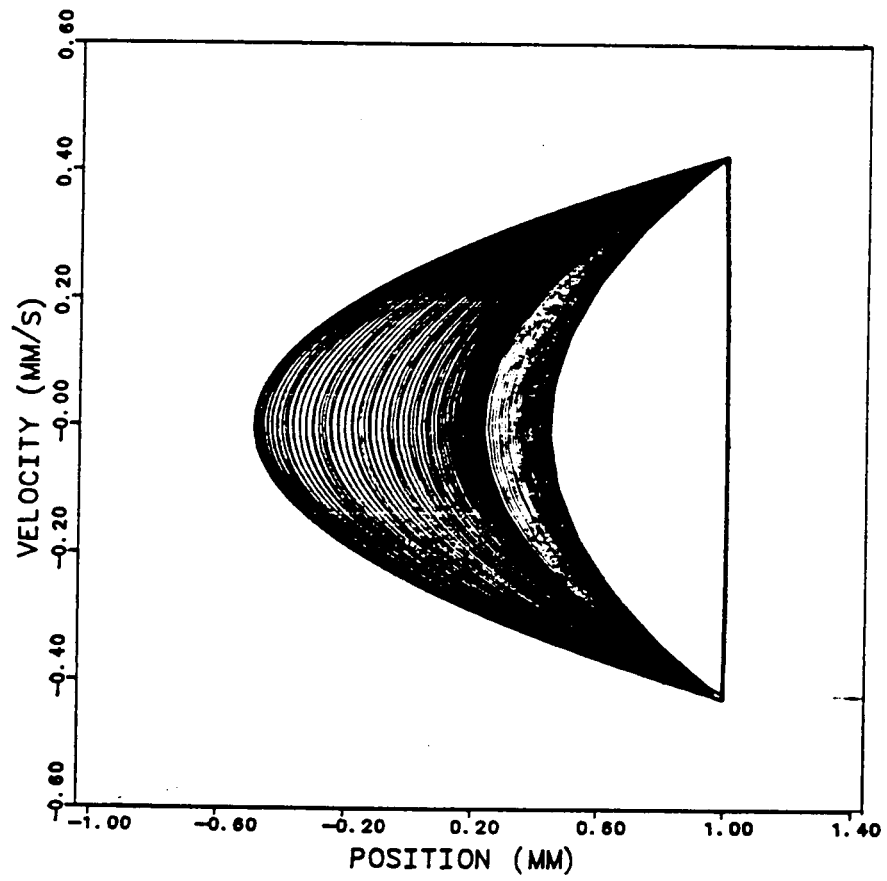


Figure 4.22-c Along-track phase plane limit cycle for one orbit during high solar activity with 5% fuel onboard.

ORIGINAL PAGE IS
OF POOR QUALITY

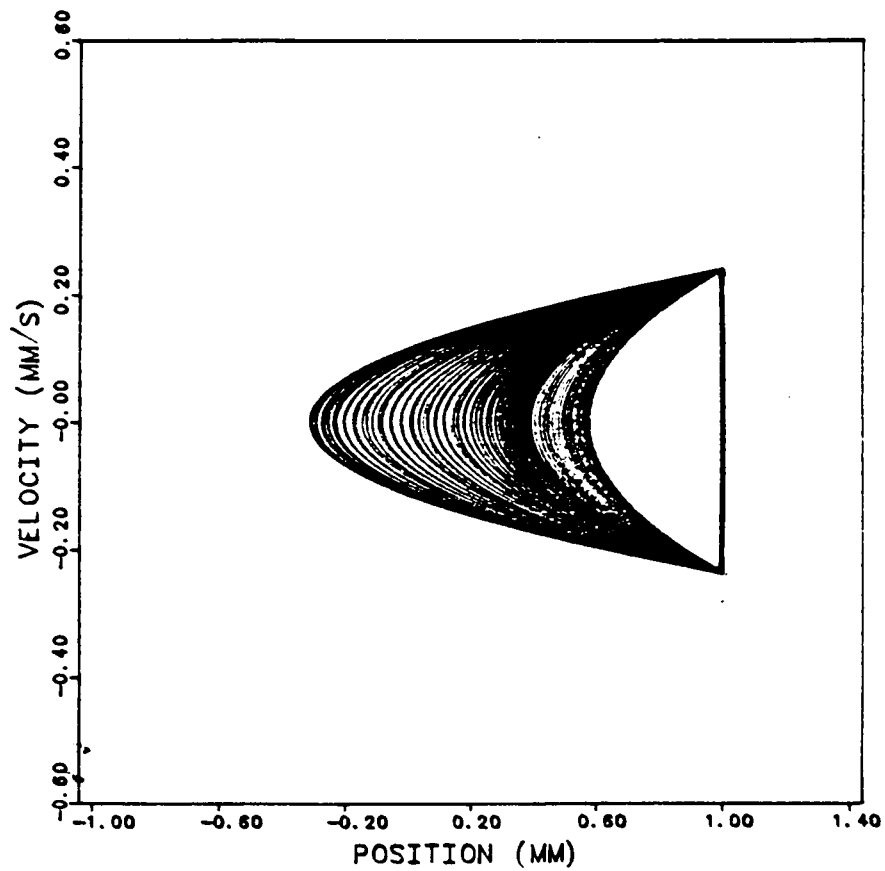


Figure 4.23-a Along-track phase plane limit cycle for one orbit during low solar activity with 95% fuel onboard.

ORIGINAL PAGE IS
OF POOR QUALITY

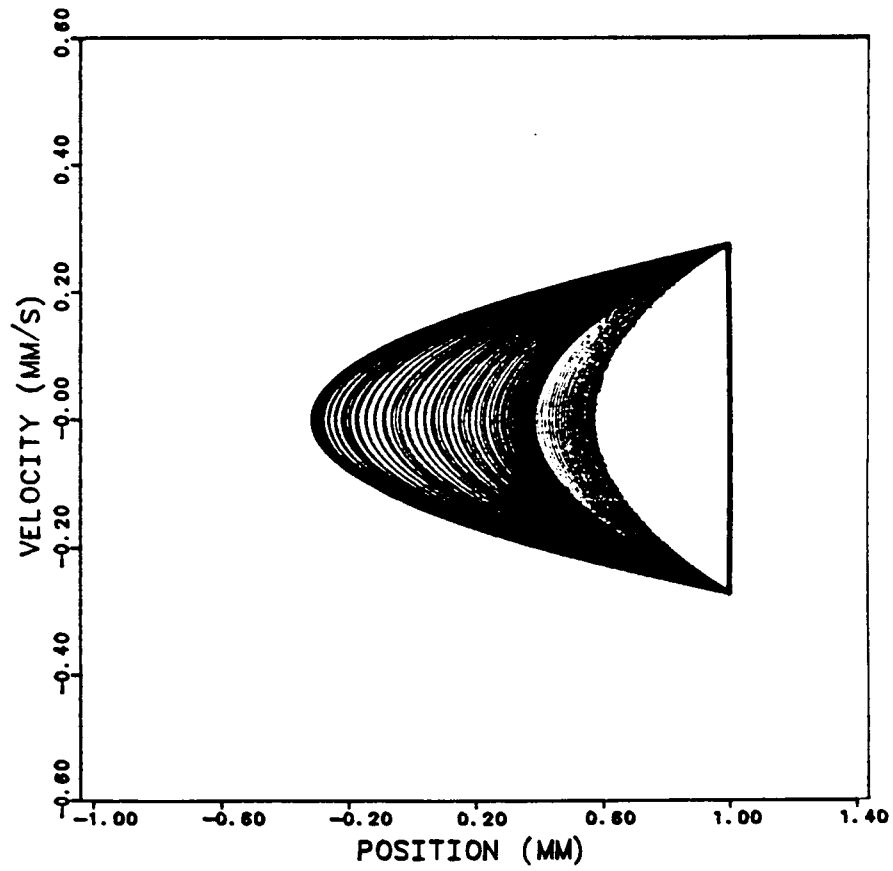


Figure 4.23-b Along-track phase plane limit cycle for one orbit during low solar activity with 50% fuel onboard.

ORIGINAL PAGE IS
OF POOR QUALITY

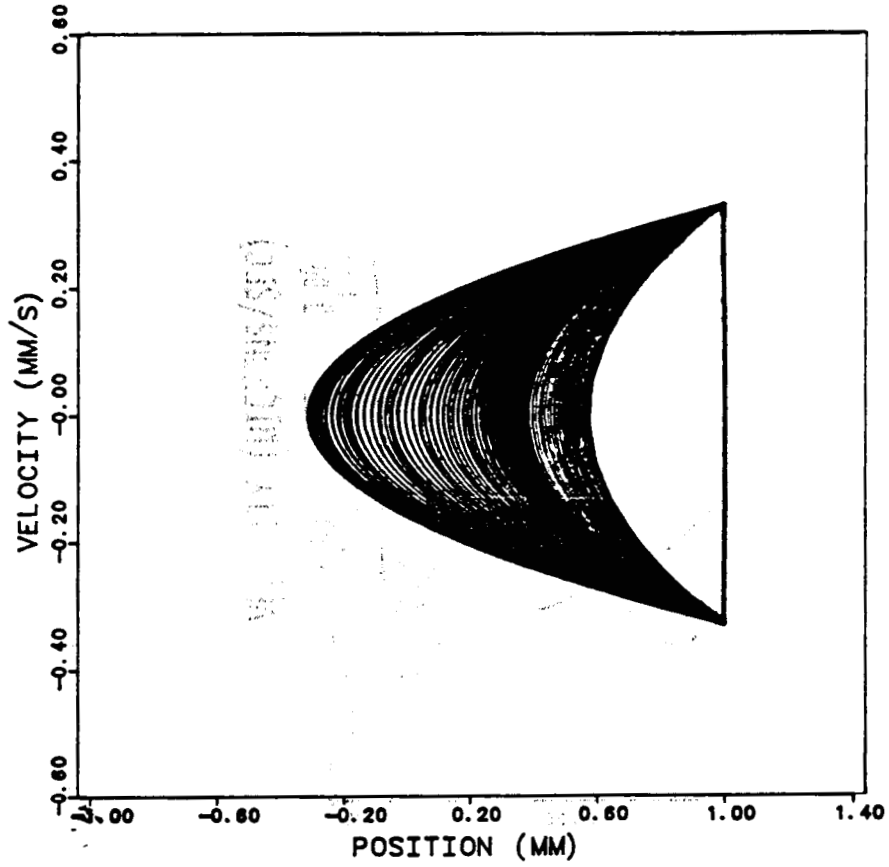


Figure 4.23-c Along-track phase plane limit cycle for one orbit during low solar activity with 5% fuel onboard.

ORIGINAL PAGE IS
OF POOR QUALITY

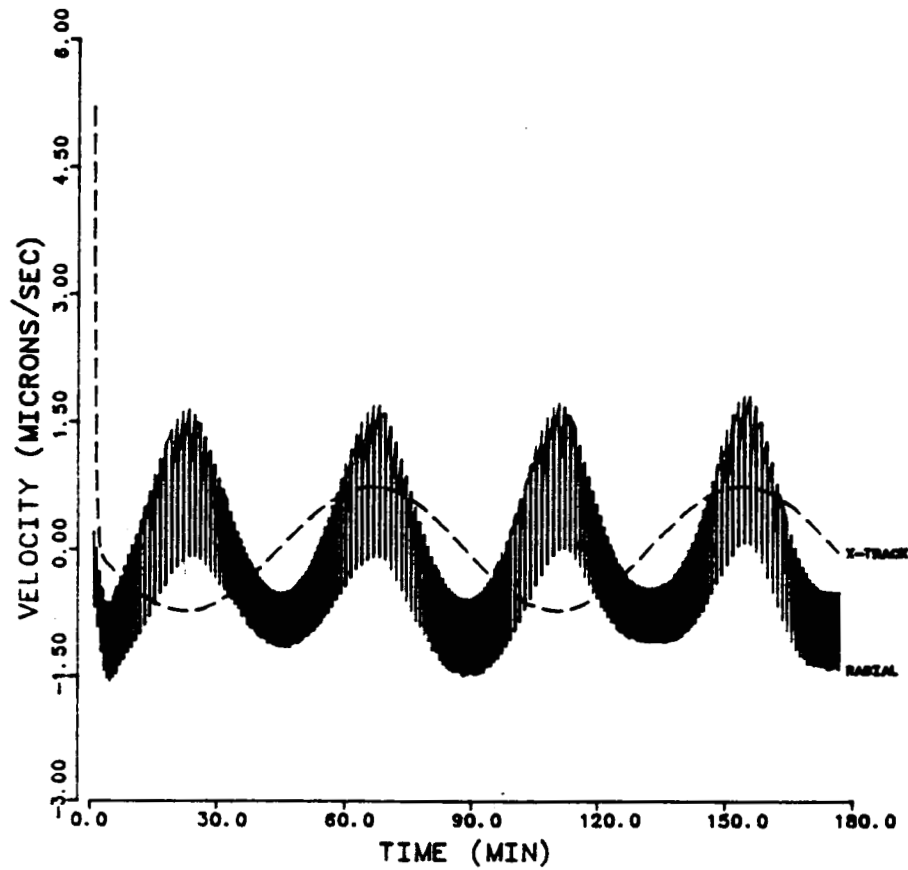


Figure 4.24 Radial and cross-track proof mass velocities with respect to the spacecraft against time for two orbits during high solar activity with 50% fuel onboard.

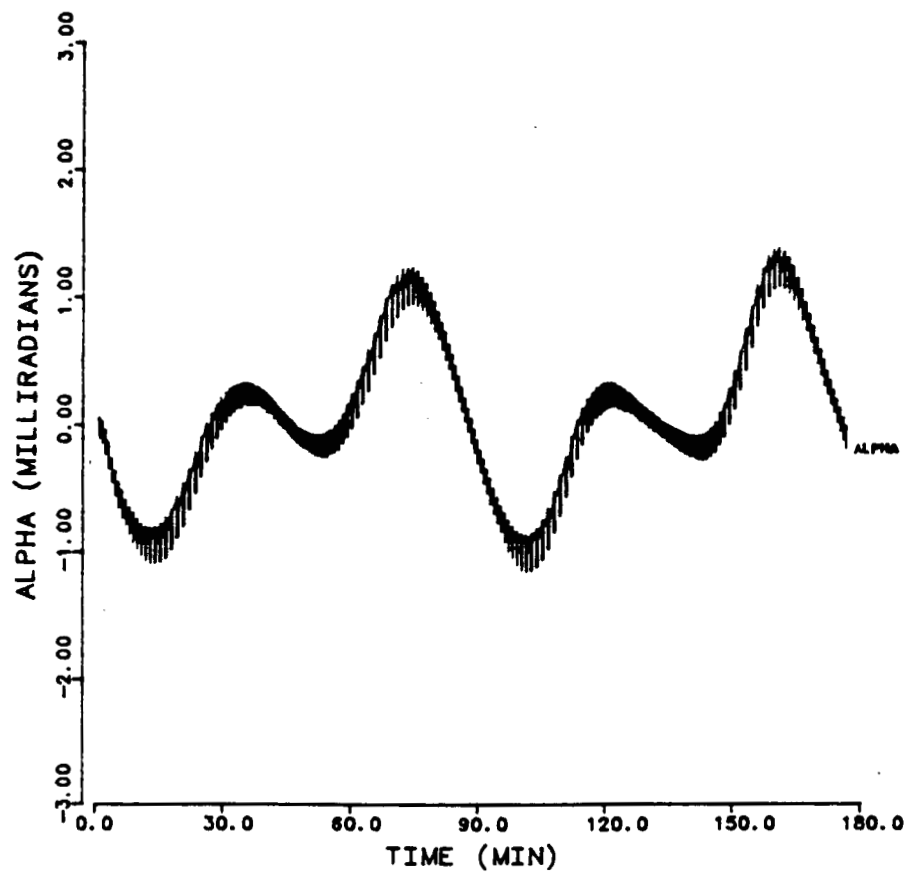


Figure 4.25 Ball-centering attitude control pitch angle against time for two orbits during high solar activity with 50% fuel onboard.

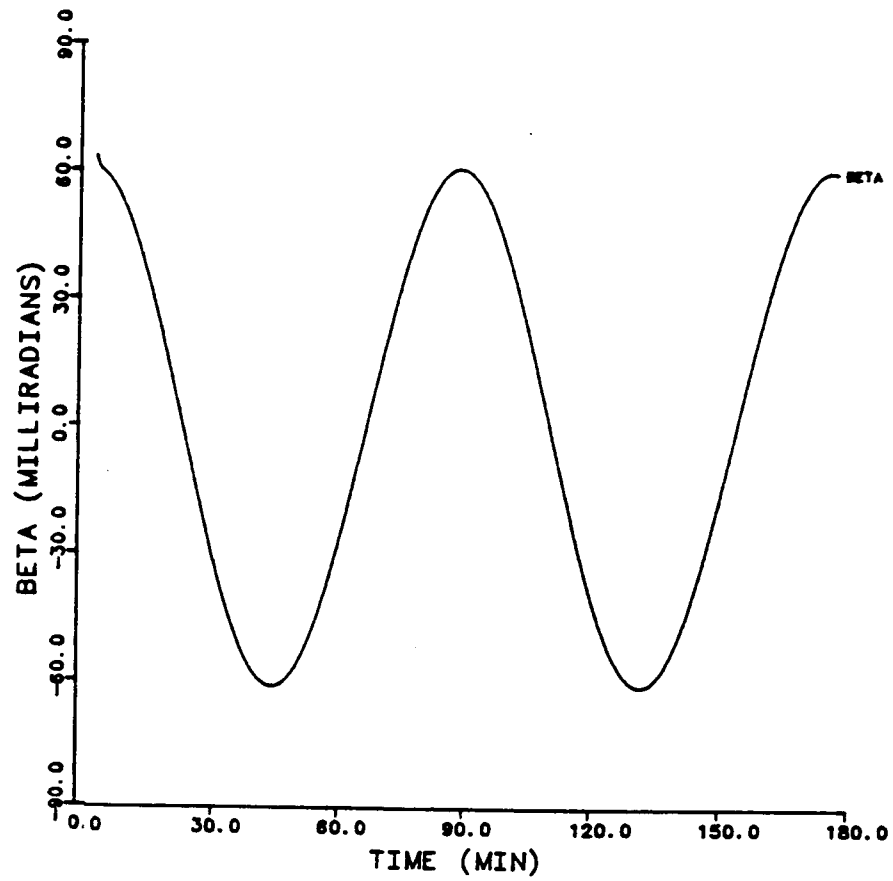


Figure 4.26 Ball-centering attitude control yaw angle against time for two orbits during high solar activity with 50% fuel onboard.

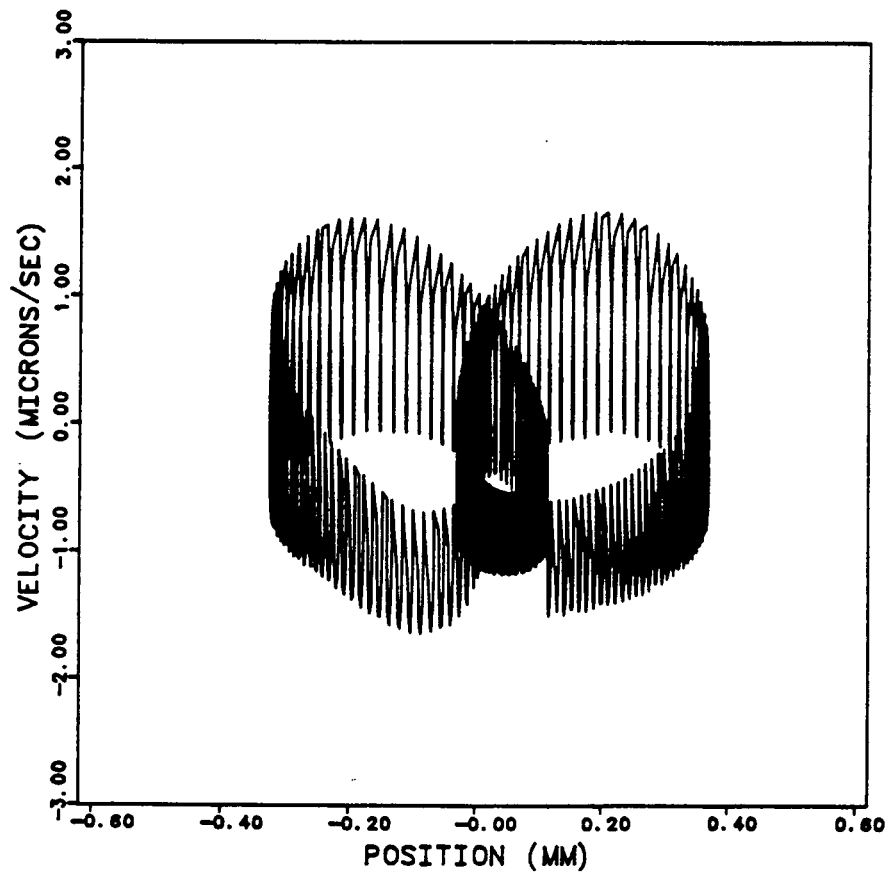


Figure 4.27 Radial phase plane diagram (velocity vs. position) for one orbit during high solar activity with 95% fuel onboard.

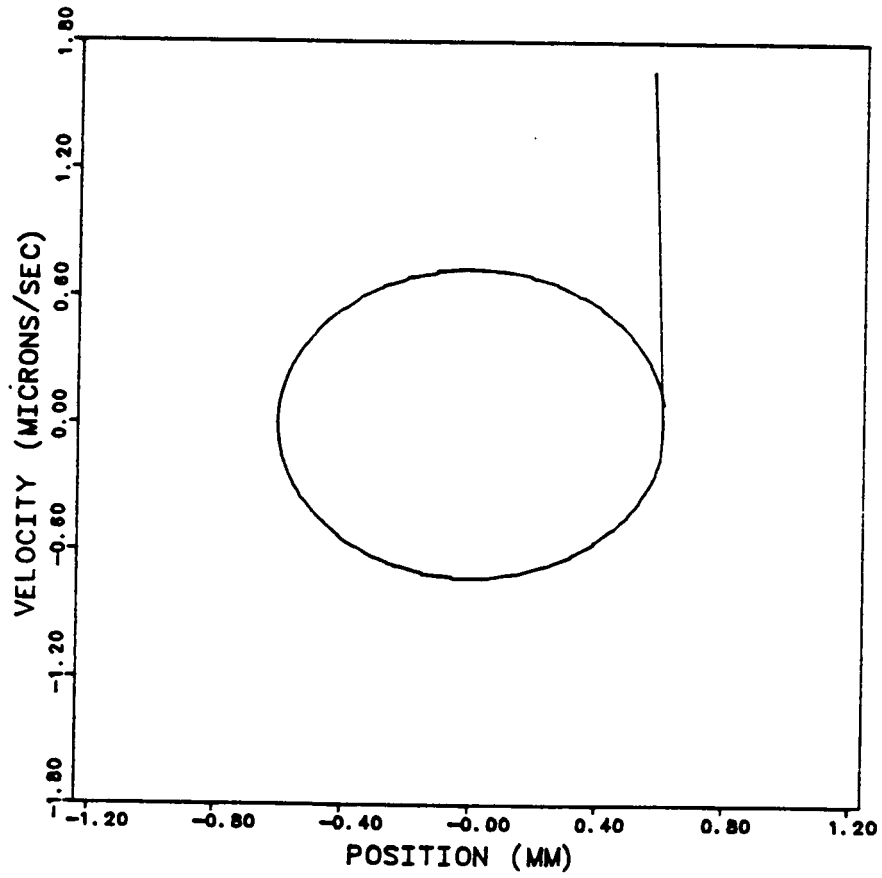


Figure 4.28 Cross-track phase plane diagram (velocity vs. position) for one orbit during high solar activity with 5% fuel onboard.

CHAPTER V

CONCLUSIONS

Presented in the first part of this study are two orbit simulations, one representing the actual GRM orbits and the other representing the orbit estimated from orbit determination techniques. These orbit simulations are essential for the geodetic science community to test gravity evaluation techniques before the GRM mission is launched. The second part of this study involved creating a computer algorithm to simulate GRM's drag compensation mechanism (DISCOS) so that fuel expenditure and proof mass trajectories relative to the spacecraft centroid could be calculated for the mission.

Although the low-low GRM spacecraft configuration was used exclusively, the orbit information obtained in this study is applicable to all possible scenarios since at least one low satellite will be used. In addition, the drag compensation study is also still applicable to a possible change of the design of DISCOS mechanism in the low-low scenario to a "two-stage" design, or the replacement of the SST (and elimination of the second satellite) with a gravity gradiometer.

The two-stage DISCOS and gravity gradiometer take the single stage DISCOS and SST a step further by eliminating the need for post flight proof mass velocity reconstruction since measurements taken by these instruments are always taken about the proof mass centroid. The two-stage DISCOS system incorporates an intermediate stage that is equipped with the SST antennae and is magnetically forced to follow the proof mass constantly while the outer stage uses the same concept as performed in this study to follow the intermediate stage by firing appropriate

thrusters to compensate for drag. The gravity gradiometer uses a set of high precision accelerometers whose measurements would replace the range rate measurements from the SST for the determination of the higher degree and order terms of the geopotential.

5.1 Summary

With a geopotential of degree and order 360, the 32 day true orbit simulation of the two GRM spacecrafts' proof masses required a total of 19.2 hours of CPU time on the Cray X-MP/24 supercomputer, nearly 100 times faster than on any conventional mainframes computers. The initial conditions determined by *White* [1987] satisfied the requirement that the orbit repeat after exactly 32 sidereal days

The orbit determination solution discussed here merely indicates some of the major points that must be considered when solving for the nominal trajectory. It was shown that the orbit can be determined within the 3σ accuracy requirement of 100 meters in the radial and 300 meters in the along- and cross-track directions for the gravity mission. The magnetic mission requirements of 60 meters radial and 100 meters in the along- and cross-track components could not be met with this solution; however the nominal orbit simulation will be used to further improve gravity models so that eventually the residuals will meet the magnetic mission requirements.

The one-way Doppler algorithm, created for the SST simulation, rarely did not converge for measurements received by satellite two's antenna, and the latest measurements calculated during these non-convergences did not meet the $1 \mu\text{m/s}$ requirement. Much effort went into finding the cause of this iteration problem, but the problem was never solved completely. It was finally thought to be due to

round-off errors occurring during the interpolation of the ephemeris between the recorded time points.

The results of the GRM DISCOS simulation demonstrated that the spacecraft can essentially be "drag-free", that is, the spacecraft can be made to follow the purely gravitational trajectory of the proof mass. The results showed that the centroid of the spacecraft can be controlled so that it will not deviate more than 1.0 mm in any direction from the centroid of the proof mass.

Radial and cross-track proof mass excursions were shown to be constrained within the ± 1.0 mm region without firing radial or cross-track thrusters, but with the use of the ball-centering attitude control law which pitches or yaws the spacecraft at slight angles to produce counteracting lift or sideslip forces.

The aft along-track thrusters were determined to fire for 55 to 105 milliseconds every 5 to 25 seconds depending on drag magnitudes and the current satellite mass. The total number of aft thruster firings ranged from 1.2 to 1.7 million. Total thrust-on times, and thus fuel expenditure rates, were essentially independent of the variation in mass due to fuel consumption for either the high solar or low solar activity case. It was also shown that estimated fuel expenditures of 763 to 1056 kg of hydrazine for drag compensation compared closely to other studies.

5.2 Future Study

Now that both a representation of the proof mass orbit trajectories and a way of simulating the drag compensation mechanism exists, the simulation of the outer satellites' orbits can be determined. Proof mass displacements from the satellites'

mass centers corrupt the SST range-rate measurements, thus the outer satellite orbit simulation will incorporate this source of error thereby allowing precise calculations of the SST range-rate measurements.

Many refinements and improvements are needed to improve the drag-free thruster control algorithm. To fully simulate the DISCOS mechanism, adaptive control laws should be implemented to provide coasting arcs of nearly constant duration. An algorithm to adjust the thruster turn-off switches (imparted relative velocities) according to the magnitude of drag and satellite mass is needed since either too small or too large limit cycles would result if this parameter is held constant throughout the mission. This would require aft thrusters to fire frequently or fore thrusters to fire occasionally, thus increasing fuel consumption. It was not clear from previous reports that this point has been studied.

The Jacchia 1971 atmospheric model used in this simulation was also slightly outdated. A more current one, such as the Jacchia 1977 atmospheric model should be incorporated into the study. In addition, the drag model used in this study did not take into account the effects due to complicated atmospheric gas impingements and reflections. Also, a detailed model of the satellite's surface area incident to the airstream is needed since the incidental area (frontal area) used in this study was held constant and radial and cross-track drag components were determined from this value.

Finally, the inclusion of a fuel expenditure algorithm into the DISCOS simulation is needed to better calculate fuel expenditures. Longer simulations (greater than one orbit) would further improve these calculations.

BIBLIOGRAPHY

- Bate, R. R., D. D. Mueller, J. E. White, Fundamentals of Astrodyanmics, Dover Publishings, Inc., New York, 1971.
- Bettis, D. G., Private Communication in Department of Aerospace and Engineering Mechanics, University of Texas, Austin, 1977.
- Fischell, R. E. and V. L. Piscane, "A Drag-Free Lo-Lo Satellite System for Improved Gravity Field Measurements," Proceedings of the 9th GEOP Conference, An International Symposium on the Application of Geodesy to Geodynamics, Dept. of Geodetic Science, No. 280, Ohio State University, October 2-5, 1978.
- Hunt, J. W., "Geopotential Research Mission Spacecraft Simulation and Analysis: Guidance and Control System Simulation," JHU/APL SDO-7397, September 1984.
- Hunt, J. W. jr., F. F. Mobley, A. C. Sadilek, "A Study of the Feasibility of the Two-Stage DISCOS for GRM," JHU / APL SDO-8411, April 1987.
- Holmes, N. C., CH. Reigber, "Study of a Satellite-to-Satellite Tracking Gravity Mission," DGFI, Munich, March 1987.
- Jacchia, L. G., Smithsonian Astrophysical Observatory, Special Report 332, May 1971.
- Johns Hopkins University Applied Physics Laboratory and the Guidance and Control Laboratory of Standford University, "A Satellite Freed of All but Gravitational Forces: 'TRIAD I'," Journal of Spacecraft and Rockets, Vol. 11, September 1974, pp. 637-644.
- Keating, T., P. Taylor, W. Kahn, F. Lerch, "Geopotential Research Mission Science, Engineering, and Program Summary," NASA Technical 86240, May 1986.

- Lange, B., "The Drag-Free Satellite," AIAA Journal, Vol. 2, No. 9, September 1962, pp. 1590-1606.
- Lerch, F. A., B. H. Putney, C. A. Wagner, S. M. Klosko, "Goddard Earth Models for Oceanographic Applications (GEM 10B and 10C)," Marine Geodesy, Vol. 5, No. 2, 1981.
- Lundberg, J. B., "Computational Errors and Their Control in the Determination of Satellite Orbits," Doctorial Dissertation, The University of Texas at Austin, December 1984.
- McNamee, J. B. Jr., "Perturbation of Low Altitude Satellite Motion Due to the Prescence of Ocean Eddies," Master's Thesis, The University of Texas at Austin, December, 1986.
- Pines, S., "Uniform Representation of the Gravitational Potential and its Derivatives," AIAA Journal Vol. 11, No. 11, November 1973, pp. 1508-1511.
- Rapp, R. H. and J. Y. Cruz, "Spherical Harmonic Expansions of the Earth's Gravitational Potential to Degree 360 using 30' Mean Anomalies," Report No. 376, Dept. of Geodetic Science and Surveying, The Ohio State University, Columbus, Dec. 1986.
- Rapp, R. H., "The Earth's Gravity Field to Degree and Order 180 Using SEASAT Altimeter Data, and Other Data," Report No. 322, Dept. of Geodetic Science and Surveying, The Ohio State University, Columbus, Dec. 1981.
- Ray, J. C. and R. E. Jenkins, "GRAVSAT / MAGSAT - A Guidance and Control System Annual Report 1981, Volume 1," JHU / APL SDO-6179, September 1981.
- Ray, J. C. and R. E. Jenkins, "GRAVSAT / MAGSAT - A Guidance and Control System Annual Report 1981, Volume 2," JHU / APL SDO-6179, September

1981.

Ray, J.C. and R. E. Jenkins, R. A. Van Patten, J. C. Junkins, "Attitude and Translational Control of a Low-Altitude GRAVSAT," AIAA / AAS Astrodynamics Conference," AIAA-82-1416, August 1982.

Roberts, C. E., jr., "An Analytical Model for Upper Atmosphere Densities Based upon Jacchia's 1970 Model," *Celestial Mechanics*, Vol. 4, 1971, pp. 368-377.

Schutz, B. E., B. D. Tapley, J. B. Lundberg, and P. Halamek, "Simulation of a Geopotential Research Mission For Gravity Studies," Center for Space Research, University of Texas at Austin.

White, L. K., "Simulation and Analysis of a Geopotential Research Mission," Doctorial Dissertation, The University of Texas at Austin, December 1987.